

A thesis entitled

*Electromagnetically Induced Transparency
with Squeezed Vacuum*

written by

Daisuke AKAMATSU

submitted to

*The Department of Physics
Tokyo Institute of Technology*

in partial fulfillment of the requirements for
the degree of Doctor of Philosophy,
2007.

This thesis is supervised by:

Prof. Mikiyo KOZUMA

The thesis jury is composed of:

Prof. Fujio MINAMI

Prof. Masahito UEDA

Prof. Hideto KANAMORI

Prof. Michio MATSUSHITA

Acknowledgement

It gives me great pleasure to express my deepest respect and sincere gratitude to Prof. Mikio Kozuma for his excellent guidance throughout the duration of this thesis work. His deep insight for getting to the heart of the problem and exceptional capacity to work has been a source of inspiration for me.

I am grateful to Prof. Akira Furusawa, Dr. Nobuyuki Takei, Mr. Hidehiro Yonezawa and Mr. Kentaro Wakui for their valuable comments and stimulating discussions on generation of a squeezed vacuum with sub-threshold optical parametric oscillator.

I am grateful to Prof. Takuya Hirano for his fruitful lecture on experimental quantum optics. The concept of a bichromatic homodyne method was born from his lecture.

I would like to thank Dr. Motonobu Kouroggi and Dr. Kazuhiro Imai for helpful comments on feed-forward phase lock method.

I wish to express my appreciation to Prof. Hiroki Saito for discussing the mathematical issues on the experiments.

I would like to thank to Prof. Fujio Minami, Prof. Masahito Ueda, Prof. Hideto Kanamori, and Prof. Michio Matsushita for their valuable comments on the thesis.

I also would like to thank one of my collaborators, Yoshihiko Yokoi, for making excellent electric circuits, which had an active part in our experimental setups.

I wish to express my gratitude to the members of Kozuma lab, Dr. Koji Usami, Keiichirou Akiba, Norifumi Kanai, Takahito Tanimura, Jun-ichi Takahashi, Ryotaro Inoue, Kousuke Kashiwagi, and Toshiya Yonehara for sharing a great deal of fun time with me.

Special thanks goes to one of my best friends, Brett, who corrected many grammatical mistakes in this thesis and my girlfriend, Natsuki, whose presence is vital to the development of my creativity and humanity.

I must remember the blessings of my family members, who always supported me. I am very much indebted to my parents for their endless sacrifice, love and affection.

Finally, I would like to dedicate this thesis to my grandfather, who has always been in my center of heart.

Urawa, Saitama, Japan
March, 2007

Daisuke Akamatsu

Contents

I	Generation of Squeezed vacuum	13
1	Squeezed State	15
1.1	Single-mode Electric Field Theory	15
1.1.1	Single-mode Vacuum State	16
1.1.2	Single-mode Coherent State	16
1.1.3	Single-mode Squeezed State	17
1.2	Two-mode Electric Field theory	19
1.2.1	Two-mode Squeezed State	19
1.3	Balanced Homodyne Method with Monochromatic Local Oscillator	20
2	Generation of a Squeezed Vacuum Resonant on Rubidium with Periodically Poled KTiOPO_4	29
2.1	Formalism of Wave Propagation in Nonlinear Medium[68] . . .	29
2.2	Optical Second-Harmonic Generation	30
2.2.1	Quasi Phase Matching	31
2.2.2	Optimal Focusing in a Nonlinear Crystal	32
2.2.3	Second Harmonic Generation with Bow-Tie Cavity . .	33
2.3	Optical Parametric Amplification	34
2.3.1	Generation of Squeezed Vacuum by Sub-threshold Optical Parametric Oscillator	36
2.4	Experiment on Generation of Squeezed Vacuum with PPKTP crystals	41
2.4.1	Second Harmonic Generation with PPKTP crystal . .	41
2.4.2	Optical Parametric Oscillation with PPKTP Crystal .	43
2.4.3	Generation of Squeezed Vacuum with PPKTP Crystal	45
2.5	Discussions	47
2.5.1	The Stability of Cavity	47
2.6	Conclusion	48
II	Electromagnetically Induced Transparency with Squeezed Vacuum	51
3	Electromagnetically Induced Transparency with Squeezed Vacuum	53

3.1	Quantum Description of Electromagnetically Induced Transparency	53
3.1.1	Optical Bloch Equation for Electromagnetically Induced Transparency	53
3.1.2	Absorption Coefficient and Refractive Index by EIT	56
3.2	Experiment on Electromagnetically Induced Transparency with Squeezed Vacuum	56
3.3	Discussion	61
3.4	Conclusion	64
4	Ultraslow Propagation of Squeezed Vacuum with Electromagnetically Induced Transparency	65
4.1	Group Velocity and Transparency Window	65
4.2	Balanced Homodyne Method with Bichromatic Local Oscillator	66
4.3	Experiment on Ultraslow Propagation of Squeezed Vacuum	69
4.3.1	Experiment on Observation of Narrow EIT Window with Squeezed Vacuum	69
4.4	Experiment on Ultraslow Propagation of Squeezed Vacuum	73
4.5	Discussions	77
4.5.1	Evaluation of the delay time	77
4.5.2	Time Dependent Absorption	79
4.6	Conclusion	79
A	Electromagnetically Induced Transparency with a laser-cooled atomic system	83
B	Electric Circuit	87
B.1	Cut-off Frequency of Fast Photodetector with OP Amp	87
B.2	Homodyne Detector	89
B.3	Photodetector for FM Sideband Lock	89
C	Rubidium 87 data	91

Introduction-scope of the thesis

The laser has been at the heart of various fields of research since its invention [1], because of its intensity and coherence. In fact, soon after the birth of the laser, its extraordinary intensity generated optical harmonics [2]. A nonlinear crystal pumped by an intense monochromatic (694.3 nm) laser emitted the second harmonic light (347.2 nm). Since Franken's report, the refractive index and the absorption coefficient of materials have had to be considered variable parameters. The paper marked the beginning of nonlinear optics. This research was followed by a parametric amplification [3], a parametric oscillation [4], a four wave mixing [5, 6], and so on. Recently optical comb generation [7], which plays the main role in frequency measurement of light [8] has widely attracted attention. Optical comb generation is also an extension of the research.

Although P. A. M. Dirac found the beautiful quantum theory of radiation [9], all of the above phenomena can be explained by the semiclassical theory, in which light is treated as a classical electric field. H. P. Yuen introduced the concept of a squeezed state, which one of the main topics in this thesis, and pointed out that the squeezed state can be generated through a degenerate parametric amplification [10]. The squeezed state is one of the *nonclassical* states of light. As squeezed states have potential applications to optical communications [11] and gravitation radiation detectors [12], many experimentalists tried to generate the squeezed states. In 1986, R. E. Slusher, *et. al.*, succeeded in the generation of squeezed vacuum states through parametric amplification using a Dye laser [13]. Squeezed vacuum states have less noise than a vacuum state in one of the field quadratures. The squeezing level increased to 7dB with a sub-threshold parametric oscillator by 2006 [14].

The squeezed vacuum exhibits a number of quantum features and an EPR type-correlated beam can be produced by overlapping two squeezed vacua. Such an EPR beam plays the main role in quantum teleportation [15, 16, 17]. In 1998, A. Furusawa, *et. al.*, successfully demonstrated the unconditional quantum teleportation of a light [18]. Since S. L. Braunstein and his colleagues developed the quantum information theory with continuous variables [19, 20], the squeezed vacuum has been regarded as an important information carrier.

The other important property of the laser is coherence, which is used for coherent manipulation and preparation of the medium. One of the early applications is the *photon echo*, which was demonstrated in 1964 [21]. A

coherently prepared macroscopic electric dipole moment by first laser pulse restores the dephasing after the second laser pulse and emits an echo. The idea of the photon echo came from the spin echo [22], which had been investigated in magneto-resonance. The success of the photon echo means that the laser can be used for the coherent manipulation of dipoles, in the same way as the coherent manipulation of spins by the magnetic field. The optical Bloch equation [23] shows a clear correspondence between atomic dipole manipulation by laser and spin manipulation by a magnetic field.

The optical reaction of atoms dramatically changes through laser-induced coherence of atomic states. The destructive quantum interference between the excitation amplitudes eliminates the absorption at the resonant frequency of a transition. This is referred to as electromagnetically induced transparency (EIT), which is another main issue in this thesis. EIT was first observed by S. E. Harris and his colleagues in 1991 [24, 25]. EIT occurs in a three-level atomic system. When a weak probe light is incident on atoms which are irradiated by an intense control light, the transition amplitudes from the ground states to the excited state destructively interfere and the absorption of the probe light disappears as a result.

EIT provides many interesting phenomena, such as lasers without inversion [26, 27, 28], giant nonlinearity [29, 30, 31, 32], ultraslow light [33, 34, 35, 36], and so on. EIT can also be explained by the semiclassical theory and all of these experiments have been carried out with laser lights, or lights in a coherent state.

M. Fleischhauer and M. D. Lukin treated the probe light as a quantized field and gave the quantum description of the probe light in an EIT medium. The description is termed a dark state polariton [37, 38]. They also found that the speed of the dark state polariton can be controlled by the intensity of the control light and can be stopped by turning off the control light. The stopped dark state polariton can be accelerated by turning on the control light again, and the probe light is retrieved from the medium. The whole process is unitary, therefore ideally the quantum information of photons can be stored in the EIT medium. This is called *storage of light* technique. This paper has attracted attention to the EIT, because the paper provides an easier way to quantum memory.

Quantum Memory — motivation and world trend —

While photons are the fastest and very robust carriers of quantum information, they do not interact with each other and are difficult to localize. In contrast, atoms can interact with each other and can even be stopped by conventional laser cooling techniques but they are not fast carriers of information (Fig1). Therefore one would like to employ atoms to manipulate and store quantum information and photons to carry the information from atoms to atoms. Such a system is termed a quantum network, which was first proposed by J. I. Cirac [39].

A single photon state is often used as a qubit state and is one of the most important ingredients in quantum communications. A conceptually

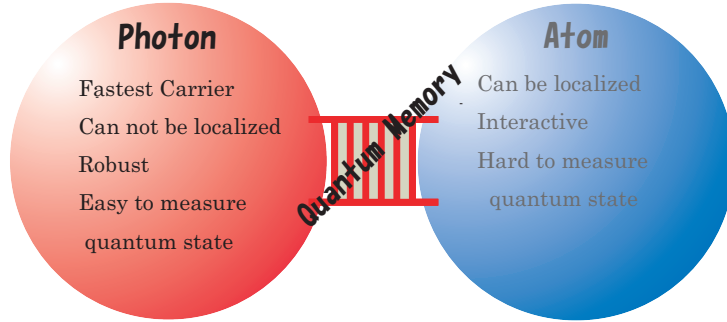


Figure 1: Schematic image of light-atom interface. The disadvantage of photons can be compensated with atoms, and vice versa. As quantum memory connects these two fields, we can cancel the disadvantages of both systems and utilize only advantages with quantum memory.

simple approach to the quantum memory of a single photon is to employ a single two-level atom. It is possible to store and retrieve a single photon state through coherent absorption and emission of a single photon. The interaction Hamiltonian of this process is given by

$$\mathcal{H} = g\hat{a}\hat{\sigma}_{12} + \text{h.c.}, \quad (1)$$

where \hat{a} is the annihilation operator of the light and $\hat{\sigma}_{12}$ is the flipping operator from the atomic states $|2\rangle$ to $|1\rangle$. The interaction strength g is very weak, so placing the atom in a high-Q optical resonator is necessary to effectively increase the interaction [40, 41, 42]. Despite the enormous experimental progress in this field it is technically very challenging to achieve the necessary strong-coupling regime [43, 44, 46].

The proposal by M. Fleischhauer and M. D. Lukin [37, 38] is based on an adiabatic transfer of the quantum state of photons to *collective atomic excitations* with EIT. A collective atomic operator [47] is defined by the sum of the flipping operators of every atom as follows:

$$\tilde{\sigma}_{12} = \frac{1}{\sqrt{N}} \sum_j \hat{\sigma}_{12}^{(j)}. \quad (2)$$

Here N represents the number of atoms. The Hamiltonian describing the interaction between light and atoms is given by

$$\mathcal{H} = g\sqrt{N}\hat{a}\tilde{\sigma}_{12} + \text{h.c.}. \quad (3)$$

The interaction strength between the light and the collective atomic excitation is \sqrt{N} times as large as that between the light and a single atom. This alleviates the experimental requirements with a single-atom cavity QED. In fact, preliminary demonstrations of the proposal were soon carried out independently by two groups [48, 49]. One of the groups also demonstrated that the phase of the stored pulse can be manipulated by applying a magnetic field during storage [50].

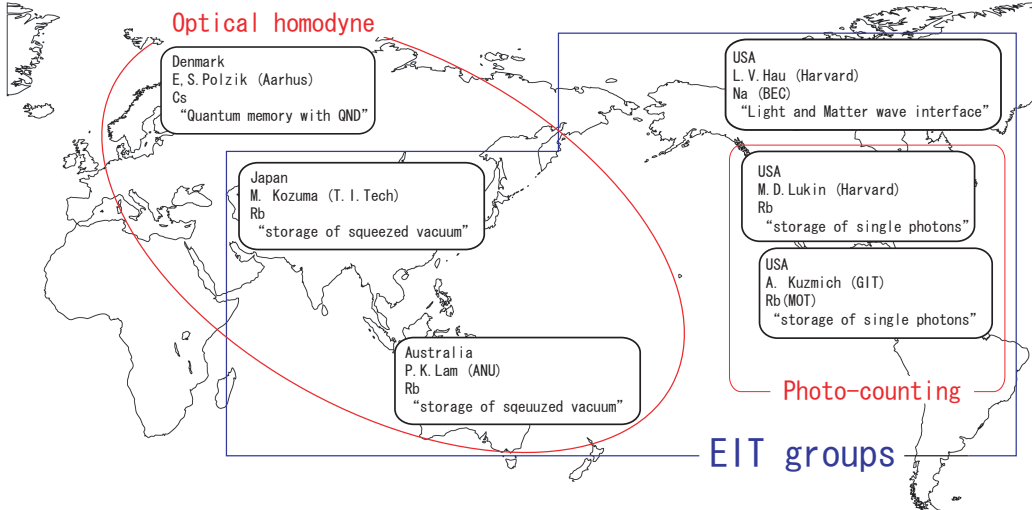


Figure 2: Some groups on quantum memory with atomic ensembles.

Recently several groups have succeeded in storing and retrieving light of single photons with *storage of light* technique [51, 52]. These experiments have demonstrated nonclassical characteristics of the retrieved light field, such as photon antibunching and violation of classical inequalities. Although their demonstrations are large steps towards scalable quantum information processing with single photons, it should be noted that the advantage of quantum memory with atomic ensembles is not only its simplicity of implementation but also its storage capacity. While one can store only single photons with single atoms in a high-Q cavity, atomic ensembles can be used for storage of arbitrary states of photons¹.

Arbitrary states of photons can be converted into those of atoms and vice versa with “genuine” quantum memory, that is, the “genuine” quantum memory connects these two fields. In order to verify such a quantum memory, one has to estimate the density matrix of the light by using homodyne detection. Note that, unlike a photon counting method, homodyne detection is sensitive to the vacuum state. E. S. Polzik and his colleagues are trying to map an arbitrary quantum state of light onto an atomic ensemble from another approach. They utilize quantum nondemolition measurement of atomic spins [53, 54] and verified storage of a coherent state of light with a homodyne method [55], however, their method does not restore the stored state as a radiation field. While some improvement of the system is needed to retrieve the stored state as radiation field [56], the EIT approach can be used for “genuine” quantum memory as it is. Figure 2 schematically shows some groups working on quantum memory with atomic ensembles on the world map.

For demonstration of “genuine” quantum memory with EIT, we adopted a squeezed vacuum state as an input state. The squeezed vacuum carries

¹Strictly speaking, the number of stored photons must be much less than that of atoms.

lower quadrature noise than the coherent state, therefore after storage of the squeezed vacuum, the spin noise of the atomic system is reduced. Such a state is termed “spin squeezed state” [57] and has attracted much attentions [58, 59, 60]. Recently the squeezed vacuum was employed for generation of Schrödinger kitten state [61, 62], therefore storage of squeezed vacuum will leads us to Schrödinger kitten state of atomic systems. The storage of the squeezed vacuum will open the door to a new stage of quantum manipulation of lights and atoms.

The experiment in this thesis is a milestone in the storage of a squeezed vacuum. The thesis is divided into two parts:

- **Generation of a Squeezed Vacuum with Periodically Poled KTiOPO₄ crystals**
- **Electromagnetically Induced Transparency with a Squeezed Vacuum**

In Chapter 1, the basic concept of a squeezed vacuum is presented. To observe a quadrature noise, a balanced homodyne method has been employed for a long time. The theory of the homodyne method is also presented.

In Chapter 2, the experiment on generation of squeezed vacuum resonant on rubidium D₁ line is reported. At the beginning of the research, there were no reports on generation of squeezed vacuum resonant on rubidium. We have developed two methods; one is with periodically poled lithium niobate waveguides, which is not written in this thesis, the other method is with periodically poled KTiOPO₄ crystals in cavities. The observed squeezing level -2.75 dB was the world record at that time. This experimental results can be also seen in [63]

In Chapter 3, the experiment on electromagnetically induced transparency with a squeezed vacuum is presented. This experiment was the first demonstration of EIT with a quantum probe light. A theory of EIT with a quantum probe light is presented before the details of the experiment. The experimental results can also be seen in [64]

In Chapter 4, the experiment on observation of ultraslow propagation of a squeezed vacuum is presented. To observe the squeezed vacuum after passing through the sub-MHz EIT window, we developed a new homodyne method, which enables us to observe the quadrature squeezing of the carrier frequency component. With the new homodyne method, we observed the delay of the squeezed vacuum by $1.3 \mu\text{s}$. Although there are a few reports on the delay of nonclassical light [65, 66], the obtained delay time in our experiment is quite larager than the previous ones.

Part I

Generation of Squeezed vacuum

Chapter 1

Squeezed State

In this chapter, the concept of a squeezed vacuum state is presented. A single-mode squeezed state reduces the field quadrature noise for a certain direction in the phase-space. The single-mode theory is expanded to the two-mode theory, in which the concept of two-mode quadrature is introduced. A two-mode squeezed state is defined as the state, of which two-mode quadrature noise is lower than the vacuum state.

In order to observe a squeezed vacuum, a balanced homodyne method has been employed for a long time. It should be noted that not a single-mode quadrature noise but a two-mode quadrature noise is measured with the conventional homodyne method. A theoretical treatment for the homodyne method is also presented in this chapter.

1.1 Single-mode Electric Field Theory

A quantized single-mode electric field (in a Heisenberg picture) is written as

$$\hat{E}(z, t) = \frac{1}{2} \left[\sqrt{\frac{2\hbar\omega}{\varepsilon_0 V}} \hat{a} \exp(-i(\omega t - kz)) + \text{h.c.} \right], \quad (1.1)$$

where ω , k and V are the angular frequency, the wave number of the field, and the quantization mode volume, respectively. \hat{a} is an annihilation operator of the field and satisfies the following commutation relation,

$$[\hat{a}, \hat{a}^\dagger] = 1. \quad (1.2)$$

(1.1) can be transformed into

$$\hat{E}(z, t) = \sqrt{\frac{2\hbar\omega}{\varepsilon_0 V}} [\hat{x}_\phi \cos(\omega t - kz - \phi) + \hat{x}_{\phi+\pi/2} \sin(\omega t - kz - \phi)], \quad (1.3)$$

with quadrature operators defined as

$$\hat{x}_\phi = \frac{\hat{a}e^{-i\phi} + \hat{a}^\dagger e^{i\phi}}{2}, \quad (1.4)$$

$$\hat{x}_{\phi+\pi/2} = \frac{\hat{a}e^{-i\phi} - \hat{a}^\dagger e^{i\phi}}{2i}. \quad (1.5)$$

The commutation relation between the quadratures is given by

$$[\hat{x}_\phi, \hat{x}_{\phi+\pi/2}] = \frac{i}{2}. \quad (1.6)$$

Therefore the uncertainty relation is written as

$$\langle (\Delta x_\phi)^2 \rangle \langle (\Delta x_{\phi+\pi/2})^2 \rangle \geq \frac{1}{16}, \quad (1.7)$$

where the noise or the variance of the quadrature is defined as

$$\langle (\Delta \hat{x}_\phi)^2 \rangle = \langle \hat{x}_\phi^2 \rangle - \langle \hat{x}_\phi \rangle^2. \quad (1.8)$$

1.1.1 Single-mode Vacuum State

The vacuum state $|0\rangle$ is defined as

$$\hat{a} |0\rangle = 0. \quad (1.9)$$

The expectation value of the electric field and the square of the electric field are calculated as

$$\langle 0 | \hat{E} | 0 \rangle = 0, \quad (1.10)$$

$$\langle 0 | \hat{E}^2 | 0 \rangle = \frac{\hbar\omega}{2\epsilon_0 V}, \quad (1.11)$$

respectively. Therefore the noise of the electric field is given by

$$\langle 0 | (\Delta \hat{E})^2 | 0 \rangle = \frac{\hbar\omega}{2\epsilon_0 V}. \quad (1.12)$$

The expectation value of the quadrature, the square of the quadrature, and the quadrature noise are given by

$$\langle 0 | \hat{x}_\phi | 0 \rangle = 0, \quad (1.13)$$

$$\langle 0 | \hat{x}_\phi^2 | 0 \rangle = \frac{1}{4}, \quad (1.14)$$

$$\langle 0 | (\Delta \hat{x}_\phi)^2 | 0 \rangle = \frac{1}{4}, \quad (1.15)$$

respectively. Since the vacuum state satisfies the equality of (1.7), the vacuum state is one of the minimum uncertainty state with respect to the quadrature.

1.1.2 Single-mode Coherent State

One of the quantum states, which seems closest to a classical picture, is called a coherent state. A coherent state is defined by a displacement operator

$$\hat{D}(\alpha) = \exp(\alpha \hat{a}^\dagger - \alpha^* \hat{a}), \quad (1.16)$$

where $\alpha = |\alpha|e^{i\theta}$. The displacement operator displaces the annihilation operator (creation operator) by α (α^*)¹

$$\hat{D}^\dagger(\alpha)\hat{a}\hat{D}(\alpha) = \hat{a} + \alpha, \quad (1.17)$$

$$\hat{D}^\dagger(\alpha)\hat{a}^\dagger\hat{D}(\alpha) = \hat{a}^\dagger + \alpha^*. \quad (1.18)$$

The coherent state $|\alpha\rangle$ is given by operating the displacement operator to the vacuum state,

$$|\alpha\rangle = \hat{D}(\alpha)|0\rangle. \quad (1.19)$$

Since the quadrature noise of the light in a coherent state is given by

$$\langle\alpha|(\Delta\hat{x}_\phi)^2|\alpha\rangle = \frac{1}{4}, \quad (1.20)$$

the coherent state is also one of the minimum uncertainty state. The expectation value of the electric field of a coherent state is given by

$$\langle\alpha|\hat{E}|\alpha\rangle = \sqrt{\frac{2\hbar\omega}{\epsilon_0 V}}|\alpha|\cos(\omega t - kz - \theta). \quad (1.21)$$

The electric field is proportional to $|\alpha|$. The square of the electric field for the coherent state is given by

$$\langle\alpha|\hat{E}^2|\alpha\rangle = \frac{\hbar\omega}{2\epsilon_0 V} [4|\alpha|^2 \cos^2(\omega t - kz - \theta) + 1], \quad (1.22)$$

and the noise of the electric field is written as

$$\langle\alpha|(\Delta\hat{E})^2|\alpha\rangle = \frac{\hbar\omega}{2\epsilon_0 V}. \quad (1.23)$$

It should be noted that the noise of the electric field of the coherent state is independent on $|\alpha|$ and the same as that of the vacuum state. Since the amplitude of the electric field is proportional to $|\alpha|$, the ratio of the electric field noise to the amplitude of the field is $1/|\alpha|$. This means that the noise of the electric field, which originates the quantization, can be ignored when the light in a coherent state is intense enough. A laser is known as one of the lights in a coherent state.

1.1.3 Single-mode Squeezed State

The quantum theory does not restrict the way to distribute the quadrature noise. We can consider such a state that $\langle(\Delta\hat{x}_\phi)^2\rangle$ is smaller than $1/4$ while $\langle(\hat{x}_{\phi+\pi/2})^2\rangle$ is larger than $1/4$. Such states is called a squeezed state. A single-mode squeezed state is defined by

$$|\psi\rangle_S = \hat{\mathcal{S}}_S(\eta)|0\rangle, \quad (1.24)$$

¹We can prove the formula with Baker-Hausdorff formula: $\exp(\xi\hat{A})\hat{B}\exp(-\xi\hat{A}) = \hat{B} + \xi[\hat{A}, \hat{B}] + \frac{\xi^2}{2!}[\hat{A}, [\hat{A}, \hat{B}]] + \frac{\xi^3}{3!}[\hat{A}, [\hat{A}, [\hat{A}, \hat{B}]]] + \dots + \frac{\xi^n}{n!}[\hat{A}, [\hat{A}, [\hat{A}, \dots [\hat{A}, \hat{B}]]]] + \dots$

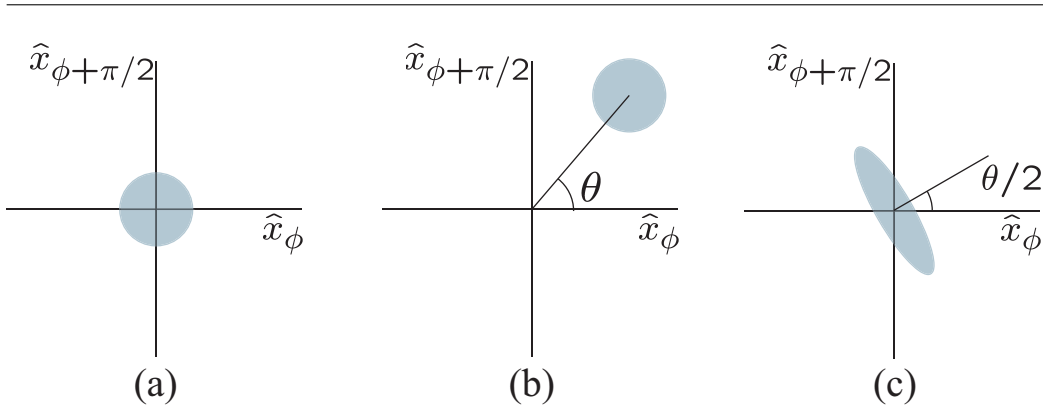


Figure 1.1: Phase-space image showing the uncertainty in (a) a single-mode vacuum state $|0\rangle$, (b) a single-mode coherent state $|\alpha\rangle$, and (c) a single-mode squeezed state $|\psi\rangle$.

with a unitary squeezing operator

$$\hat{\mathcal{S}}_S(\eta) \equiv \exp \left[\frac{1}{2} [\eta^* \hat{a}^2 - \eta (\hat{a}^\dagger)^2] \right], \quad \eta = r e^{i\theta}, \quad (1.25)$$

where r is called a squeezing parameter. The squeezing operator has the following useful transformation properties

$$\hat{\mathcal{S}}_S^\dagger(\eta) \hat{a} \hat{\mathcal{S}}_S(\eta) = \hat{a} \cosh r - \hat{a}^\dagger e^{i\theta} \sinh r, \quad (1.26)$$

$$\hat{\mathcal{S}}_S^\dagger(\eta) \hat{a}^\dagger \hat{\mathcal{S}}_S(\eta) = \hat{a}^\dagger \cosh r - \hat{a} e^{-i\theta} \sinh r. \quad (1.27)$$

The expectation values of the quadrature x_ϕ for the squeezed state is given by

$${}_S \langle \psi | \hat{x}_\phi | \psi \rangle_S = 0, \quad (1.28)$$

$${}_S \langle \psi | \hat{x}_\phi^2 | \psi \rangle_S = \frac{1}{4} (\cosh 2r - \cos(\theta - 2\phi) \sinh 2r). \quad (1.29)$$

When $\theta = 2\phi$, the quadrature noise are simply written as

$${}_S \langle \psi | (\Delta \hat{x}_\phi)^2 | \psi \rangle_S = \frac{1}{4} e^{-2r}, \quad (1.30)$$

$${}_S \langle \psi | (\Delta \hat{x}_{\phi+\pi/2})^2 | \psi \rangle_S = \frac{1}{4} e^{2r}. \quad (1.31)$$

This state satisfies (1.7), *i.e.*, the squeezed state is also one of the minimum uncertainty states and the quadrature noise $\langle (\Delta \hat{x}_\phi)^2 \rangle$ is less than that of the vacuum state when $r > 0$.

1.2 Two-mode Electric Field theory

The two-mode field consisting of $\omega \pm \delta$ can be written as

$$\begin{aligned} \hat{E}(z, t) = & \frac{1}{2\sqrt{2}} \sqrt{\frac{2\hbar\omega}{\varepsilon_0 V}} [\hat{a}_{\omega+\delta} \exp(-i((\omega + \delta)t - kz)) + \text{h.c.}] \\ & + \frac{1}{2\sqrt{2}} \sqrt{\frac{2\hbar\omega}{\varepsilon_0 V}} [\hat{a}_{\omega-\delta} \exp(-i((\omega - \delta)t - kz)) + \text{h.c.}]. \end{aligned} \quad (1.32)$$

The commutation relations between the field operators are given by

$$[\hat{a}_{\omega\pm\delta}, \hat{a}_{\omega\pm\delta}^\dagger] = 1, \quad (1.33)$$

$$[\hat{a}_{\omega\pm\delta}, \hat{a}_{\omega\mp\delta}^{(\dagger)}] = 0. \quad (1.34)$$

(1.32) can be rewritten as

$$\hat{E}(z, t) = \sqrt{\frac{2\hbar\omega}{\varepsilon_0 V}} \left[\hat{X}(\delta, \phi) \cos(\omega t - kz - \phi) + \hat{X}(\delta, \phi + \pi/2) \sin(\omega t - kz - \phi) \right]. \quad (1.35)$$

Here the (Hermite) two-mode quadrature phase amplitudes are

$$\hat{X}(\delta, \phi) = \frac{\hat{a}_{\omega+\delta} e^{-i(\delta t + \phi)} + \hat{a}_{\omega+\delta}^\dagger e^{i(\delta t + \phi)} + \hat{a}_{\omega-\delta} e^{-i(-\delta t + \phi)} + \hat{a}_{\omega-\delta}^\dagger e^{i(-\delta t + \phi)}}{2\sqrt{2}}, \quad (1.36)$$

$$\hat{X}(\delta, \phi + \pi/2) = \frac{\hat{a}_{\omega+\delta} e^{-i(\delta t + \phi)} - \hat{a}_{\omega+\delta}^\dagger e^{i(\delta t + \phi)} + \hat{a}_{\omega-\delta} e^{-i(-\delta t + \phi)} - \hat{a}_{\omega-\delta}^\dagger e^{i(-\delta t + \phi)}}{2\sqrt{2}i}. \quad (1.37)$$

The commutation relation between two-mode quadratures is given by

$$[\hat{X}(\delta, \phi), \hat{X}(\delta, \phi + \pi/2)] = \frac{i}{2}, \quad (1.38)$$

and the uncertainty inequality is written as

$$\langle (\Delta \hat{X}(\delta, \phi))^2 \rangle \langle (\Delta \hat{X}(\delta, \phi + \pi/2))^2 \rangle \geq \frac{1}{16}. \quad (1.39)$$

1.2.1 Two-mode Squeezed State

In the previous section, we discussed a squeezed vacuum state consisting of a single mode \hat{a} . In this section, we expand the concept to the two-mode state. The two-mode squeezed vacuum is defined as

$$|\psi\rangle_T = \hat{\mathcal{S}}_T(\eta)|0\rangle, \quad (1.40)$$

where a two-mode squeezing operator $\hat{\mathcal{S}}_T$ is given by

$$\hat{\mathcal{S}}_T(\eta) \equiv \exp(\eta^* \hat{a}_{\omega+\delta} \hat{a}_{\omega-\delta} - \eta \hat{a}_{\omega+\delta}^\dagger \hat{a}_{\omega-\delta}^\dagger), \quad \eta = r e^{i\theta}. \quad (1.41)$$

The following commutation relation

$$[\eta\hat{a}_{\omega+\delta}^\dagger\hat{a}_{\omega-\delta}^\dagger - \eta^*\hat{a}_{\omega+\delta}\hat{a}_{\omega-\delta}, \hat{a}_{\omega\pm\delta}] = -\eta\hat{a}_{\omega\mp\delta}^\dagger, \quad (1.42)$$

generates a useful formula

$$\begin{aligned} \hat{\mathcal{S}}_T^\dagger(\eta)\hat{a}_{\omega\pm\delta}\hat{\mathcal{S}}_T(\eta) &= \exp(\eta\hat{a}_{\omega+\delta}^\dagger\hat{a}_{\omega-\delta}^\dagger - \eta^*\hat{a}_{\omega+\delta}\hat{a}_{\omega-\delta})\hat{a}_{\omega\pm\delta}\exp(\eta^*\hat{a}_{\omega+\delta}\hat{a}_{\omega-\delta} - \eta\hat{a}_{\omega+\delta}^\dagger\hat{a}_{\omega-\delta}^\dagger) \\ &= \hat{a}_{\omega\pm\delta} + [\eta\hat{a}_{\omega+\delta}^\dagger\hat{a}_{\omega-\delta}^\dagger - \eta^*\hat{a}_{\omega+\delta}\hat{a}_{\omega-\delta}, \hat{a}_{\omega\pm\delta}] \\ &+ \frac{1}{2!}[\eta\hat{a}_{\omega+\delta}^\dagger\hat{a}_{\omega-\delta}^\dagger - \eta^*\hat{a}_{\omega+\delta}\hat{a}_{\omega-\delta}, [\eta\hat{a}_{\omega+\delta}^\dagger\hat{a}_{\omega-\delta}^\dagger - \eta^*\hat{a}_{\omega+\delta}\hat{a}_{\omega-\delta}, \hat{a}_{\omega\pm\delta}]] + \dots \\ &= \hat{a}_{\omega\pm\delta} - \eta\hat{a}_{\omega\mp\delta}^\dagger + \frac{1}{2!}\eta\eta^*\hat{a}_{\omega\pm\delta} - \frac{1}{3!}\eta^2\eta^*\hat{a}_{\omega\mp\delta}^\dagger + \frac{1}{4!}\eta^2\eta^{*2}\hat{a}_{\omega\pm\delta} - \dots \\ &= \hat{a}_{\omega\pm\delta} - r e^{i\theta}\hat{a}_{\omega\mp\delta}^\dagger + \frac{1}{2!}r^2\hat{a}_{\omega\pm\delta} - \frac{1}{3!}r^3 e^{i\theta}\hat{a}_{\omega\mp\delta}^\dagger + \frac{1}{4!}r^4\hat{a}_{\omega\pm\delta} - \dots \\ &= \hat{a}_{\omega\pm\delta} \cosh r - \hat{a}_{\omega\mp\delta}^\dagger e^{i\theta} \sinh r, \end{aligned} \quad (1.43)$$

with Baker-Hausdorff formula.

Since the expectation values of the two-mode quadrature noise and the square thereof are written as

$${}_T\langle\psi|\hat{X}(\delta, \phi)|\psi\rangle_T = 0, \quad (1.44)$$

$${}_T\langle\psi|\hat{X}^2(\delta, \phi)|\psi\rangle_T = \frac{1}{4}(\cosh 2r - \cos(\theta - 2\phi) \sinh 2r), \quad (1.45)$$

respectively, the two-mode quadrature noise is given by

$${}_T\langle\psi|(\Delta\hat{X}(\delta, \phi))^2|\psi\rangle_T = \frac{1}{4}(\cosh 2r - \cos(\theta - 2\phi) \sinh 2r). \quad (1.46)$$

When $\theta = 2\phi$, the quadrature noise is written as

$${}_T\langle\psi|(\Delta\hat{X}(\delta, \phi))^2|\psi\rangle_T = \frac{1}{4}e^{-2r}, \quad (1.47)$$

$${}_T\langle\psi|(\Delta\hat{X}(\delta, \phi + \pi/2))^2|\psi\rangle_T = \frac{1}{4}e^{2r}. \quad (1.48)$$

The quadrature noise of the two-mode vacuum state is given by

$${}_T\langle 0|(\Delta\hat{X}(\delta, \phi))^2|0\rangle_T = \frac{1}{4}, \quad (1.49)$$

therefore $\langle(\Delta\hat{X}(\delta, \phi))^2\rangle$ is smaller than that of vacuum state, when $r > 0$.

1.3 Balanced Homodyne Method with Monochromatic Local Oscillator

In order to measure the quadrature noise of a signal light, an optical balanced homodyne method has been employed for a long time. The method is schematically shown in Fig. 1.3. A signal beam \hat{a}_S is mixed on the beam

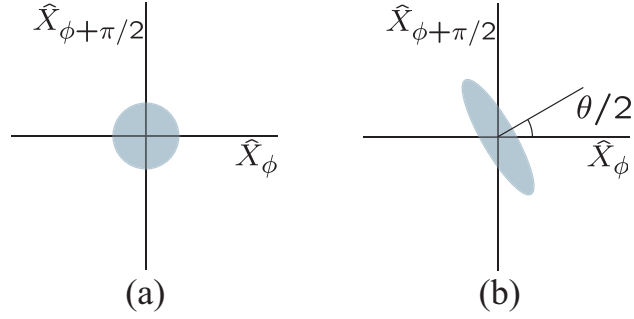


Figure 1.2: Phase-space image showing the uncertainty in (a) a two-mode vacuum state $|0\rangle$, (b) a two-mode squeezed state $|\psi\rangle$.

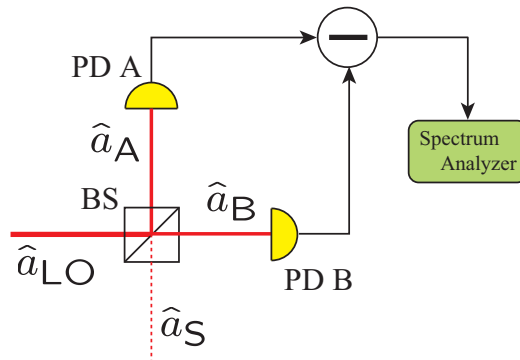


Figure 1.3: A schematic of a homodyne method. A local oscillator light is in a single-mode coherent state. The power of the differential current is measured by a spectrum analyzer.

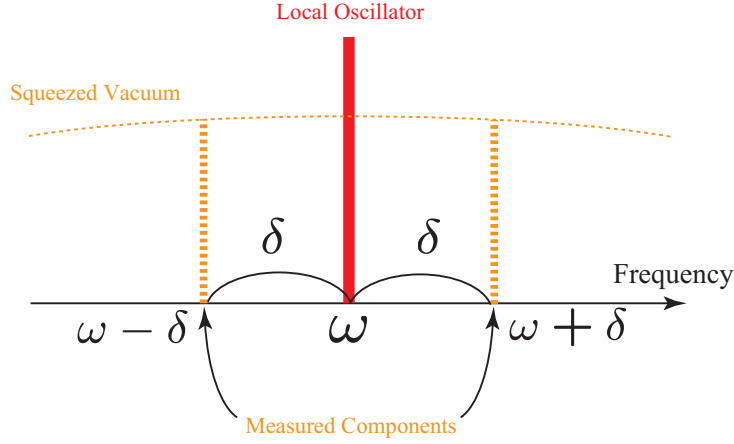


Figure 1.4: Schematic image of a homodyne method with a monochromatic local oscillator. The measured frequency components of the squeezed vacuum are $\omega \pm \delta$.

splitter with a monochromatic local oscillator \hat{a}_{LO} in a coherent state. Each output $\hat{a}_{\text{A,B}}$ is detected by the photodetectors A and B, respectively, and the power spectrum of the differential current is measured by a spectrum analyzer. From the input-output relation of the beam splitter, the output fields can be written as

$$\hat{a}_{\text{A}}(t) = \frac{1}{\sqrt{2}}\{\hat{a}_{\text{LO}}(t) + i\hat{a}_{\text{S}}(t)\}, \quad (1.50)$$

$$\hat{a}_{\text{B}}(t) = \frac{1}{\sqrt{2}}\{i\hat{a}_{\text{LO}}(t) + \hat{a}_{\text{S}}(t)\}, \quad (1.51)$$

respectively. Since the local oscillator light is in a coherent state, the annihilation operator of the field can be treated as a complex variable

$$\hat{a}_{\text{LO}}(t) = \alpha e^{-i\omega t}, \quad (1.52)$$

$$\alpha = |\alpha_{\text{mono}}| e^{i\theta}. \quad (1.53)$$

Usually a squeezed vacuum generated by nonlinear crystal is broad ($\Delta\omega > 10\text{MHz}$). We can, however, ignore the frequency components of the signal field other than $\hat{a}_{\omega\pm\delta} e^{i(\omega\pm\delta)t}$, since the spectrum analyzer measures a power of a beat δ (Fig. 1.4). Therefore the signal field can be written as

$$\hat{a}_{\text{S}}(t) = \hat{a}_{\omega+\delta} e^{-i(\omega+\delta)t} + \hat{a}_{\omega-\delta} e^{-i(\omega-\delta)t}. \quad (1.54)$$

(1.52) and (1.54) are substituted into (1.50) and (1.51), and we obtain

$$\hat{a}_{\text{A}}(t) = \frac{1}{\sqrt{2}}(\alpha e^{-i\omega t} + i\hat{a}_{\omega+\delta} e^{-i(\omega+\delta)t} + i\hat{a}_{\omega-\delta} e^{-i(\omega-\delta)t}), \quad (1.55)$$

$$\hat{a}_{\text{B}}(t) = \frac{1}{\sqrt{2}}(i\alpha e^{-i\omega t} + \hat{a}_{\omega+\delta} e^{-i(\omega+\delta)t} + \hat{a}_{\omega-\delta} e^{-i(\omega-\delta)t}). \quad (1.56)$$

The differential current between PD A and PD B is given by

$$\begin{aligned}
\Delta\hat{I} &= C(\hat{a}_A^\dagger(t)\hat{a}_A(t) - \hat{a}_B^\dagger(t)\hat{a}_B(t)) \\
&= iC[(\alpha^*\hat{a}_{\omega+\delta} - \alpha\hat{a}_{\omega-\delta}^\dagger)e^{-i\delta t} + (\alpha^*\hat{a}_{\omega-\delta} - \alpha\hat{a}_{\omega+\delta}^\dagger)e^{i\delta t}] \\
&= C|\alpha_{\text{mono}}|[\hat{a}_{\omega+\delta}e^{-i(\delta t+(\theta-\pi/2))} + \hat{a}_{\omega+\delta}^\dagger e^{i(\delta t+(\theta-\pi/2))} \\
&\quad + \hat{a}_{\omega-\delta}e^{-i(-\delta t+(\theta-\pi/2))} + \hat{a}_{\omega-\delta}^\dagger e^{i(-\delta t+(\theta-\pi/2))}] \\
&= 2\sqrt{2}C|\alpha_{\text{mono}}|\hat{X}(\delta, \theta - \pi/2), \tag{1.57}
\end{aligned}$$

where two-mode quadrature $\hat{X}(\delta, \theta)$ is defined by (1.37). According to the Wiener-Khintchine theorem, the spectral density function $\langle \hat{S}_{\text{mono}} \rangle$ of $\Delta\hat{I}$ is given by

$$\langle \hat{S}_{\text{mono}}(\delta') \rangle = \frac{1}{\pi} \int_{-\infty}^{\infty} d\tau \langle \Delta\hat{I}(t)\Delta\hat{I}(t+\tau) \rangle \cos \delta'\tau. \tag{1.58}$$

Substituting (1.57) into (1.58), we obtain

$$\langle \hat{S}_{\text{mono}}(\delta') \rangle = 8(C|\alpha_{\text{mono}}|)^2 \langle \hat{X}^2(\delta, \theta - \pi/2) \rangle \delta(\delta' - \delta), \tag{1.59}$$

where $\delta(\delta' - \delta)$ is the Dirac delta function. If the signal field is in a vacuum state, the measured noise is given by

$$\langle \hat{S}_{\text{mono}}(\delta, \theta) \rangle_{\text{vac}} = 2(C|\alpha_{\text{mono}}|)^2. \tag{1.60}$$

The power spectrum of the differential current normalized by vacuum noise level is given by

$$\hat{\mathcal{S}}_{\text{mono}}(\delta, \theta) = 4\hat{X}^2(\delta, \theta - \pi/2). \tag{1.61}$$

It should be noted that the quadrature noise of various directions can be measured by changing the phases of the local oscillator.

When the signal state $|\psi\rangle$ is a two-mode squeezed vacuum state, the expectation value of the power spectrum is written as

$$\langle \psi | \hat{\mathcal{S}}_{\text{mono}}(\delta, \theta) | \psi \rangle = \cosh 2r - \cos(\phi - 2\theta + \pi) \sinh 2r. \tag{1.62}$$

As discussed in the next chapter, ϕ represents the phase of the pump field in the optical parametric amplifier. Without any loss of generality, we can set $\phi = \pi$. Figure 1.5 shows the dependence of the normalized noise power on the phase of the local oscillator θ when the squeezing parameter $r = 0.3$. The maximum squeezing (-2.6 dB) and antisqueezing ($+2.6$ dB) can be observed when $\theta = 0$ and $\theta = \pi/2$, respectively.

Spatial overlapping of signal beam with local oscillator

In the previous discussion, we did not consider the spatial modes of the signal light and the local oscillator light, which has, implicitly, been assumed to be exactly the same. As the homodyne method measures the quadrature

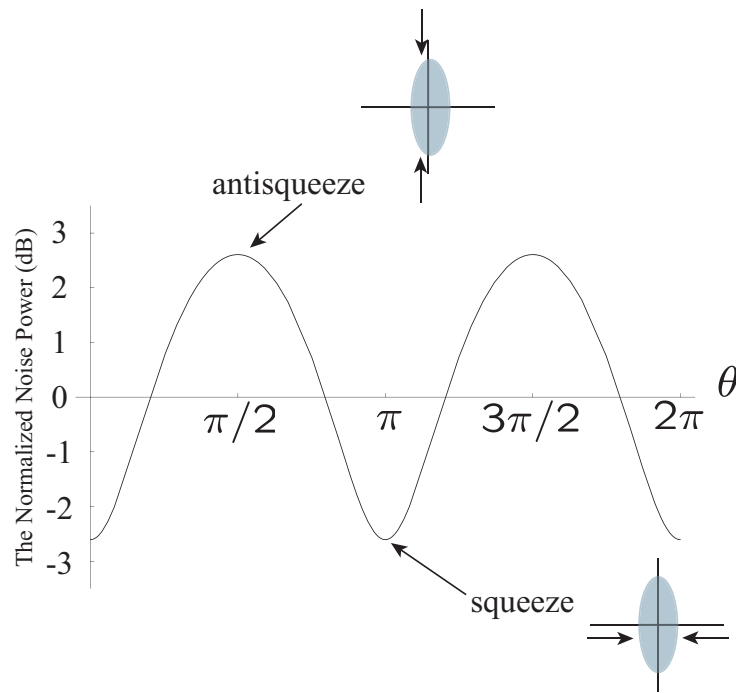


Figure 1.5: The dependence of the normalized power on the phase of the local oscillator with the picture of the phase space image. The squeezing parameter $r=0.3$. The normalized noise power is usually expressed with the unit of dB, *i.e.*, $10 \log_{10} \langle \hat{S} \rangle$ (dB).

noise of the field of the same spatial mode as that of the local oscillator, the spatial overlapping between the signal light and the local oscillator is very important. Let ξ be the spatial overlap of the local oscillator with the signal beam². The local oscillator is divided into the two modes.

$$\hat{a}_{\text{LO}} = \xi \hat{a}_{\text{LO}}^{\parallel} + \sqrt{1 - \xi^2} \hat{a}_{\text{LO}}^{\perp}, \quad (1.63)$$

where the spatial mode of $\hat{a}_{\text{LO}}^{\parallel}$ is exactly same as the signal beam, whereas the spatial mode of $\hat{a}_{\text{LO}}^{\perp}$ is orthogonal to that of the signal beam. (1.50) and (1.51) can also be divided into two modes

$$\hat{a}_{\text{A}}^{\parallel}(t) = \frac{1}{\sqrt{2}} \{ \hat{a}_{\text{LO}}^{\parallel}(t) + i \hat{a}_{\text{S}}^{\parallel}(t) \}, \quad (1.64)$$

$$\hat{a}_{\text{B}}^{\parallel}(t) = \frac{1}{\sqrt{2}} \{ i \hat{a}_{\text{LO}}^{\parallel}(t) + \hat{a}_{\text{S}}^{\parallel}(t) \}, \quad (1.65)$$

$$\hat{a}_{\text{A}}^{\perp}(t) = \frac{1}{\sqrt{2}} \{ \hat{a}_{\text{LO}}^{\perp}(t) + i \hat{a}_{\text{S}}^{\perp}(t) \}, \quad (1.66)$$

$$\hat{a}_{\text{B}}^{\perp}(t) = \frac{1}{\sqrt{2}} \{ i \hat{a}_{\text{LO}}^{\perp}(t) + \hat{a}_{\text{S}}^{\perp}(t) \}. \quad (1.67)$$

The parallel and orthogonal annihilation operators of the local oscillator in a coherent state are written as

$$\hat{a}_{\text{LO}}^{\parallel}(t) = \xi \alpha e^{-i\omega t}, \quad (1.68)$$

$$\hat{a}_{\text{LO}}^{\perp}(t) = \sqrt{1 - \xi^2} \alpha e^{-i\omega t}, \quad (1.69)$$

respectively. The power of the differential current can be given by

$$\hat{\mathcal{S}}_{\text{mono}}(\delta, \theta) = \xi^2 \hat{\mathcal{S}}_{\text{mono}}^{\parallel}(\delta, \theta) + (1 - \xi^2) \hat{\mathcal{S}}_{\text{mono}}^{\perp}(\delta, \theta), \quad (1.70)$$

with

$$\hat{\mathcal{S}}_{\text{mono}}^{\parallel(\perp)}(\delta, \theta) = 8(C|\alpha_{\text{mono}}| \hat{X}^{\parallel(\perp)}(\delta, \theta))^2, \quad (1.71)$$

where $\hat{X}^{\parallel(\perp)}$ represents the quadrature noise of the mode parallel (orthogonal) to the local oscillator. Since the state, to which \hat{X}^{\perp} operates, is a vacuum, the normalized power spectrum of the differential current is given by

$$\hat{\mathcal{S}}_{\text{mono}}(\delta, \theta) = 4\xi^2 (\hat{X}^{\parallel}(\delta, \theta))^2 + 1 - \xi^2. \quad (1.72)$$

The above discussion can be expanded to the case which a squeezed vacuum experiences the intensity loss L before the homodyne detector. The expression of the normalized power spectrum is written as

$$\hat{\mathcal{S}}_{\text{mono}}(\delta, \theta) = 4\zeta (\hat{X}^{\parallel}(\delta, \theta))^2 + 1 - \zeta, \quad (1.73)$$

where we introduce the detection efficiency factor $\zeta = (1 - L)\xi^2$. Figure 1.6 shows the dependence of the power spectrum on the phase of the local oscillator θ when the squeezing parameter $r = 0.3$, the visibility $\xi = 0.95$,

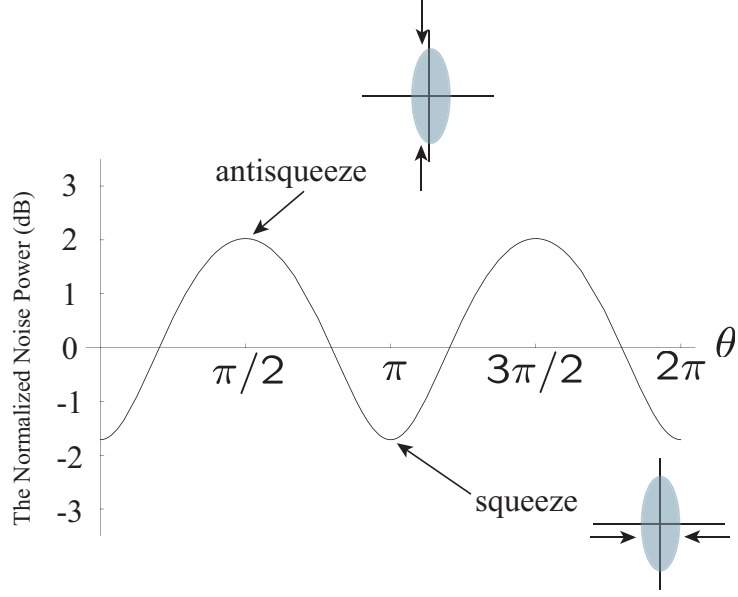


Figure 1.6: The dependence of the power spectrum on the phase of the local oscillator with the picture of the phase space image. The squeezing parameter $r = 0.3$, the visibility $\xi = 0.95$, and the loss $L = 0.2$.

and the loss $L = 0.2$. The maximum squeezing (-1.7 dB) and antisqueezing ($+2.0$ dB) is observed by varying the phase of the local oscillator. It should be noted that the squeezing level decreases by 0.9 dB ($=2.6\text{dB} - 1.7\text{dB}$), while the antisqueezing level decreases by only 0.6 dB ($=2.6\text{ dB} - 2.0\text{ dB}$). The squeezing is more sensitive to the optical loss or visibility than the antisqueezing.

This fact can be understood as follows. In quantum theory of radiation, the loss means not only reduction of the number of the photons, but also invasion of the vacuum noise. Consider a pure squeezed vacuum of which quadrature noises are given

$$\langle \hat{x}_\phi^2 \rangle = \frac{1}{8} \quad \left(= \frac{1}{2} \times \langle 0 | \hat{x}_\phi^2 | 0 \rangle \right), \quad (1.74)$$

$$\langle \hat{x}_{\phi+\pi/2}^2 \rangle = \frac{1}{2} \quad \left(= 2 \times \langle 0 | \hat{x}_\phi^2 | 0 \rangle \right), \quad (1.75)$$

respectively. In other words, the squeezing and the antisqueezing level of the squeezed vacuum are -3.0 dB and $+3.0$ dB, respectively. If half of the squeezed vacuum is absorbed and the vacuum noise is injected to the state

² ξ is also called as a visibility.

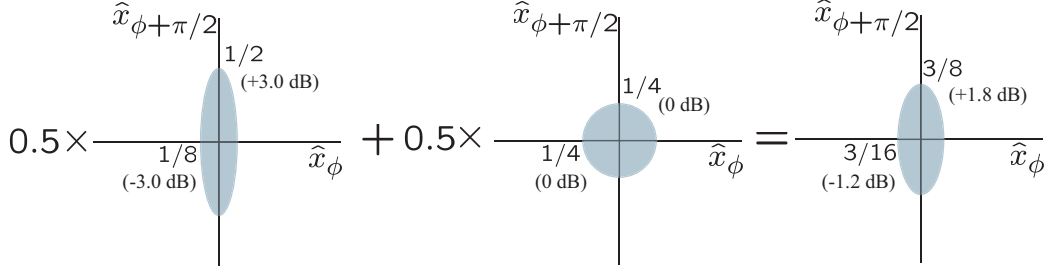


Figure 1.7: Schematic diagram of loss. The -3dB -squeezed vacuum passes through the loss $L = 0.5$. After the absorption, the observed squeezing level is decreases to -1.2 dB .

(Fig. 1.7), the quadrature noise changes to

$$\langle \hat{x}_\phi^2 \rangle \rightarrow 0.5 \times \frac{1}{8} + 0.5 \times \frac{1}{4} = \frac{3}{16}, \quad (1.76)$$

$$\langle \hat{x}_{\phi+\pi/2}^2 \rangle \rightarrow 0.5 \times \frac{1}{2} + 0.5 \times \frac{1}{4} = \frac{3}{8}, \quad (1.77)$$

respectively. In other words, the squeezing and the antisqueezing level of the squeezed vacuum changes -1.2 dB and $+1.8\text{ dB}$, respectively. While the squeezing level changes by 1.8 dB , the antisqueezing level decreases by only 1.2 dB . This difference increases if the initial squeezing level is higher. A high level squeezed vacuum is very sensitive to optical loss. From a simple consideration, more than -3 dB squeezing can not be obtained with the existence of 50% -loss.

The dependences of the maximum squeezing and antisqueezing on the detection efficiency are shown in Fig. 1.8 with the squeezing parameter $r = 0.3$.

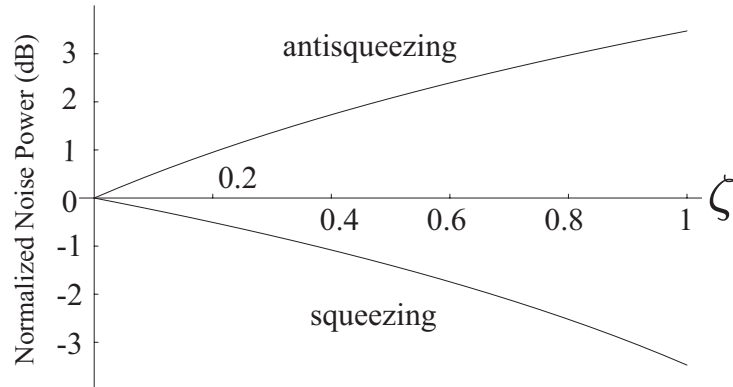


Figure 1.8: The dependence of the power spectrum on the detection efficiency ζ . The squeezing parameter $r = 0.3$.

Chapter 2

Generation of a Squeezed Vacuum Resonant on Rubidium with Periodically Poled KTiOPO₄

We succeeded in the generation of a continuous-wave squeezed vacuum resonant on the Rb D₁ line (795nm) using periodically poled KTiOPO₄ crystals in cavities. We observed a squeezing level of -2.75 ± 0.14 dB and an anti-squeezing level of $+7.00 \pm 0.13$ dB.

To generate a squeezed vacuum, we have to construct two inevitable parts, *i.e.*, a doubler, and an optical parametric amplifier (squeezer). The theory of the second nonlinear optics in the cavity is presented before the details of the experiment.

2.1 Formalism of Wave Propagation in Non-linear Medium[68]

First we derive equations describing a light propagating in a nonlinear medium. Generally the polarization of a medium loses proportionality to the field under an intense light. Such an intense light induces a nonlinear polarization, proportional to the second or higher order of the field. The polarization \mathbf{P} can be divided into linear \mathbf{P}_L and nonlinear \mathbf{P}_{NL}

$$\mathbf{P} = \mathbf{P}_L + \mathbf{P}_{NL}, \quad (2.1)$$

where

$$\mathbf{P}_L = \varepsilon_0 \chi^{(1)} \cdot \mathbf{E}, \quad (2.2)$$

$$\mathbf{P}_{NL} = \varepsilon_0 \chi^{(2)} \cdot \mathbf{E}\mathbf{E} + \varepsilon_0 \chi^{(3)} \cdot \mathbf{E}\mathbf{E}\mathbf{E} + \dots \quad (2.3)$$

Here $\chi^{(i)}$ is the i th order susceptibility, which is generally $(i + 1)$ th order tensor. From Maxwell equations, the electromagnetic wave propagation in a

medium is described by

$$\nabla^2 \mathbf{E} - \mu_0 \varepsilon \frac{\partial^2 \mathbf{E}}{\partial t^2} = \mu_0 \frac{\partial^2 \mathbf{P}_{NL}}{\partial t^2}, \quad (2.4)$$

where $\varepsilon = \varepsilon_0(1 + \chi^{(1)})$. In the following discussion, we focus on the second order nonlinear effect, so we ignore the higher order effect. For simplicity, let us limit our consideration to a field made up of three x-polarized plane waves propagating in the z direction with frequencies ω_1 , ω_2 , and ω_3 according to

$$E^{(\omega_1)}(z, t) = \frac{1}{2} \mathcal{E}_1(z) e^{i(\omega_1 t - k_1 z)} + \text{c.c.}, \quad (2.5)$$

$$E^{(\omega_2)}(z, t) = \frac{1}{2} \mathcal{E}_2(z) e^{i(\omega_2 t - k_2 z)} + \text{c.c.}, \quad (2.6)$$

$$E^{(\omega_3)}(z, t) = \frac{1}{2} \mathcal{E}_3(z) e^{i(\omega_3 t - k_3 z)} + \text{c.c.}. \quad (2.7)$$

Here \mathcal{E}_i is a slowly varying complex amplitude and we ignore its time dependence. The total instantaneous field is, then,

$$E(z, t) = E^{(\omega_1)}(z, t) + E^{(\omega_2)}(z, t) + E^{(\omega_3)}(z, t). \quad (2.8)$$

In order to couple the fields through the nonlinear polarization, we assume that $\omega_3 = \omega_1 + \omega_2$. Furthermore, $\chi^{(2)}$ is assumed to be a scalar, and \mathbf{P} to be parallel to x axis. (2.4) can be rewritten as

$$\nabla^2 E(z, t) - \mu_0 \varepsilon \frac{\partial^2 E(z, t)}{\partial t^2} = \mu_0 \varepsilon_0 \chi^{(2)} \frac{\partial^2}{\partial t^2} (E(z, t)^2). \quad (2.9)$$

We substitute (2.8) into the wave equation (2.9) with (2.5)-(2.7), and separate the resulting equation into three equations, each containing only terms oscillating at one of the three frequencies. Using the slowly varying amplitude and phase approximation (SVAP), we obtain the basic equations describing second order nonlinear interactions:

$$\frac{d\mathcal{E}_1}{dz} = -\frac{i\omega_1}{2} \sqrt{\frac{\mu_0}{\varepsilon}} \varepsilon_0 \chi^{(2)} \mathcal{E}_3 \mathcal{E}_2^* e^{-i(k_3 - k_2 - k_1)z}, \quad (2.10)$$

$$\frac{d\mathcal{E}_2^*}{dz} = \frac{i\omega_2}{2} \sqrt{\frac{\mu_0}{\varepsilon}} \varepsilon_0 \chi^{(2)} \mathcal{E}_2 \mathcal{E}_3^* e^{-i(k_1 - k_3 + k_2)z}, \quad (2.11)$$

$$\frac{d\mathcal{E}_3}{dz} = -\frac{i\omega_3}{2} \sqrt{\frac{\mu_0}{\varepsilon}} \varepsilon_0 \chi^{(2)} \mathcal{E}_1 \mathcal{E}_2 e^{-i(k_1 + k_2 - k_3)z}. \quad (2.12)$$

2.2 Optical Second-Harmonic Generation

Irradiation of a nonlinear crystal by an intense laser light (fundamental light) generates the second harmonic wave. The second harmonic generation process can be described by using (2.10)-(2.12). The frequency of a fundamental light is ω and the amplitude is $\mathcal{E}^{(\omega)}$, then we put $\omega_1 = \omega_2 = \omega$ and

$\mathcal{E}_1 = \mathcal{E}_2 = \mathcal{E}^{(\omega)}$. The second harmonic light is represented by $\mathcal{E}_3 = \mathcal{E}^{(2\omega)}$ and $\omega_3 = 2\omega$. (2.12) is transformed into

$$\frac{d\mathcal{E}^{(2\omega)}}{dz} = -i\omega\sqrt{\frac{\mu_0}{\varepsilon}}\varepsilon_0\chi^{(2)}(\mathcal{E}^{(\omega)})^2 e^{i\Delta kz}, \quad (2.13)$$

where $\Delta k = k_3 - 2k_1$. For simplicity, we ignore the depletion of the fundamental light due to conversion to the second harmonic light. We can easily integrate the equation, and the amplitude of the second harmonic light at the end facet of the crystal $z = d$ is written as

$$\mathcal{E}^{(2\omega)}(d) = -i\omega\sqrt{\frac{\mu_0}{\varepsilon}}\varepsilon_0\chi^{(2)}(\mathcal{E}^{(\omega)})^2 \frac{e^{i\Delta kd} - 1}{i\Delta k}. \quad (2.14)$$

The output power of the second harmonic light is given by

$$\mathcal{I}^{(2\omega)}(d) = \frac{1}{2}c\varepsilon_0|\mathcal{E}^{(2\omega)}|^2 = \left(\frac{\mu_0}{\varepsilon}\right)^{3/2}(\omega\varepsilon_0\chi^{(2)})^2(\mathcal{I}^{(\omega)})^2 d^2 \frac{\sin^2(\Delta kd/2)}{(\Delta kd/2)^2}. \quad (2.15)$$

The power of second harmonic light is proportional to the square of that of the fundamental light. We define the conversion efficiency

$$\eta = \frac{\mathcal{I}^{(2\omega)}}{(\mathcal{I}^{(\omega)})^2} = \left(\frac{\mu_0}{\varepsilon}\right)^{3/2}(\omega\varepsilon_0\chi^{(2)})^2 d^2 \frac{\sin^2(\Delta kd/2)}{(\Delta kd/2)^2}, \quad (2.16)$$

and the loss factor due to the conversion

$$\beta = \frac{\mathcal{I}^{(2\omega)}}{\mathcal{I}^{(\omega)}} = \left(\frac{\mu_0}{\varepsilon}\right)^{3/2}(\omega\varepsilon_0\chi^{(2)})^2 \mathcal{I}^{(\omega)} d^2 \frac{\sin^2(\Delta kd/2)}{(\Delta kd/2)^2}. \quad (2.17)$$

2.2.1 Quasi Phase Matching

The phase of nonlinear polarization evolves by $2k_1$, and that of electric wave by k_3 . $\Delta k = k_3 - 2k_1$ represents the discrepancy of the wave number of nonlinear polarization from that of the electric wave. When $2k_1 = k_3$, these phases *get into step*. This condition is referred to as phase matching condition. Whereas the intensity of the field grows up by z^2 when $\Delta k = 0$, the function of the intensity is periodic when $\Delta k \neq 0$, so the intensity is suppressed.

The refraction index normally increases with ω , or k . One of the techniques to satisfy the phase matching condition takes advantage of the natural birefringence of anisotropic crystals. In practice, to generate a squeezed vacuum resonant on cesium the birefringence of KNbO₃ has been widely used.

In our experiment, we adopted an alternative technique for the phase matching proposed by Yariv[69]. The method, which is referred to as quasi phase-matching, utilizes a crystal of which the nonlinear coefficient is periodically modulated by reversing the direction of one of its principal axes periodically. The periodic nonlinear coefficient $\chi^{(2)}(z)$ can be expanded in a

Fourier series

$$\chi^{(2)}(z) = \chi_0^{(2)} \left[\sum_{m=-\infty}^{\infty} a_m \exp \left(im \frac{2\pi}{\Lambda} z \right) \right], \quad (2.18)$$

$$a_m = \frac{1}{\Lambda} \int_0^\Lambda \frac{\chi^{(2)}(z)}{\chi_0^{(2)}} \exp \left(-im \frac{2\pi}{\Lambda} z \right) dz, \quad (2.19)$$

where Λ represents the period of $\chi^{(2)}(z)$. Substituting (2.18) into (2.10), we obtain

$$\frac{d\mathcal{E}_1}{dz} = -\frac{i\omega_1}{2} \sqrt{\frac{\mu_0}{\varepsilon}} \varepsilon_0 \chi_0^{(2)} \mathcal{E}_3 \mathcal{E}_2^* \sum_{m=-\infty}^{\infty} a_m \exp \left[i \left(m \frac{2\pi}{\Lambda} - k_3 + k_2 + k_1 \right) z \right]. \quad (2.20)$$

If some integer m satisfies

$$m \frac{2\pi}{\Lambda} = k_3 - k_2 - k_1, \quad (2.21)$$

phase matching is obtained. It should be noted that we can ignore non-phase-matched terms in (2.18), since their contribution averages out to zero over the long integration of z . When $\chi^{(2)}(z)$ switches from $\chi_0^{(2)}$ to $-\chi_0^{(2)}$ every $\Lambda/2$,

$$a_m = \frac{1 - \cos m\pi}{m\pi}, \quad (2.22)$$

so that choosing $m = 1$, the effective nonlinear constant is

$$\chi_{\text{eff}}^{(2)} = a_1 \chi_0^{(2)} = \frac{2}{\pi} \chi_0^{(2)}. \quad (2.23)$$

2.2.2 Optimal Focusing in a Nonlinear Crystal

The discussion in 2.2 is based on a plane wave model, so we do not care about the interaction volume. In practice, Gaussian beams, which have finite cross sections, are widely used. The confocal length $z_0 = \pi w_0^2 n / \lambda$ characterizes the distance from the beam waist in which the beam area is double that of the waist. If the crystal is much shorter than the confocal length, we can ignore the spread of the beam, and the conversion efficiency is given by

$$\eta = \left(\frac{\mu_0}{\varepsilon} \right)^{3/2} \frac{(\omega \varepsilon_0 \chi^{(2)} d)^2 \sin^2(\Delta k d / 2)}{\pi w_0^2 (\Delta k d / 2)^2}. \quad (2.24)$$

The beam of smaller waist gives a larger conversion efficiency. If the length of the crystal is comparable to or longer than the confocal length, the trade-off emerges. The tight focused beam has a large conversion efficiency at the focal spot. Since the confocal length of such a beam is small, the beam spreads rapidly with propagation in the crystal. Therefore the conversion efficiency rapidly decreases with propagation. From a further consideration[70], the optimal focusing condition is given by

$$w_0 = \sqrt{\frac{d}{2.84k}}. \quad (2.25)$$

2.2.3 Second Harmonic Generation with Bow-Tie Cavity

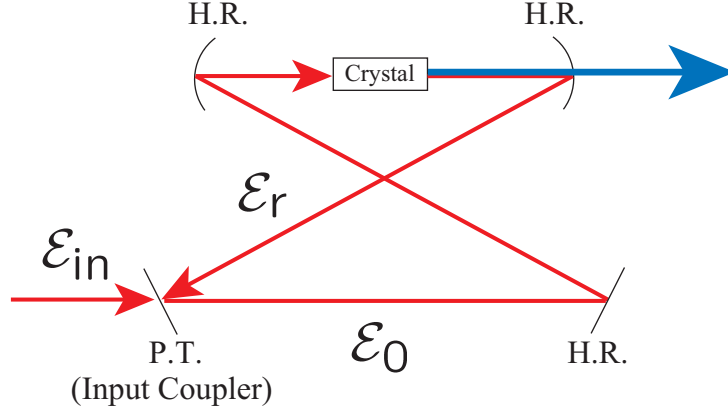


Figure 2.1: Electric field and a bow-tie cavity. H.R. and P.T. represent a high reflective mirror and a partially transmitted mirror, respectively. Those mirrors are anti-reflective coated to the second harmonic light.

Normally the nonlinear coefficient is small, so we need an intense fundamental light to generate appreciable second harmonic light. The cw laser light, however, is not intense enough, therefore we utilize the optical resonators or cavities to obtain relatively high conversion efficiency. The intensity inside the cavity (intracavity power) exceeds its value outside a mirror by $(1 - R)$, where R is the mirror reflectivity.

Let us consider the bow-tie cavity, described in Fig.2.1. The transmittance of the input coupler mirror is T and the other mirrors are highly reflective to the fundamental light. Every mirror is anti-reflection coated to second harmonic light, so that the generated second harmonic light escapes from the cavity. \mathcal{E}_{in} , \mathcal{E}_0 , and \mathcal{E}_r represents the electric field of the fundamental light input to the cavity, before the crystal, and after the crystal, respectively. Considering the phase shift by reflection, the following equation is obtained:

$$\mathcal{E}_0 = \sqrt{T}\mathcal{E}_{in} + i\sqrt{1-T}\mathcal{E}_r. \quad (2.26)$$

Considering the loss due to the conversion $\beta = \mathcal{I}^{(2\omega)}/\mathcal{I}^{(\omega)}$ and the loss L in the cavity other than the partial mirror and conversion loss, which is mainly caused by mirror imperfections, we obtain the following equation

$$\mathcal{E}_r = -i\sqrt{1-L}\sqrt{1-\beta}\mathcal{E}_0. \quad (2.27)$$

From the resonance condition of the cavity to the fundamental light, $-i$ was multiplied. From these two equations, the pump field of the crystal can be written as

$$\mathcal{E}_0 = \frac{\sqrt{T}\mathcal{E}_{in}}{1 - \sqrt{1-L}\sqrt{1-T}\sqrt{1-\beta}}. \quad (2.28)$$

Using the intensity of the second harmonic light $\mathcal{I}^{(2\omega)}$, the loss factor β can be written as

$$\beta = \sqrt{\eta \mathcal{I}^{(2\omega)}}. \quad (2.29)$$

The intensity of the second harmonic power is given by

$$\begin{aligned} \mathcal{I}^{(2\omega)} &= \eta \left(\frac{1}{2} c \varepsilon_0 |\mathcal{E}_0|^2 \right), \\ &= \eta \left[\frac{T \mathcal{I}_{\text{in}}}{(1 - \sqrt{1-T} \sqrt{1-L} \sqrt{1 - \sqrt{\eta \mathcal{I}^{(2\omega)}}})^2} \right]^2, \end{aligned} \quad (2.30)$$

$$\simeq \eta \left[\frac{4T \mathcal{I}_{\text{in}}}{2 - \sqrt{1-T}(2-L - \sqrt{\eta \mathcal{I}^{(2\omega)}})} \right]^2, \quad (2.31)$$

where $\mathcal{I}_{\text{in}} = \frac{1}{2} c \varepsilon_0 |\mathcal{E}_{\text{in}}|^2$ is the intensity of the input power to the cavity. We have assumed $L \ll 1$ and $\beta = \sqrt{\eta_{SHG} \mathcal{I}_{SHG}} \ll 1$. From (2.31), the optimal transmittance of input coupler for a given input power is given by

$$T = \frac{L}{2} + \sqrt{\frac{L^2}{4} + E_{NL} P_{\text{in}}}. \quad (2.32)$$

This result corresponds to an impedance-matching condition of the cavity, *i.e.*, zero reflection of the fundamental field by the input coupler .

2.3 Optical Parametric Amplification

The optical process that divides a highly oscillating field (pump field) $\omega_3 = \omega_1 + \omega_2$ into two lower oscillating fields ω_1 and ω_2 and amplifies the new fields, is called parametric amplification. In particular, when $\omega_1 = \omega_2 = \omega_3/2$, the process is referred to as degenerate parametric amplification. From the basic equation of the second nonlinear process (2.10)-(2.12), the degenerate parametric process can be described by

$$\frac{d\mathcal{E}_1}{dz} = -i\Omega_p e^{i\phi_3} \mathcal{E}_1^*, \quad (2.33)$$

$$\Omega_p = \frac{\omega_1}{2} \sqrt{\frac{\mu}{\varepsilon}} \varepsilon_0 \chi^{(2)} |\mathcal{E}_3|, \quad (2.34)$$

where ϕ_3 represents the phase of the pump field. The phase matching condition has been assumed to be satisfied. The solution of (2.33) is given by

$$\mathcal{E}_1(z) = \mathcal{E}_1(0) \cosh \Omega_p z - i e^{i\phi_3} \mathcal{E}_1^*(0) \sinh \Omega_p z. \quad (2.35)$$

The pump light was assumed to be intense and constant through the interaction region. Normally the nonlinear coefficient is small, and we place the crystal in a cavity resonant on the signal field. Let us consider the parametric process in a bow-tie cavity, whose configuration is the same as in the section 2.2.3.

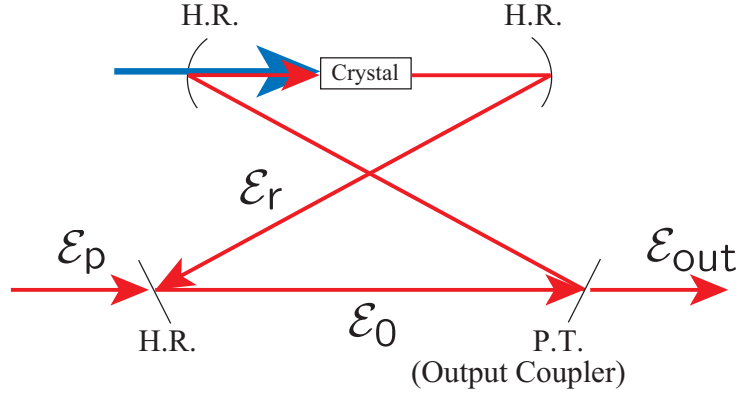


Figure 2.2: Electric field and a bow-tie cavity for degenerate parametric process. The crystal is pumped by the second harmonics generated by a doubler. The probe beam leaks into the cavity through the high reflective mirror.

Degenerate Parametric Process with Bow-Tie Cavity

A weak seed light is injected into the cavity through one of the high reflective mirrors (2.2). The slowly varying amplitudes are defined as follows:

- \mathcal{E}_0 : amplitude before the partially reflective mirror
- \mathcal{E}_r : amplitude after the nonlinear crystal
- \mathcal{E}_p : amplitude injecting into the cavity
- \mathcal{E}_{out} : amplitude output from the cavity

Every field is assumed not to depend on the time. Considering the phase shift by reflection, \mathcal{E}_0 can be written as

$$\mathcal{E}_0 = i\sqrt{1-T'}\mathcal{E}_r + \sqrt{T'}\mathcal{E}_p, \quad (2.36)$$

where T' is the transmission of the high reflective mirror. The length of the crystal d is assumed to be small, so the solution of the (2.33) can be approximately given by

$$\mathcal{E}_1 = -i\Omega_p e^{i\phi_3} d\mathcal{E}_1^*. \quad (2.37)$$

The field after the crystal can, therefore, be written as

$$\mathcal{E}_r = \sqrt{1-T}(\mathcal{E}_0 - i\Omega_p e^{i\phi_3} d\mathcal{E}_0^*). \quad (2.38)$$

Substituting (2.38) into (2.36), we obtain

$$\mathcal{E}_0 = i\sqrt{1-T'}\sqrt{1-T}(\mathcal{E}_0 - i\Omega_p e^{i\phi_3} d\mathcal{E}_0^*) + \sqrt{T'}\mathcal{E}_p. \quad (2.39)$$

In the following discussion, T , T' and $\Omega_p d\mathcal{E}_0$ are assumed to be small, and their second order terms are neglected. With these assumptions, (2.39) can be transformed into

$$-\left(\frac{T+T'}{2}\right)\mathcal{E}_0 - i\Omega_p e^{i\phi_3} d\mathcal{E}_0^* + \sqrt{T'}\mathcal{E}_p = 0. \quad (2.40)$$

The complex conjugated equation can be written as

$$-\left(\frac{T+T'}{2}\right)\mathcal{E}_0^* + i\Omega_p e^{-i\phi_3} d\mathcal{E}_0 + \sqrt{T'}\mathcal{E}_p^* = 0. \quad (2.41)$$

The solution of these equations is given by

$$\mathcal{E}_0 = \sqrt{T'} \frac{\frac{T+T'}{2}\mathcal{E}_p - i\Omega_p d e^{i\phi_3} \mathcal{E}_p^*}{\left(\frac{T+T'}{2}\right)^2 - (\Omega_p d)^2}. \quad (2.42)$$

The optical parametric oscillation occurs when the threshold parameter

$$x = \frac{\Omega_p d}{(T+T')/2} = 1. \quad (2.43)$$

The normalized output intensity from the cavity varies with the phase of probe light or pump light

$$G(\theta) = \frac{I(\phi_p)}{I_0} = \frac{1+x^2+2x\sin(\phi_3-2\phi_p)}{(1-x^2)^2}, \quad (2.44)$$

where I_0 is the output intensity without pump light, and ϕ_p is the phase of the probe lights. This can be understood as the interference between the injected probe light and the generated new field whose phase depends on the phase of probe light or pump light. The maximal gain G_+ and attenuation G_- is given by

$$G_{\pm} = \frac{(1 \pm x)^2}{(1 - x^2)^2}. \quad (2.45)$$

If we treat the signal lights as quantized fields. The equation may be written as

$$\frac{d\hat{\mathcal{E}}_1}{dz} = -i\Omega_p e^{i\phi_3} \hat{\mathcal{E}}_1^\dagger, \quad (2.46)$$

and the solutions is

$$\hat{\mathcal{E}}_1(z) = \hat{\mathcal{E}}_1(0) \cosh \Omega_p z - i e^{i\phi_3} \hat{\mathcal{E}}_1^\dagger(0) \sinh \Omega_p z. \quad (2.47)$$

This result seems equivalent to (1.26). This indicates that this process can be utilized for the generation of a squeezed vacuum. In the following section, we discuss generation of a squeezed vacuum through the parametric process in the cavity.

2.3.1 Generation of Squeezed Vacuum by Sub-threshold Optical Parametric Oscillator

The parametric process also works for the vacuum field, and generates a squeezed vacuum. The squeezed vacuum is output from the partially reflective mirror (output coupler) when we inject the pump field into the cavity.

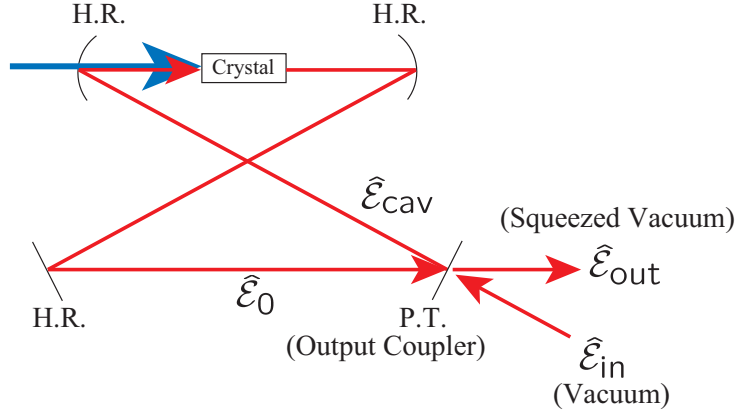


Figure 2.3: Electric field and a bow-tie cavity for degenerate parametric process. The crystal is pumped by the second harmonics generated by a doubler. No other beams are incident on the cavity.

In order to understand the generation process of a squeezed vacuum, we have to take into account the vacuum field incident on the cavity from the output coupler.

We derive the equation relating $\hat{\mathcal{E}}_{\text{in}}$ with $\hat{\mathcal{E}}_{\text{cav}}$ by considering that of classical amplitudes. Under the resonance condition, the buildup of the cavity field amplitude \mathcal{E}_{cav} is described by ,

$$\mathcal{E}_{\text{cav}}(t) = \sqrt{T}\mathcal{E}_{\text{in}}(t) + i\sqrt{R}\mathcal{E}_0(t), \quad (2.48)$$

$$\mathcal{E}_0(t) = -i(\mathcal{E}_{\text{cav}}(t - l/c) - i\Omega_p d\mathcal{E}_{\text{cav}}^*(t)), \quad (2.49)$$

where l is the length of the cavity. We expand the slowly varying amplitude $\mathcal{E}_{\text{cav}}(t - l/c)$ upto the first order,

$$\mathcal{E}_{\text{cav}}(t - l/c) = \mathcal{E}_{\text{cav}}(t) - \frac{l}{c} \frac{d\mathcal{E}_{\text{cav}}}{dt}. \quad (2.50)$$

Substituting (2.48) into (2.50), we obtain

$$\frac{d\mathcal{E}_{\text{cav}}}{dt} = -\frac{\gamma}{2}\mathcal{E}_{\text{cav}} - i\Omega_p d \frac{c}{l} \mathcal{E}_{\text{cav}}^* + \frac{c\sqrt{T}}{l}\mathcal{E}_{\text{in}}, \quad (2.51)$$

where we left the small term up to the second order. $\gamma = cT/l$ denotes the decay rate of the cavity. The corresponding equation in the quantum theory may be given by

$$\frac{d\hat{\mathcal{E}}_{\text{cav}}}{dt} = -\frac{\gamma}{2}\hat{\mathcal{E}}_{\text{cav}} - i\Omega_p e^{i\phi_3} d \frac{c}{l} \hat{\mathcal{E}}_{\text{cav}}^* + \frac{c\sqrt{T}}{l}\hat{\mathcal{E}}_{\text{in}}. \quad (2.52)$$

The slowly varying amplitude operators $\hat{\mathcal{E}}_{\text{cav}}$ and $\hat{\mathcal{E}}_{\text{in}}$ can be given by

$$\hat{\mathcal{E}}_{\text{cav}} = \sqrt{\frac{2\hbar\omega_0}{\epsilon_0 l A}} \hat{a}(t), \quad (2.53)$$

$$\hat{\mathcal{E}}_{\text{in}} = \sqrt{\frac{2\hbar\omega_0}{\epsilon_0 c A}} \sqrt{\frac{1}{2\pi}} \int \hat{b}_{\text{in}}(\omega) e^{-i(\omega - \omega_0)t} d\omega. \quad (2.54)$$

where $\hat{a}(t)$ and $\hat{b}_{\text{in}}(\omega)$ represent the intracavity field and the Fourier transform of the leaking field into the cavity, respectively. ω_0 is the carrier frequency of the field in our interest. The normalization adopted is appropriate for a one-dimensional traveling field, with a transverse quantization area A .

$$\frac{d\hat{a}(t)}{dt} = -\frac{\gamma}{2}\hat{a}(t) - i\Omega_p e^{i\phi_3} d \frac{c}{l} \hat{a}^\dagger(t) + \hat{F}(t), \quad (2.55)$$

$$\hat{F}(t) = \sqrt{\gamma} \sqrt{\frac{1}{2\pi}} \int \hat{b}_{\text{in}} e^{-i(\omega - \omega_0)t} d\omega. \quad (2.56)$$

It should be noted that \hat{F} has the properties of the Langevin operator :

$$\langle \hat{F}(t) \rangle = 0, \quad (2.57)$$

$$\langle \hat{F}^\dagger(t) \hat{F}(t') \rangle = 0, \quad (2.58)$$

$$\langle \hat{F}(t) \hat{F}^\dagger(t') \rangle = \frac{\gamma}{2\pi} \delta(t - t'). \quad (2.59)$$

(2.55) can be rewritten in the matrix form with its Hermite conjugate equation,

$$\dot{\mathcal{A}} = -\mathcal{M}\mathcal{A} + \mathcal{F}, \quad (2.60)$$

$$\mathcal{A} = \begin{bmatrix} \hat{a}(t) \\ \hat{a}^\dagger(t) \end{bmatrix}, \quad (2.61)$$

$$\mathcal{M} = \begin{bmatrix} \frac{\gamma}{2} & i\Omega_p e^{i\phi_3} d \frac{c}{l} \\ -i\Omega_p e^{-i\phi_3} d \frac{c}{l} & \frac{\gamma}{2} \end{bmatrix}, \quad (2.62)$$

$$\mathcal{F} = \begin{bmatrix} \hat{F}(t) \\ \hat{F}^\dagger(t) \end{bmatrix}. \quad (2.63)$$

A formal solution of (2.60) is given by

$$\mathcal{A}(t) = e^{-\mathcal{M}t} \mathcal{A}(0) + \int_0^t e^{-\mathcal{M}(t-t')} \mathcal{F}(t') dt'. \quad (2.64)$$

We assume the steady state, so that the first term, proportional to the initial field inside the cavity, is gone. Then the explicit form of the annihilation operator inside the cavity can be described by

$$\hat{a}(t) = \int_0^t e^{-\frac{\gamma}{2}(t-t')} \left[\cosh \Omega_p d \frac{c}{l} (t-t') \hat{F}(t') + i e^{-i\phi_3} \sinh \Omega_p d \frac{c}{l} (t-t') \hat{F}^\dagger(t') \right] dt'. \quad (2.65)$$

Substituting (2.56) and integrating over time, we obtain,

$$\begin{aligned} \hat{a}(t) = & \sqrt{\frac{\gamma}{2\pi}} \int d\omega \\ & \left[\frac{e^{-i(\omega - \omega_0)t} \left(\frac{\gamma}{2} - i(\omega - \omega_0) \right) + e^{-\frac{\gamma}{2}t} \left(\left(\frac{\gamma}{2} - i(\omega - \omega_0) \right) \cosh \Omega_p d \frac{c}{l} t + i(\Omega_p d \frac{c}{l}) \sinh \Omega_p d \frac{c}{l} t \right)}{\left(\frac{\gamma}{2} - i(\omega - \omega_0) \right)^2 - (\Omega_p d \frac{c}{l})^2} \hat{b}_{\text{in}}(\omega) \right. \\ & \left. - i e^{-i\phi_3} \frac{(\Omega_p d \frac{c}{l}) e^{-i(\omega_0 - \omega)t} + e^{-\frac{\gamma}{2}t} \left((\Omega_p d \frac{c}{l}) \cosh \Omega_p d \frac{c}{l} t + i \left(\frac{\gamma}{2} - i(\omega_0 - \omega) \right) \sinh \Omega_p d \frac{c}{l} t \right)}{\left(\frac{\gamma}{2} - i(\omega_0 - \omega) \right)^2 - (\Omega_p d \frac{c}{l})^2} \hat{b}_{\text{in}}^\dagger(\omega) \right]. \end{aligned} \quad (2.66)$$

Taking the long time limit, the decaying exponentials can be dropped.

$$\begin{aligned}\hat{a}(t) &= \sqrt{\frac{\gamma}{2\pi}} \int d\omega \\ &\frac{e^{-i(\omega-\omega_0)t}(\frac{\gamma}{2} - i(\omega - \omega_0))}{(\frac{\gamma}{2} - i(\omega - \omega_0))^2 - (\Omega_p d_l^c)^2} \hat{b}_{\text{in}}(\omega) \\ &- ie^{-i\phi} \frac{(\Omega_p d_l^c) e^{-i(\omega_0-\omega)t}}{(\frac{\gamma}{2} - i(\omega_0 - \omega))^2 - (\Omega_p d_l^c)^2} \hat{b}_{\text{in}}^\dagger(\omega).\end{aligned}\quad (2.67)$$

Changing the variable of integration in the second term of integral, from ω to $2\omega_0 - \omega$, we obtain,

$$\hat{a}(t) = \sqrt{\frac{\gamma}{2\pi}} \int d\omega \frac{(\frac{\gamma}{2} - i(\omega - \omega_0)) \hat{b}_{\text{in}}(\omega) - ie^{-i\phi} (\Omega_p d_l^c) \hat{b}_{\text{in}}^\dagger(2\omega_0 - \omega)}{(\frac{\gamma}{2} - i(\omega - \omega_0))^2 - (\Omega_p d_l^c)^2} e^{-i(\omega-\omega_0)t}.\quad (2.68)$$

The leaking field from the cavity can be written as

$$\begin{aligned}\mathcal{E}_{\text{out}}(t) &= i\sqrt{R}\mathcal{E}_{\text{in}}(t) + \sqrt{T}\mathcal{E}_0(t) \\ &\simeq i\sqrt{R}\mathcal{E}_{\text{in}}(t) - i\sqrt{T}\mathcal{E}_{\text{cav}}(t).\end{aligned}\quad (2.69)$$

The quantum mechanical equation of (2.69) may be written as

$$\hat{b}_{\text{out}}(t) = i\sqrt{R}\hat{b}_{\text{in}}(t) - i\sqrt{\gamma}\hat{a}(t).\quad (2.70)$$

By the Fourier transformation, $\hat{b}_{\text{out}}(t)$ and $\hat{b}_{\text{in}}(t)$ can be written as

$$\hat{b}_{\text{out}}(t) = \sqrt{\frac{1}{2\pi}} \int \hat{b}_{\text{out}}(\omega) e^{-i(\omega-\omega_0)t} d\omega,\quad (2.71)$$

$$\hat{b}_{\text{in}}(t) = \sqrt{\frac{1}{2\pi}} \int \hat{b}_{\text{in}}(\omega) e^{-i(\omega-\omega_0)t} d\omega.\quad (2.72)$$

From (2.68), (2.71), and (2.72), the Fourier components of the output field can be given by

$$\hat{b}_{\text{out}}(\omega_0 + \delta) = i\sqrt{R}\hat{b}_{\text{in}}(\omega_0 + \delta) - i\gamma \frac{(\frac{\gamma}{2} - i\delta)\hat{b}_{\text{in}}(\omega_0 + \delta) - ie^{-i\phi_3}(\Omega_p d_l^c)\hat{b}_{\text{in}}^\dagger(\omega_0 - \delta)}{(\frac{\gamma}{2} - i\delta)^2 - (\Omega_p d_l^c)^2},\quad (2.73)$$

where $\delta = \omega - \omega_0$. As we discussed in the previous chapter, what we measure with a conventional homodyne method is the square of the two-mode quadrature and is described by

$$\hat{\mathcal{S}}_{\text{mono}}(\delta, \theta) = 4\hat{X}^2(\delta, \theta),\quad (2.74)$$

where $\hat{X}(\delta, \theta)$ represents two-mode quadrature operator, which is defined by (1.37). Considering that the input state is in a vacuum state, the normalized quadrature noise of the output field is given by

$$\left\langle \hat{\mathcal{S}}_{\text{mono}}(\delta, \theta) \right\rangle = 1 + 2\gamma\Omega_p d_l^c \left[\frac{\cos^2(\theta + \frac{\phi_3}{2})}{(\frac{\gamma}{2} - \Omega_p d_l^c)^2 + \delta^2} - \frac{\sin^2(\theta + \frac{\phi_3}{2})}{(\frac{\gamma}{2} + \Omega_p d_l^c)^2 + \delta^2} \right].\quad (2.75)$$

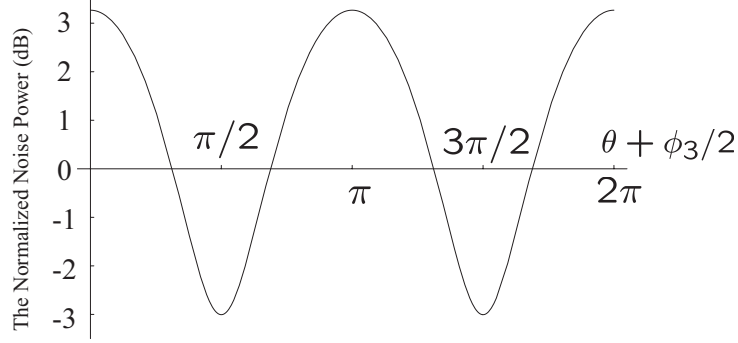


Figure 2.4: The dependence of the normalized noise power (dB) on the direction of the quadrature with $\rho=0.9$, $x=0.2$, $\gamma=50$, $\delta=1$. When $\theta + \phi_3/2 = 0$, the quadrature noise are amplified and when $\theta + \phi_3/2 = \pi/2$, the quadrature noise are suppressed.

Using a threshold parameter with $T' = 0$, we can rewrite the equation as

$$\langle \hat{\mathcal{S}}_{\text{mono}}(\delta, \theta) \rangle = 1 + 4x \left[\frac{\cos^2(\theta + \frac{\phi_3}{2})}{(1-x)^2 + (\frac{2\delta}{\gamma})^2} - \frac{\sin^2(\theta + \frac{\phi_3}{2})}{(1+x)^2 + (\frac{2\delta}{\gamma})^2} \right]. \quad (2.76)$$

This formula can be easily expanded to a formula including the loss in the cavity. The expression of the squeezing from the OPO with loss L can be given by

$$\langle \hat{\mathcal{S}}_{\text{mono}}(\delta, \theta) \rangle = 1 + 4\rho x \left[\frac{\cos^2(\theta + \frac{\phi_3}{2})}{(1-x)^2 + (\frac{2\delta}{\gamma})^2} - \frac{\sin^2(\theta + \frac{\phi_3}{2})}{(1+x)^2 + (\frac{2\delta}{\gamma})^2} \right], \quad (2.77)$$

where $\rho = \frac{T}{T+L}$ is referred to as the escape efficiency.

The dependence of (2.77) on $\theta + \phi_3/2$ is shown in Fig. 2.4 with $\rho=0.9$, $x=0.2$, $\gamma=50$, $\delta=1$. It is found that the noise of the quadrature $X(\delta, \pi/2 - \phi_3/2)$ is reduced and that of $X(\delta, -\phi_3/2)$ is amplified.

When the detection efficiency of the homodyne detector is ζ , (2.77) can be transformed into

$$\langle \hat{\mathcal{S}}_{\text{mono}}(\delta, \theta) \rangle = 1 + 4\zeta\rho x \left[\frac{\cos^2(\theta + \frac{\phi_3}{2})}{(1-x)^2 + (\frac{2\delta}{\gamma})^2} - \frac{\sin^2(\theta + \frac{\phi_3}{2})}{(1+x)^2 + (\frac{2\delta}{\gamma})^2} \right]. \quad (2.78)$$

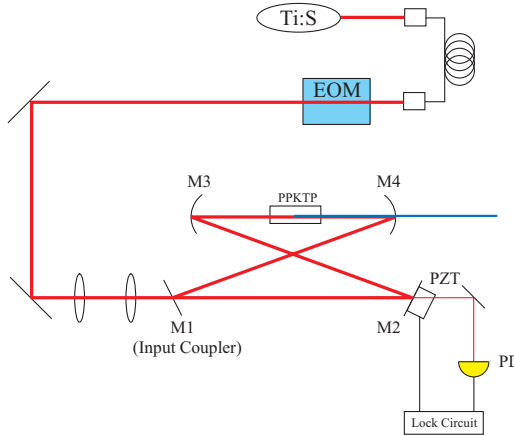


Figure 2.5: Experimental setup. Ti:S, Ti-sapphire laser; EOM, electro-optic modulator, made of lithium niobate; PZT, monolayer piezoelectric transducer, made of lead zirconium titanate; PD, Photodetector; M1, partially reflective ($R=0.9$) flat mirror; M2, highly reflective ($R>0.9999$) flat mirror; M3, highly reflective ($R>0.9999$) curved mirror; M4, highly reflective ($R>0.9999$) curved mirror with anti-reflective coat to 397.5nm (second harmonic light). The radii of the curved mirrors are 100mm, each.

2.4 Experiment on Generation of Squeezed Vacuum with PPKTP crystals

2.4.1 Second Harmonic Generation with PPKTP crystal

The experimental setup for a frequency doubler is shown in Fig. 2.5. A continuous-wave Ti:sapphire laser (Coherent, MBR 110) at 795nm was employed in this experiment. The beam from the Ti:sapphire laser was phase modulated by an electro-optic modulator (EOM). The modulation frequency was 3.0 MHz. This modulation was utilized to lock a bow-tie cavity using the FM side band method. The detail of the locking method is described in [71]. Two lenses are used to couple the beam to a bow-tie cavity consisting of two spherical mirrors (radius of curvature of 100mm) and two flat mirrors. One of the flat mirrors (PT1) had a reflectivity of 90% at 795nm, and was used as the input coupler while the other mirrors (one flat mirror and two curved mirrors) were high reflectivity coated (99.99%). All the mirrors had reflectivities of less than 5% at 397.5 nm. The round trip cavity length was $l = 520$ mm, and the beam waist radius inside the crystal was $26 \mu\text{m}^1$. The configuration of the SHG cavity is shown in Fig. 2.6

A 1 mm wide \times 1mm thick \times 10 mm long periodically poled KTiOPO_4 crystal, which was fabricated so that quasi phase matching is obtained at room temperature, was used for second harmonic generation. Blocking the

¹The optimal radius is calculated as $16 \mu\text{m}$. The power of the second harmonic light could not be stabilized with such a tight focused beam.

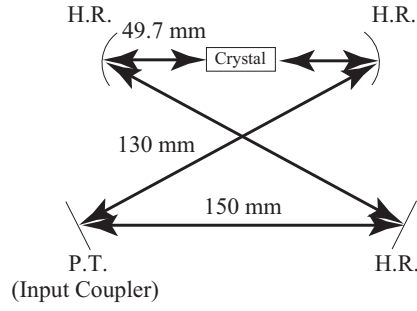


Figure 2.6: The configuration of the SHG cavity.

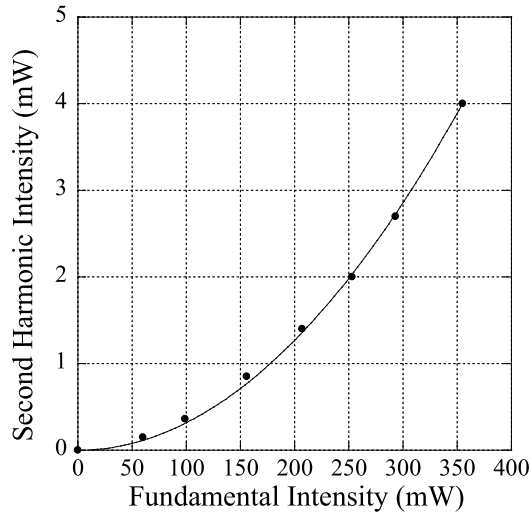


Figure 2.7: The second harmonic intensity dependence on the fundamental intensity. The wave length of the fundamental light was 796.525nm. The temperature was actively stabilized at 50°C . The beam waist was 26 μm . The solid line was a fitting line by (2.16).

optical pass in the cavity, we measured the dependence of the intensity of second harmonic light to that of fundamental light (Fig. 2.7).

By fitting the experimental data with (2.16), the conversion efficiency of the crystal was found to be 0.032 W^{-1} . The loss of the cavity varies from 1% to 10% depending on the beam position in the crystal. We believe that the loss is caused by the gray tracks[72, 73, 74, 75]. Since the maximum input (fundamental) power was approximately 400 mW, the optimal transmittance of the input coupler ranged from 1% to 12% depending on the input power. We selected $T = 0.1$.

Figure 2.8 shows the dependence of the second harmonic light from the cavity on the input fundamental power. We obtained 104 mW of second harmonic light for 284 mW of the incident fundamental light. We observed instability of the blue output power when the fundamental light exceeded approximately 300 mW. When we injected, for example, 391 mW of the fundamental light, the intensity of second harmonic light (115 mW) was

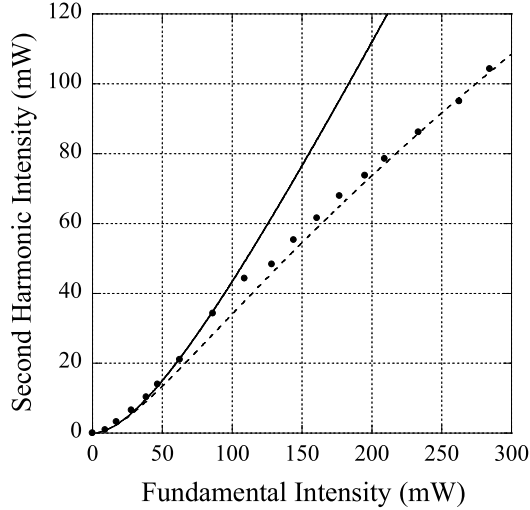


Figure 2.8: The dependence of the intensity of the second harmonic light from the bow-tie cavity on the intensity of the fundamental light. The solid line is obtained from (2.30) with $L = 0.05$. The broken line is obtained, assuming the loss proportional to the intensity of the second harmonic light. The loss coefficient α is 0.5.

not stable and decreased to 106 mW within a minute. The solid line in Fig. 2.8 is obtained from (2.30) with $L = 0.05$. The discrepancy from the experimental data increases with the intensity of the second harmonic light. For KNbO_3 crystal it is well-known that the second harmonic light induces the additional loss for the fundamental light which is referred to as Blue Light Induced Infra Red Absorption (BLIIRA)[77]. Although there are no such reports for the PPKTP crystal, we add the additional loss proportional to the second harmonic light to (2.30):

$$\mathcal{I} = \eta \left[\frac{T\mathcal{I}_{\text{in}}}{1 - \sqrt{1 - T}\sqrt{1 - \alpha\mathcal{I}}\sqrt{1 - L}\sqrt{1 - \sqrt{\eta\mathcal{I}}}} \right]^2. \quad (2.79)$$

The broken line is well in agreement with the experimental data, though the coefficient $\alpha = 0.5$ is substantially larger than that of KNbO_3 crystal. This point has to be further investigated.

2.4.2 Optical Parametric Oscillation with PPKTP Crystal

The experimental setup for an optical parametric oscillator is shown in Fig. 2.9. The OPO cavity also has a bow-tie ring configuration with two spherical mirrors (radius of curvature of 50mm) and two flat mirrors. The beam waist radius inside a 10 mm long PPKTP crystal was $21 \mu\text{m}^2$. The cavity length

²Because of a lack of the available space, we had to construct a cavity which has a different size from the frequency doubler.

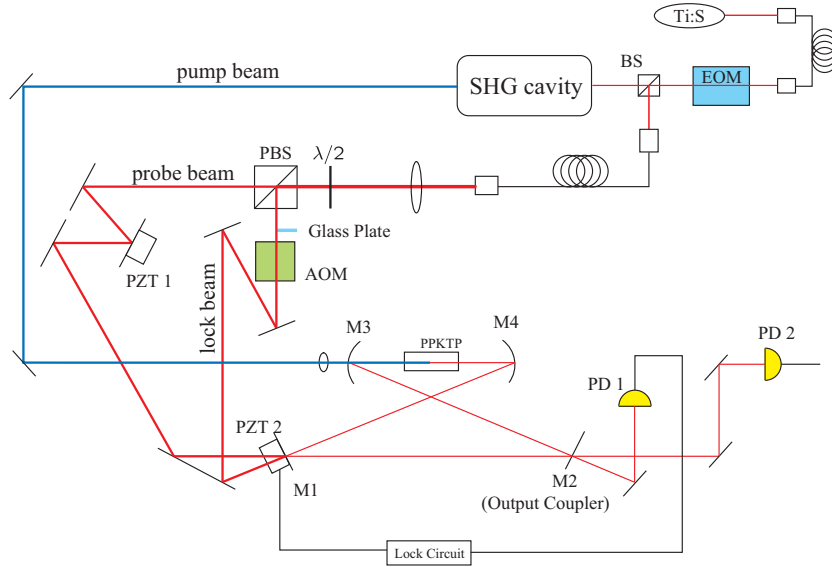


Figure 2.9: Experimental setup. AOM; acousto-optic modulator; M1, highly reflective ($R > 0.9999$) flat mirror; M2, partially reflective ($R = 0.9$) flat mirror; M3, highly reflective ($R > 0.9999$) curved mirror with anti-reflective coat to 397.5nm (second harmonic light); M4, highly reflective ($R > 0.9999$) curved mirror. The radii of the curved mirrors are 50mm.

was $l = 627$ mm. The cavity configuration is shown in Fig. 2.10. One of the flat mirrors is used as an output coupler, whose reflectivity is 90% at 795nm. We tapped the fundamental light from the SHG system. The tapped light is used for the probe light and the light to lock the cavity length (lock beam).

The OPO cavity length was locked so that the frequency of the fundamental light (795nm) was resonant. Both of the probe beam and the lock beam was injected into the cavity through one of high reflective mirrors (M1) but they counter-propagate each other in the cavity. The leaking field of the lock beam was detected by PD1 and the error signal for locking the cavity length was extracted using the FM sideband method. Due to the imperfection of the AR coating of the crystal, part of the lock beam co-propagated to the probe beam. This co-propagating beam would interfere with the generated

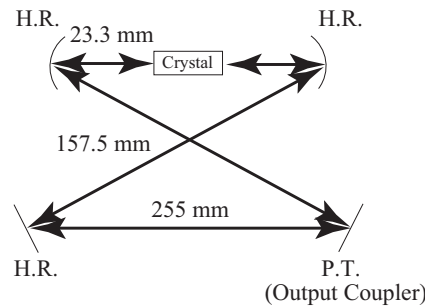


Figure 2.10: The configuration of the OPO cavity.

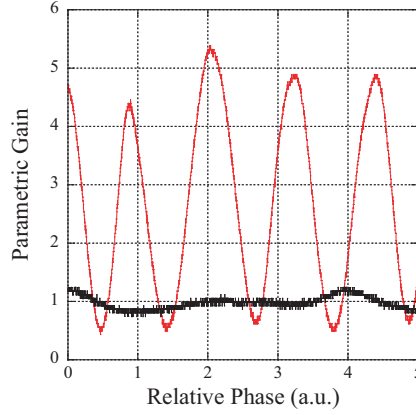


Figure 2.11: Red (Black) curve shows the output intensity from the cavity with (without) the pump beam of 61mW. The relative phase was varied by using PZT1.

squeezed vacuum in the next experiment. In order to avoid the interference, the frequency shift of 120 MHz was provided to the lock beam by an acousto-optic modulator (AOM) and is chosen equal to the transverse-mode spacing of the cavity. A thin glass plate provided π -phase shift to the half of the lock beam and converted the mode from TEM_{00} to TEM_{10} . When the cavity is resonant to the frequency-shifted lock beam in TEM_{10} mode, the frequency unshifted probe beam or generated squeezed vacuum in TEM_{00} is likewise on resonant[76].

The transmitted probe beam from the output coupler was detected by a photodetector (PD2). The phase of the incident probe beam was modulated by the PZT1.

Figure 2.11 shows a typical signal from PD1. The black curve in Fig 2.11 shows the transmittance power of the probe beam without the pump beam. The fluctuation was due to the instability of the lock system. When 61mW of the pump beam was incident on the cavity, due to the parametric process, the output intensity of the probe light varied with the relative phase between the pump light and the probe light (red curve in Fig. 2.11). The parametric gain $G_+ = 4.97 \pm 0.56$ and attenuation $G_- = 0.59 \pm 0.07$ were observed. Gain is normalized by the average of the probe signal without the pump light.³ From G_+ and (2.45), the pump parameter for 61mW pump beam, $x = 0.55$ is derived.

2.4.3 Generation of Squeezed Vacuum with PPKTP Crystal

The whole experimental setup for generation of a squeezed vacuum is shown in Fig. 2.12. To generate a squeezed vacuum, the probe beam was blocked.

³As we discussed before, the extra loss for the red light could be induced by the blue light. Since the reference power varied with the loss, we should have measured the reference with the control light when the crystal was far from the phase matching temperature.

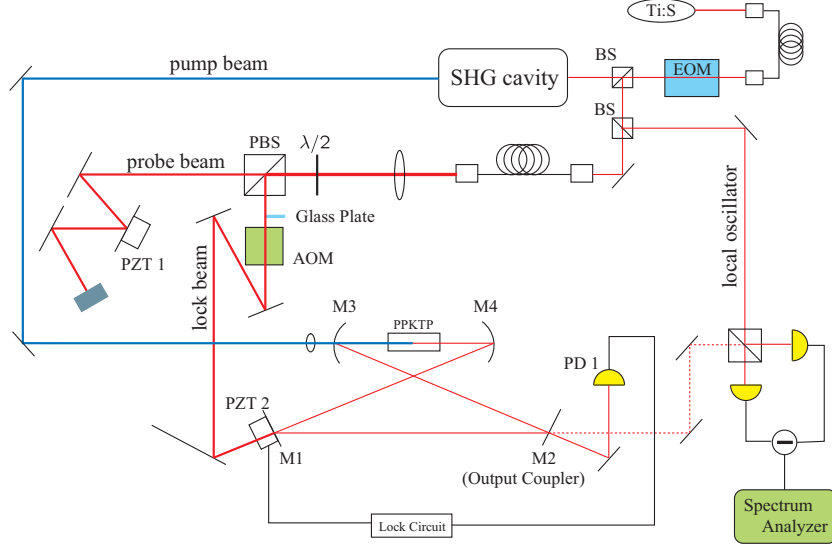


Figure 2.12: Experimental setup for generation of squeezed vacuum.

The generated squeezed vacuum was combined with a local oscillator at a half-beam splitter (HBS) and detected by a balanced homodyne detector (HD). The HD consisted of two photodiodes (Hamamatsu Photonics, S-3590 with antireflection coating for 860nm) that had a quantum efficiency of 99%. The output of the HD was measured at the sideband component of 1MHz using a spectrum analyzer. The circuit noise level of the homodyne detector was 14.0 dB below the shot noise level. The visibility between the local oscillator and the OPA output was 97%. Figure 2.13 shows the measured quantum noise levels at a pump power of 61 mW as the local oscillator phase was scanned. The noise level was measured with a spectrum analyzer in zero-span mode at 1 MHz, with a resolution bandwidth of 100 kHz and a video band width of 30 Hz. The squeezing level of $-2.75\text{dB} \pm 0.14\text{dB}$ and the antisqueezing level of $+7.00 \pm 0.13$ dB were observed, where the standard deviation was estimated from a fitting based on (2.78).

From the experimental results shown in the previous section, the pump parameter $x = 0.55$ was obtained for 61mW of the pump beam. To calculate the theoretical prediction from (2.78), the other experimental parameters in our OPO cavity are as follows:

- Transmission of the output coupler T : 0.1
- The intracavity loss L : 0.0173
- The escape efficiency $\rho = \frac{T}{T+L}$: 0.85
- The length of the cavity l : 600mm
- The decay rate of the cavity $\gamma = \frac{c(T+L)}{l}$: 72 MHz
- The visibility between the squeezed vacuum and the local oscillator ξ : 0.91

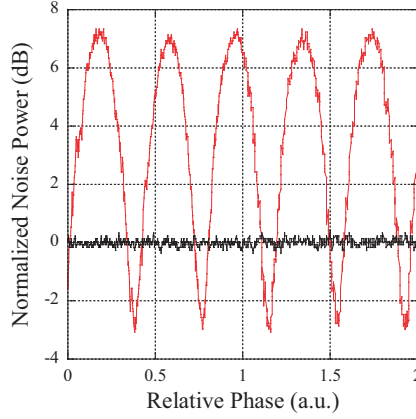


Figure 2.13: Measured quantum noise levels. (A) The settings of the spectrum analyzer were zero-span mode at 1MHz, resolution bandwidth=100kHz, and video bandwidth=30Hz.

From these values, the theoretical predictions of squeezing and antisqueezing levels are -4.4 dB and $+8.9$ dB, respectively. These theoretical values become -4.1 dB and $+8.7$ dB when the effect of the circuit noise is in the consideration. As Fig. 2.11 shown, our OPO cavity was not so stable, therefore it is hard to obtain the reliable gain parameter. We believe that this fluctuation causes the discrepancy between the experiment and the theoretical prediction. We will discuss the stability condition of the cavity in the next section.

2.5 Discussions

2.5.1 The Stability of Cavity

First we introduce a parameter, referred as to visibility, which evaluates the spatial mode overlapping of beam 1 with beam 2. Consider electric beams ($i = 1, 2$) are given by

$$\mathcal{E}_i(x, y, z) = \mathcal{E}_0 \sqrt{\frac{iz_{0i}^{(x)}}{q_i^{(x)}(z)}} \sqrt{\frac{iz_{0i}^{(y)}}{q_i^{(y)}(z)}} \exp\left(-\frac{ikx^2}{2q_i^{(x)}(z)} - \frac{iky^2}{2q_i^{(y)}(z)}\right), \quad (2.80)$$

where $q_i^{(x(y))}$ and $z_{0i}^{(x(y))}$ are a beam parameter and a confocal parameter of $x(y)$ direction of the beam i , respectively. The beam parameter is written as

$$q_i^{(x)}(z) = z - a_{0i}^{(x)} + iz_{0i}^{(x)}, \quad (2.81)$$

$$q_i^{(y)}(z) = z - a_{0i}^{(y)} + iz_{0i}^{(y)}, \quad (2.82)$$

where $a_{0i}^{(x)}$ represents the position of the beam spot.

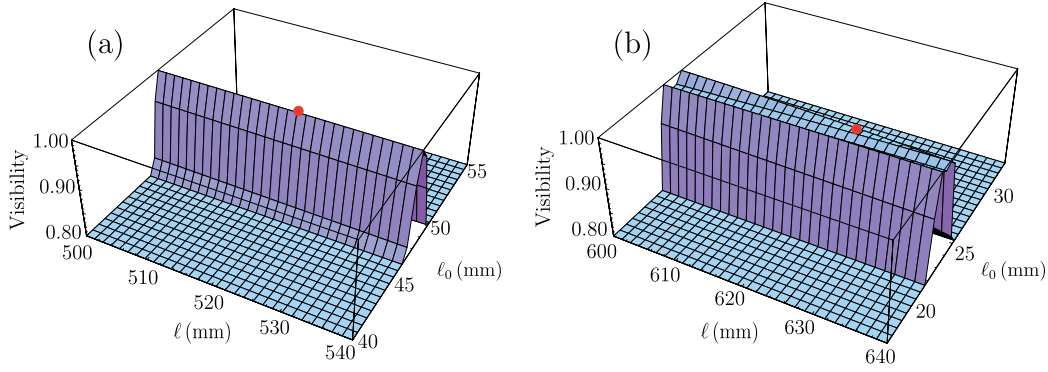


Figure 2.14: The dependence of the visibility on ℓ and ℓ_0 . Red circles indicate the cavity configuration. (a) SHG cavity. (b) OPO cavity.

The visibility between these beams is given by

$$\begin{aligned}
 V &= \frac{\iint \mathcal{E}_1 \mathcal{E}_2^* dx dy}{\iint |\mathcal{E}_1| dx dy \iint |\mathcal{E}_2| dx dy} & (2.83) \\
 &= \left(\frac{4z_{01}^{(x)} z_{02}^{(x)}}{(z_{01}^{(x)} + z_{02}^{(x)})^2 + (a_{01}^{(x)} - a_{02}^{(x)})^2} \times \frac{4z_{01}^{(y)} z_{02}^{(y)}}{(z_{01}^{(y)} + z_{02}^{(y)})^2 + (a_{01}^{(y)} - a_{02}^{(y)})^2} \right)^{1/4}. & (2.84)
 \end{aligned}$$

To design the cavity, we evaluate the visibility between the injecting beam and after its one round trip. The visibility should be 1 as close as possible. The stability of the cavity is determined by how much the visibility decreases with the displacement of mirrors. The dependence of the visibility on the cavity length l and on the distance from the curved mirror and the end facet of the crystal l_0 was calculated. Figure 2.14 shows the visibilities of the cavities (SHG and OPO) employed in this experiment. As Fig. 2.14 shows, both cavities are weak to the fluctuation of l_0 . We believe that one of the reasons of the instability of the cavities were caused by this weakness.

We also confirmed that the tight focused beam in the crystal also caused instability of the cavity, which may be due to a thermal lensing effect arising from the blue absorption [78].

Based on the discussion above, we reconstructed the cavity. The beam waist in the crystal was $60 \mu\text{m}$. The configuration and the visibility of the new cavity is shown in Fig. 2.15. Although the whole experiments presented following sections employed the cavities in this chapter, more than -3 dB squeezing obtained with the new cavity system.

2.6 Conclusion

We observed -2.75 ± 0.14 dB squeezing and $+7.00 \pm 0.13$ dB antisqueezing at 795 nm, which corresponds to the D_1 transition of Rb atoms. It should be possible to achieve a higher squeezing level by increasing the visibility of the

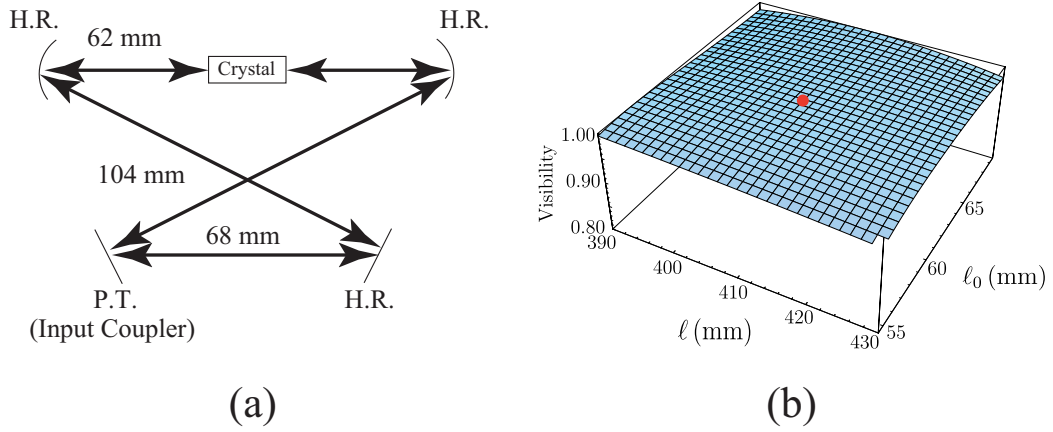


Figure 2.15: (a) A new cavity configuration. (b) The dependence of the visibility on ℓ and ℓ_0 . Red circle indicates the cavity configuration.

homodyne system and reducing the phase fluctuation by actively stabilizing the setup. While electromagnetically induced transparency was observed with the squeezed vacuum in our previous work, neither slow propagation nor storage could be realized due mainly to the low squeezing level. The squeezing level obtained in this setup was much higher than that previously obtained with periodically poled lithium niobate waveguides.

Part II

Electromagnetically Induced Transparency with Squeezed Vacuum

Chapter 3

Electromagnetically Induced Transparency with Squeezed Vacuum

An experiment on electromagnetically induced transparency with a squeezed vacuum is presented. A squeezed vacuum resonant on the ^{87}Rb D_1 line (probe light) was injected into an optically dense rubidium gas cell with a coherent light (control light). The output probe light maintained its quadrature squeezing within the transparency window caused by electromagnetically induced transparency. The result reported here is the first demonstration of EIT with a nonclassical probe light.

Before describing the details of the experiment, we give a full quantum description of EIT and derive the absorption coefficient and refractive index for a quantum probe field.

3.1 Quantum Description of Electromagnetically Induced Transparency

In order to consider electromagnetically induced transparency for a squeezed vacuum, which is one of the nonclassical lights¹, we have to treat a probe light as a quantized field while an intense control light is treated as a simple classical electromagnetic field. Such description also leads us to how to map the quantum information of the probe light onto the ground state spin coherence.

3.1.1 Optical Bloch Equation for Electromagnetically Induced Transparency

Consider a quasi-one-dimensional model, consisting of two co-propagating beams passing through an optically thick medium of length L consisting of

¹The nonclassical state is defined as the states which do not have a well-defined P-representation.

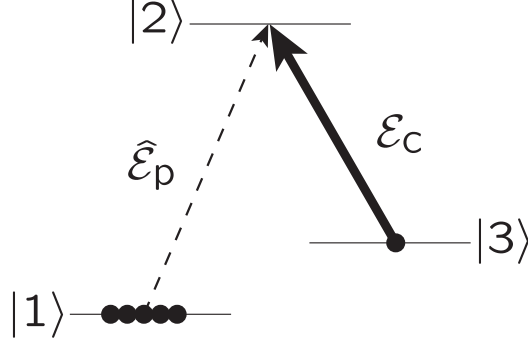


Figure 3.1: Three-level atomic system interacting with an intense coherent light (control light) and a quantized light (probe light).

three-level atoms shown in Fig. (3.1). The \mathbf{x} -polarized quantized probe field can be written as (in a Schrödinger picture)

$$\hat{\mathbf{E}}_p(z, t) = \frac{1}{2} \mathbf{x} \hat{\mathcal{E}}_p(z, t) e^{-ik_p z} + \text{c.c.} \quad (3.1)$$

Here slowly varying amplitude operator $\hat{\mathcal{E}}_p(z, t)$ is defined as

$$\hat{\mathcal{E}}_p(z, t) = \sqrt{\frac{2\hbar\omega_p}{\epsilon_0 V}} \hat{a}_p(z, t), \quad (3.2)$$

where \hat{a}_p and V are an annihilation operator and a quantization volume, which, for simplicity, is chosen to be equal to the interaction volume. The probe field couples one of the ground states $|1\rangle$ to the excited state $|2\rangle$. The other ground state $|3\rangle$ is coupled with the excited state $|2\rangle$ by a control light,

$$\mathbf{E}_c(z, t) = \frac{1}{2} \mathbf{y} \mathcal{E}_c(z, t) e^{i(\omega_c t - k_c z)} + \text{c.c.} \quad (3.3)$$

The Hamiltonian \mathcal{H} for this system is given by

$$\begin{aligned} \hat{\mathcal{H}} = & \sum_j [\hbar\omega_1 \hat{\sigma}_{11}^j + \hbar\omega_2 \hat{\sigma}_{22}^j + \hbar\omega_3 \hat{\sigma}_{33}^j + \frac{1}{2} \epsilon_0 V \hat{\mathcal{E}}_p^\dagger(z_j, t) \hat{\mathcal{E}}_p(z_j, t) \\ & - \wp_{12}^{(x)} \hat{E}_p(z_j, t) \hat{\sigma}_{12}^j - \wp_{32}^{(y)} E_c(z_j, t) \hat{\sigma}_{32}^j + \text{h.c.}], \end{aligned} \quad (3.4)$$

where $\wp_{ab}^{(i)}$ denotes an i direction component of the dipole matrix element between the states $|a\rangle$ and $|b\rangle$. z_j represents the position of the j th atoms. We defined the atomic flip operators at z_j as

$$\hat{\sigma}_{ab}^j \equiv |a\rangle_{jj} \langle b|. \quad (3.5)$$

In order to remove the time dependence of the Hamiltonian by a classical electromagnetic field (control light), we move to a new rotating frame by a transformation of

$$\hat{U}(t) = \exp[i \sum_j ((\omega_2 - \omega_p) \hat{\sigma}_{11}^j + \omega_2 \hat{\sigma}_{22}^j + (\omega_2 - \omega_c) \hat{\sigma}_{33}^j + \epsilon_0 \hat{\mathcal{E}}_p^\dagger(z_j, t) \hat{\mathcal{E}}_p(z_j, t)) t]. \quad (3.6)$$

The effective Hamiltonian is written as

$$\hat{\mathcal{H}}_{eff}/\hbar = \sum_j [\delta_p \hat{\sigma}_{11}^j + \delta_c \hat{\sigma}_{33}^j - g \hat{a}_p(z_j, t) \hat{\sigma}_{21} e^{-ik_p z_j} - \Omega_c \hat{\sigma}_{32} e^{-ik_c z_j} + \text{h.c.}], \quad (3.7)$$

where $g = \sqrt{\frac{\omega_p}{2\hbar\epsilon_0 V}} \wp_{21}$ and $\Omega_c = \frac{\wp_{32}\mathcal{E}_c}{2\hbar}$ are the coupling constant between an atom and the probe field and the Rabi frequency of the control field. We have made the rotating wave approximation. If the slowly varying quantum amplitude does not change in a length interval Δz , which contains $N_z \gg 1$ atoms, we can introduce continuum atomic variables,

$$\hat{\sigma}_{ii}(z) = \frac{1}{N_z} \sum_{z_j \in z \sim z + \Delta z} \hat{\sigma}_{ii}^j, \quad (3.8)$$

$$\hat{\sigma}_{21}(z) = \frac{1}{N_z} \sum_{z_j \in z \sim z + \Delta z} \hat{\sigma}_{21}^j e^{-ik_p z_j}, \quad (3.9)$$

$$\hat{\sigma}_{32}(z) = \frac{1}{N_z} \sum_{z_j \in z \sim z + \Delta z} \hat{\sigma}_{32}^j e^{-ik_c z_j}, \quad (3.10)$$

With these operators, we can rewrite the effective Hamiltonian as

$$\hat{\mathcal{H}}_{eff}/\hbar = \sum_z N_z [\delta_p \hat{\sigma}_{11}(z) + \delta_c \hat{\sigma}_{33}(z) - g \hat{a}_p(z, t) \hat{\sigma}_{21}(z) - \Omega_c \hat{\sigma}_{32}(z) + \text{h.c.}]. \quad (3.11)$$

Taking the continuum limit, the effective Hamiltonian can be written in terms of the locally-averaged atomic operators as

$$\hat{\mathcal{H}}_{eff}/\hbar = \frac{N}{L} \int dz [\delta_p \hat{\sigma}_{11}(z) + \delta_c \hat{\sigma}_{33}(z) - g \hat{a}_p(z, t) \hat{\sigma}_{21}(z) - \Omega_c \hat{\sigma}_{32}(z) + \text{h.c.}], \quad (3.12)$$

where N is the number of atoms in the interaction volume. The evolution of the Heisenberg operator can be given by the following equation:

$$\dot{\hat{\sigma}}_{11} = -ig(\hat{a}_p \hat{\sigma}_{21} - \hat{a}_p^\dagger \hat{\sigma}_{12}) + \gamma_1 \hat{\sigma}_{22} + \hat{F}_1, \quad (3.13)$$

$$\dot{\hat{\sigma}}_{22} = ig(\hat{a}_p \hat{\sigma}_{21} - \hat{a}_p^\dagger \hat{\sigma}_{12}) - i\Omega_c(\hat{\sigma}_{32} - \hat{\sigma}_{23}) - \gamma_2 \hat{\sigma}_{22} + \hat{F}_2, \quad (3.14)$$

$$\dot{\hat{\sigma}}_{33} = i\Omega_c(\hat{\sigma}_{32} - \hat{\sigma}_{23}) + \gamma_3 \hat{\sigma}_{22} + \hat{F}_3, \quad (3.15)$$

$$\dot{\hat{\sigma}}_{12} = -(-i\delta_p + \gamma_{12})\hat{\sigma}_{12} + ig\hat{a}_p(\hat{\sigma}_{11} - \hat{\sigma}_{22}) + i\Omega_c \hat{\sigma}_{13} + \hat{F}_{12}, \quad (3.16)$$

$$\dot{\hat{\sigma}}_{13} = -[i(\delta_c - \delta_p) + \gamma_{13}]\hat{\sigma}_{13} + i\Omega_c \hat{\sigma}_{12} - ig\hat{a}_p \hat{\sigma}_{23} + \hat{F}_{13}, \quad (3.17)$$

$$\dot{\hat{\sigma}}_{23} = -(i\delta_c + \gamma_{23})\hat{\sigma}_{23} - ig\hat{a}_p^\dagger \hat{\sigma}_{13} - i\Omega_c(\hat{\sigma}_{33} - \hat{\sigma}_{22}) + \hat{F}_{23}. \quad (3.18)$$

We have included the decays of atomic dipole: $\gamma_2 = \gamma_1 + \gamma_3$, γ_{12} , and γ_{23} and the decay of the spin coherence between the ground states γ_{13} with the associated Langevin noise operators, whose explicit form is not of interest here. This is a set of Heisenberg Langevin equations describing electromagnetically induced transparency.

3.1.2 Absorption Coefficient and Refractive Index by EIT

From the steady state solution of Heisenberg Langevin equations, the induced polarization of the probe transition can be derived. We assume that the control field is resonant on $|2\rangle$ - $|3\rangle$ transition, *i.e.*, $\delta_c = 0$ and the Rabi frequency of the control light is much larger than that of the probe light. Most of the atoms are, therefore, in a $|1\rangle$ state, *i.e.*, $\hat{\sigma}_{11} \approx 1, \hat{\sigma}_{22} \approx 0, \hat{\sigma}_{33} \approx 0$. Neglecting the second order term of \hat{a}_p , we obtain

$$\hat{\sigma}_{12} = \frac{ig\hat{a}_p}{\gamma_{12} - i\delta_p + \frac{\Omega_c^2}{\gamma_{13} - i\delta_p}}. \quad (3.19)$$

The induced polarization between $|1\rangle$ - $|2\rangle$ transition of the medium is given by the sum of the polarization of whole atoms

$$\hat{\mathcal{P}} = \rho \hat{U}(t) \left(\wp_{12}^{(x)} \hat{\sigma}_{12} + \wp_{21}^{(x)} \hat{\sigma}_{21} \right) \hat{U}^\dagger(t) \quad (3.20)$$

$$= i\varepsilon_0 \frac{g^2 N}{\omega_p} \frac{1}{\gamma_{12} - i\delta_p + \frac{\Omega_c^2}{\gamma_{13} - i\delta_p}} \hat{\mathcal{E}}_p(z, t) e^{i\omega t} + \text{c.c.}, \quad (3.21)$$

where ρ represents the atomic density. Therefore the susceptibility for the probe field of the medium can be written as

$$\chi = i \frac{2g^2 N}{\omega_p} \frac{1}{\gamma_{12} - i\delta_p + \frac{\Omega_c^2}{\gamma_{13} - i\delta_p}} \quad (3.22)$$

$$= i\rho \frac{\wp_{12}^2}{\hbar\varepsilon_0} \frac{1}{\gamma_{12} - i\delta_p + \frac{\Omega_c^2}{\gamma_{13} - i\delta_p}}. \quad (3.23)$$

The refractive index n and the absorption coefficient κ are given by

$$n = 1 + \text{Re}[\chi]/2, \quad (3.24)$$

$$\kappa = \text{Im}[\chi], \quad (3.25)$$

respectively.

As Figure 3.2 shows, the transparency region and the steep dispersion appears around the resonant frequency.

3.2 Experiment on Electromagnetically Induced Transparency with Squeezed Vacuum

We carried out the experiment on electromagnetically induced transparency with a squeezed vacuum. We generated a cw-squeezed vacuum resonant on the ^{87}Rb D₁ line (795 nm) by using two independent periodically poled

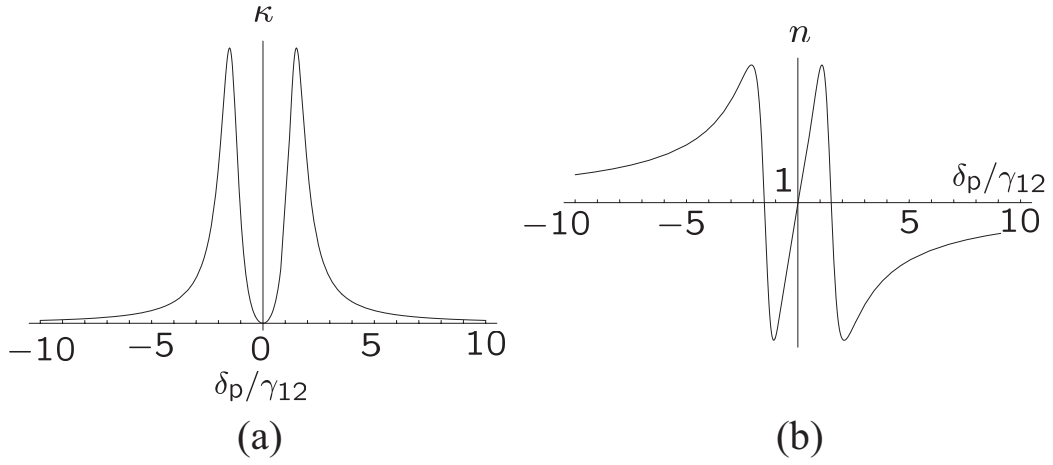


Figure 3.2: (a) Absorption coefficient and (b) refractive index (in arbitrary units) as a function of normalized detuning δ_p/γ_{12} .

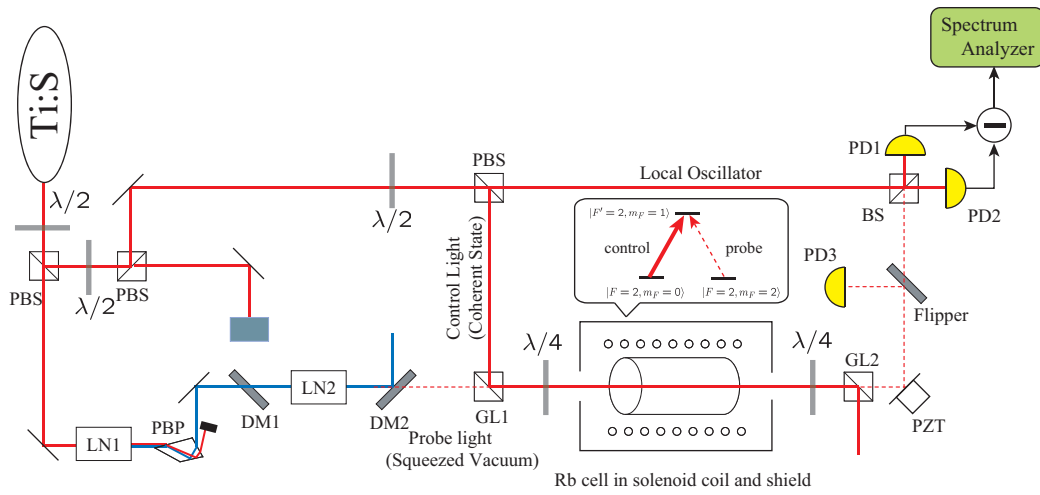


Figure 3.3: Schematic of the experiment setup. Ti:S, Ti:sapphire laser; PBS, polarizing beam splitter; LN, periodically poled MgO:LiNbO₃ waveguide; PBP, Pellin Broca prism; GL, Glan laser prism; BS, beam splitter; PZT, piezoelectric transducer; DM, dichroic mirror; PD, photodetector.

MgO:LiNbO₃ waveguides (LN1,2 in Fig. 3.3)[67]. We employed ridge waveguides, 5.0 μm wide \times 3.0 μm thick 8.5 mm long². They are fabricated so that quasi-phase-matching is obtained at room temperature. We coupled 269 mW of linearly polarized light from a Ti:sapphire laser into LN1 with 40% efficiency and generated 54 mW of second harmonic light. We separated the second harmonic light from the fundamental light by using a Pellin Broca prism and a dichroic mirror (DM1). Only the second harmonic light was injected into LN2 with 40% coupling efficiency, by which the squeezed vacuum was generated through the degenerate parametric process. The squeezed vacuum was separated from the second harmonic light by using DM2 and LN2. The power and spectral width of the squeezed vacuum were about 400 nW and 14 nm, respectively. In order to avoid any loss of the squeezed vacuum, we removed Glan laser prisms (GL1,2), $\lambda/4$ plates, and an ⁸⁷Rb glass cell and directly overlapped the squeezed vacuum with a local oscillator (5 mW) by a beam splitter. We measured quadrature noise of the squeezed vacuum by a balanced homodyne detector (PD1,2) and a spectrum analyzer. The experimental result is shown in Fig. 3.4. The observed squeezing level (-0.9 dB) and antisqueezing level ($+1.3$ dB) were independent of the spectrum analyzer center frequency up to 100 MHz because our system has no cavity, unlike the standard optical parametric oscillator. The bandwidth of the squeezing was limited by that of the preamplifier in the homodyne detector. As far as we know, this is the first time wideband squeezed vacuum has been generated in cw mode using MgO:LiNbO₃ waveguides.

We employed a pure ⁸⁷Rb vapor cell filled with 5 torr of ⁴He buffer gas as the EIT medium. The 10-cm-long, 30-mm-diameter cell was magnetically shielded by a threefold magnetic shield. The temperature was actively stabilized to 48°C, which corresponds to an atomic density of approximately 10^{11} cm⁻³. We employed the D₁ line $5^2\text{S}_{1/2}, F=2 \rightarrow 5^2\text{P}_{1/2}, F=2$ transition for control and probe fields. Two circularly polarized lights (control σ^+ and probe σ^-) coupled pairs of Zeeman sublevels of electronic ground states with magnetic quantum numbers differing by two, via the excited state.

Before the experiment with a squeezed vacuum, we performed EIT with a coherent probe light. We cut the second harmonic light incident on LN2 and injected a weak fundamental light into LN2 by removing the beam block. We employed the 2.3 mW/cm² output beam (diameter 1 mm) from LN2 as the probe light. (Because the input power was so weak, one can neglect the effect of second harmonic generation.) The control and probe lights polarized orthogonally to each other were overlapped using GL1 and were converted to σ^+ and σ^- circularly polarized lights by a $\lambda/4$ plate in front of the cell. The intensity of the input control light was 830 mW/cm². After passing through the cell, the probe light was separated from the control light by using a $\lambda/4$ plate and GL2. A flipper and a photodetector (PD3) were used to monitor the transmitted intensity of the probe light. When a homogeneous magnetic field is applied to the cell along the light axis using a

²Using waveguides of nonlinear crystals is easier to generate a squeezed vacuum than using nonlinear crystals in cavities, though the squeezing level of the squeezed vacuum with waveguides was limited -1.5 dB in our experiment.

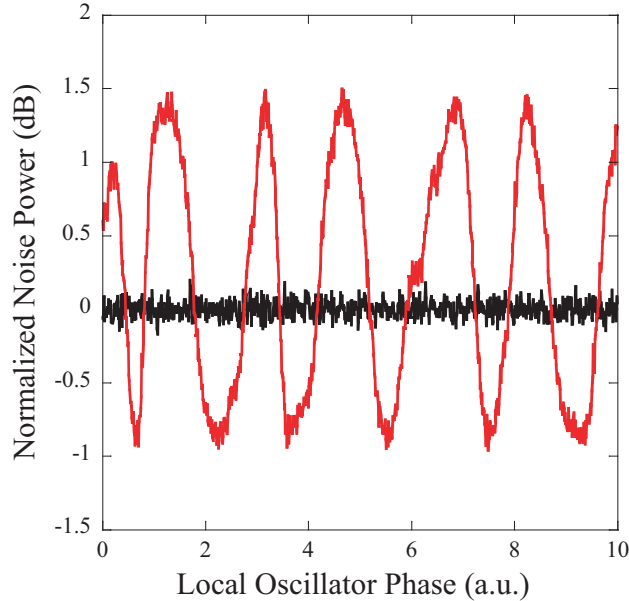


Figure 3.4: The measured quadrature noise when the squeezed vacuum incident on the homodyne detector (red trace). The black traces represents the vacuum noise level. The settings of the spectrum analyzer were zero-span mode at 15MHz, resolution bandwidth = 300kHz, and video bandwidth=300Hz. The same (anti)squeezing level was observed with the center frequency of 400kHz up to 100MHz.

solenoid coil, energy of $|F = 2, m_z = 2\rangle$ state varies due to the Zeeman effect. Thus one can change the effective two-photon detuning. Figure 3.5 illustrates a typical absorption spectrum for the probe light obtained by scanning the magnetic field. When the control light was cut off, 79% of the probe light was absorbed, independent of the magnetic field [(A) in Fig. 3.5]. In contrast, when using the control light, the absorption was reduced up to 31% at the zero-magnetic field and the width of the transparency window was 2.6 MHz, which is narrower than the natural line width of ^{87}Rb (6 MHz) ((B) in Fig. 3.5).

Next, we performed an EIT experiment with the squeezed vacuum. We again blocked the weak fundamental light and injected the second harmonic light into the LN2. The generated squeezed vacuum ($10\mu\text{W}/\text{cm}^2$) was used as the probe light and injected into the cell with the control light. We measured the quadrature noise of the probe light passing through the cell using the balanced homodyne detector. Figure 3.6 depicts the results of the balanced homodyne detection with and without the control light, where no magnetic field was applied to the cell and the quadrature noise level was normalized by the shot noise (-69.9 dBm). The noise was measured with the spectrum analyzer operated in the zero span at a center frequency of 400 kHz, a resolution bandwidth of 100 kHz, and a video bandwidth of 3 Hz. When the control light was cut off, the squeezing of the transmitted probe light was dramatically suppressed (Fig. 3.6(b)). Squeezing was restored to

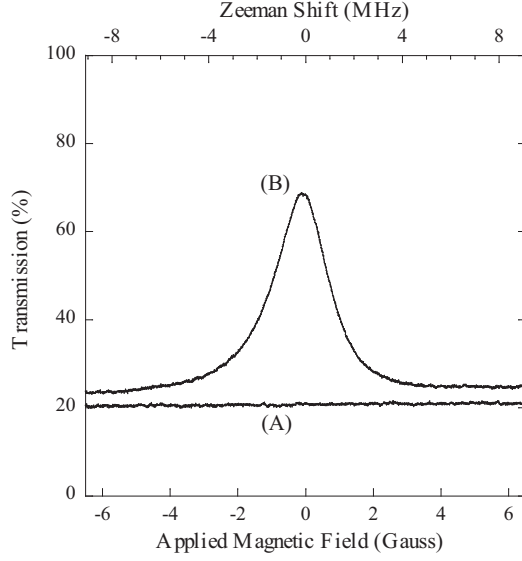


Figure 3.5: Dependence of absorption of the probe light in the coherent state on the magnetic field applied to the ^{87}Rb cell. (A) Without the control light, (B) with the control light.

0.18 ± 0.03 dB with the control light, which indicates that the opaque atomic medium became transparent for the squeezed vacuum due to the existence of the control light.

One might consider that the experimental results obtained above were due to hyperfine pumping, *i.e.*, the control light pumped almost all atoms in the $F=2$ ground state to $F=1$ state and the atomic medium became transparent for the squeezed vacuum. In order to check this, we measured the dependences of the squeezing level of the output probe beam on the applied magnetic field (Fig. 3.8(a)) and on the center frequency of the spectrum analyzer (Fig. 3.8(b)). Both cases change the measured noise, reflecting the transparency window (Fig. 3.7).

Solid circles with error bars in Fig. 3.8(a) represent experimentally obtained squeezing levels for various magnetic fields. The maximum noise reduction was obtained at a zero-magnetic field, where maximum transparency was obtained in the semiclassical experiment (see (B) in Fig. 3.5). Red circles in Fig. 3.8(b) with error bars represent the squeezing level of the probe light passing through the ^{87}Rb cell under the EIT condition. The squeezing level decreased as the center frequency of the spectrum analyzer increased, which also corresponds to the semiclassical result ((B) in Fig. 3.5). Blue circles with error bars are data when the cell was cooled to room temperature and the laser was detuned far from the atomic resonance. The squeezing level was independent of the center frequency of the spectrum analyzer.

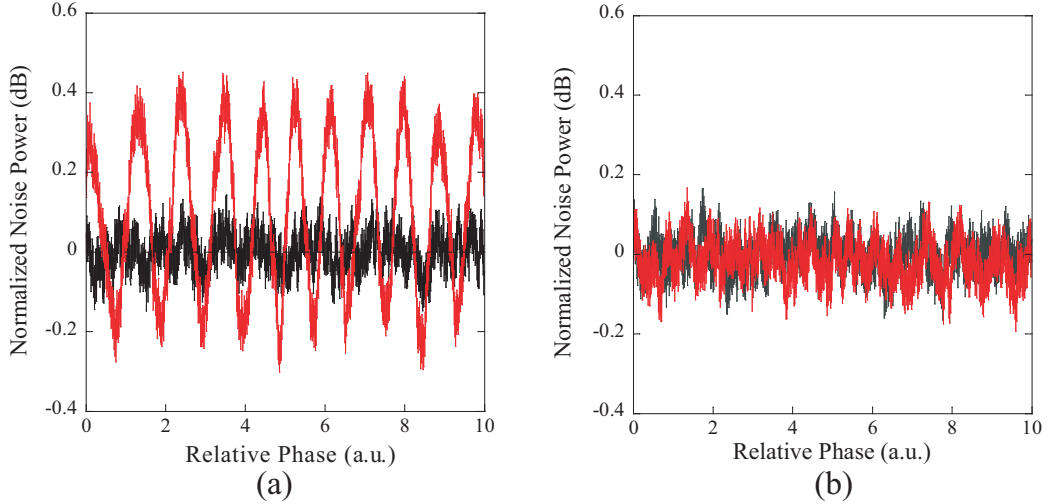


Figure 3.6: Balanced homodyne signals. Red traces are the quadrature noises of the probe lights passed through the Rb cell (a) with the control light and (b) without the control light. Black traces represent the vacuum noises (shot noises). Each data were normalized by the average of the vacuum noise (-69.9 dBm).

3.3 Discussion

First, we determine the input state to the EIT medium from the experimental data shown in Fig. 3.4. The squeezed vacuum generated in a PPLN waveguide can be considered two-mode squeezed vacuum, which is given by (1.24) and (1.25). From (1.73), the observed noise power of the two-mode squeezed vacuum is given by

$$\langle \hat{\mathcal{S}}(\delta, \theta) \rangle = \zeta \cosh 2r - \cos \phi \sinh 2r + 1 - \zeta, \quad (3.26)$$

where ζ , r , ϕ are the detection efficiency, the squeezing parameter and the relative phase between the squeezed vacuum and the local oscillator. By the fitting with (3.26), we estimated $\zeta=0.43$ and $r=0.31$.

We then discuss the results shown in Figs. 3.8(a) and 3.8(b). The squeezed vacuum passed through the EIT window was observed in the experiment. We simulate the experiment with the two-mode squeezed vacuum passing through a beam splitter of which transmission $T(\omega)$ is dependent on the frequency (Fig. (3.9)). The output field $\hat{a}^{(A)}$ from the beam splitter is given by

$$\hat{a}_{\omega\pm\delta}^{(A)} = \sqrt{T(\omega)}\hat{a}_{\omega\pm\delta}^{(1)} + i\sqrt{1-T(\omega)}\hat{a}_{\omega\pm\delta}^{(2)}, \quad (3.27)$$

where $\hat{a}_{\omega\pm\delta}^{(1)}$ and $\hat{a}_{\omega\pm\delta}^{(2)}$ are the input fields to the beam splitter. We assume that the one of the fields input to the port 1 is in a two-mode squeezed vacuum state $|\psi\rangle_1$ and the other fields input from the port 2 is in a vacuum state $|0\rangle_2$. The expectation value of the square of the quadrature of the output

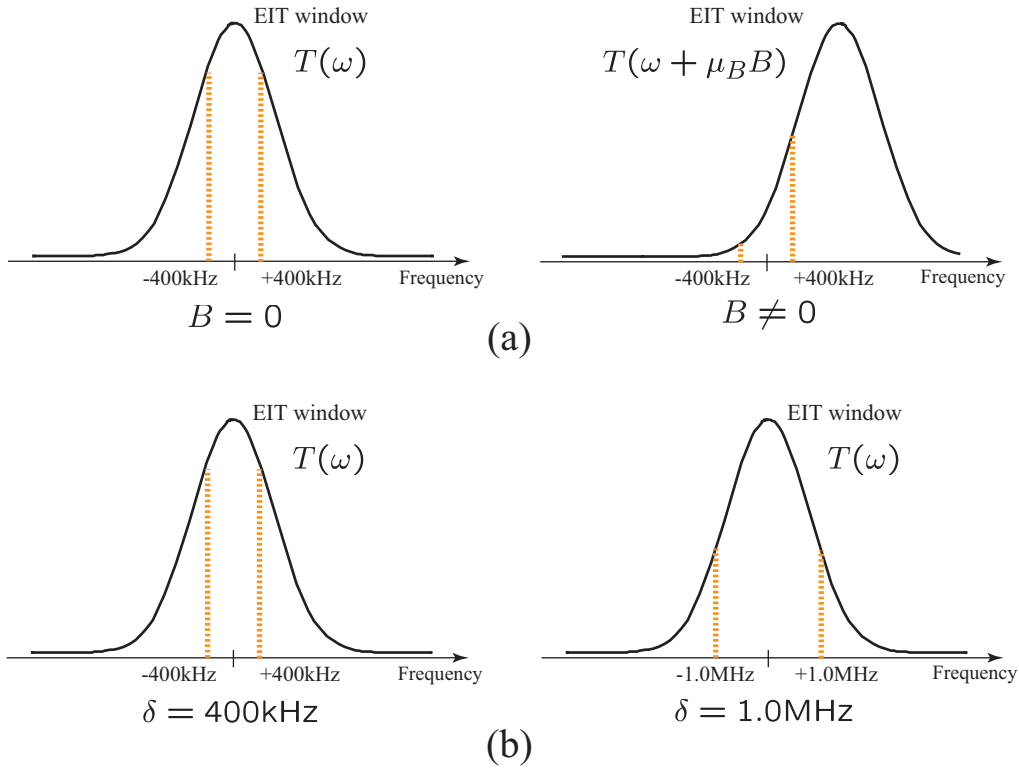


Figure 3.7: Schematic image of the experiment on (a) the dependence of the squeezing level on the magnetic field and (b) the dependence of the squeezing level on the center frequency of the spectrum analyzer. The black curves show the EIT window $T(\omega)$. The broken orange lines represent the observed frequency components of the squeezed vacuum with a monochromatic homodyne method.

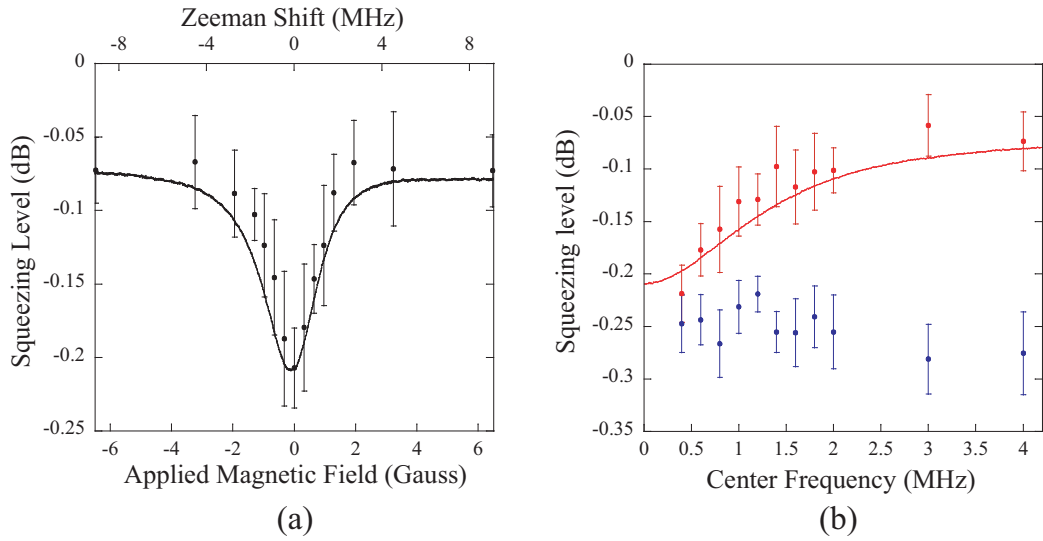


Figure 3.8: (a) Measured squeezing level of the probe light passing through the cell as a function of the applied magnetic field. (b) Same as (a) but as a function of the center frequency of the spectrum analyzer. The red dots correspond to the squeezing levels when the laser was resonance (cell temperature 48°C) and blue dots correspond to that when the laser was far off resonance (cell temperature 25°C). Each error bar represents \pm standard deviation. The curved solid lines represent numerical results of the squeezing level based on (3.28) and the plots (B) in Fig. 3.5.

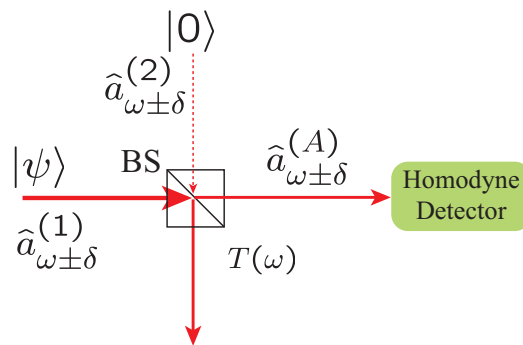


Figure 3.9: A frequency dependent beam splitter $T(\omega)$. The quadrature of squeezed vacuum is measured after passing through the beam splitter.

field $\hat{a}^{(A)}$ is given by

$$\begin{aligned}
& {}_1\langle\psi|_2\langle 0|\hat{X}(\delta,\theta)^2|0\rangle_2|\psi\rangle_1 \\
&= \frac{1}{4}\left[\left(\frac{T_++T_-}{2}\right)\cosh 2r - \sqrt{T_+T_-}\cos(\phi-2\theta)\sinh 2r + \left(1 - \frac{T_++T_-}{2}\right)\right],
\end{aligned}
\tag{3.28}$$

where T_{\pm} represents $T(\omega \pm \delta)$. Combining (3.28) with (3.26), we obtain

$$\begin{aligned}
& {}_1\langle\psi|_2\langle 0|\hat{S}(\delta,\theta)^2|0\rangle_2|\psi\rangle_1 \\
&= \zeta\left(\frac{T_++T_-}{2}\right)\cosh 2r - \zeta\sqrt{T_+T_-}\cos(\phi-2\theta)\sinh 2r + \left(1 - \zeta\frac{T_++T_-}{2}\right)
\end{aligned}
\tag{3.29}$$

The transmittance T_{\pm} can be directly obtained from the experiment results in (B) of Fig. 3.5. The curved lines in Figs. 3.8(a) and 3.8(b) represent numerical results of the squeezing level based on (3.29) and the plots (B) in Fig. 3.5. Although we changed the detection efficiency from $\zeta=0.43$ to $\zeta=0.15$, the experimental results agree well with the numerical ones, which indicates the transparency in our experiment was caused by EIT not by simple hyperfine pumping from $F=2$ to $F=1$. The detection efficiency decreased by 34%. The reflection losses at the end facets of the cell and the Glan laser prism are 16% and 7%. There still rests unknown loss of 57%. This may be explained by the reduction in homodyne detection efficiency due to the distortion of the spatial profile of the squeezed vacuum which was caused by imperfect overlapping between the control light and the squeezed vacuum.

3.4 Conclusion

We demonstrated EIT with a squeezed vacuum. Squeezing was maintained only when the control light was injected into the atomic medium and the obtained transparency window was narrower than the atomic natural linewidth. The experimental results shown in this chapter is the first evidence that EIT works for nonclassical lights.

Chapter 4

Ultraslow Propagation of Squeezed Vacuum with Electromagnetically Induced Transparency

In the previous chapter, observation of electromagnetically induced transparency with a squeezed vacuum was presented. However any dynamical effects, such a ultraslow propagation or storage of a squeezed vacuum, could not demonstrated, mainly due to poor squeezing of the probe light and to the transparency window being too broad.

The squeezing level increased by changing from the PPLN waveguides to the PPKTP crystals in cavities as the source of a squeezed vacuum. In addition, we developed a new homodyne method with a bichromatic local oscillator, which enables us to observe a squeezed vacuum which has passed through sub-MHz EIT window and ultraslow propagation of a squeezed vacuum pulse, which is a large step to genuine atomic quantum memory of photons.

4.1 Group Velocity and Transparency Window

The group velocity of a pulse is given by

$$\begin{aligned} v_g &= \frac{c}{n + \omega \frac{\partial n}{\partial \omega}} \\ &\simeq \frac{c}{1 + \omega \frac{\partial n}{\partial \omega}}, \end{aligned} \tag{4.1}$$

where n is the refractive index of the medium. Therefore the steep dispersion reduces the group velocity of the pulse. By the Taylor expansion of (3.23)

around $\delta_p = 0$, the complex susceptibility can be written as

$$\begin{aligned}\chi &= i\rho \frac{\wp_{12}^2}{\hbar\varepsilon_0} \frac{1}{\gamma_{12} - i\delta_p + \frac{\Omega_c^2}{\gamma_{13} - i\delta_p}} \\ &= \rho \frac{\wp_{12}^2}{\hbar\varepsilon_0} \left(\frac{1}{\Omega_c^2} \delta_p + i \frac{\gamma_{12}}{\Omega_c^4} \delta_p^2 + O(\delta_p^3) \right).\end{aligned}\quad (4.2)$$

The first term gives the slope of the refractive index around the resonant frequency. The group velocity in the EIT medium is given by

$$v_g \simeq \frac{c}{1 + \omega \frac{\rho \wp_{12}^2}{\hbar\varepsilon_0 \Omega_c^2}}.\quad (4.3)$$

We can reduce the group velocity by decreasing the intensity of the control light.

The second term of (4.2) gives the width of the EIT window. The transmission of the EIT medium is given by

$$T(\delta) = \exp(-\kappa kz) \simeq \exp(-\delta^2 / \Delta\omega_{\text{tr}}^2),\quad (4.4)$$

with

$$\Delta\omega_{\text{tr}} = \sqrt{\frac{\hbar\varepsilon_0}{\rho \wp_{12}^2 \gamma_{12} kz}} \Omega_c^2.\quad (4.5)$$

The width of the window is inverse proportional to the intensity of the control light.

4.2 Balanced Homodyne Method with Bichromatic Local Oscillator

When the homodyne method is employed for the measurement of the quadrature noise of the light after passing through the EIT medium, the width of the EIT window is a very important quantity. Because what we observe with a homodyne method with a monochromatic local oscillator is not the quadrature noise of the carrier frequency ω of the signal light but that of side band components $\omega \pm \delta$ (Fig.1.4). Therefore these two components have to be transmitted through the medium when the vacuum noise reduction by the squeezed vacuum is observed. One might think that we can observe the quadrature squeezing of the light which has passed through the narrow EIT window by selecting small center frequency of the spectrum analyzer. However, experimentally, the center frequency should be selected more than hundreds kHz because of the electric noise of the apparatus in the lower frequency region.

While several schemes are available to observe around quadrature squeezing of the carrier frequency component [79], we have developed a new homodyne method with a bichromatic local oscillator.

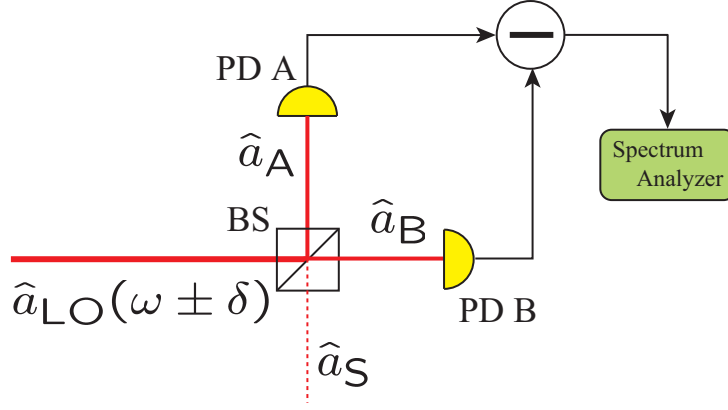


Figure 4.1: A schematic of a bichromatic homodyne method. The employed local oscillator consists of $\omega \pm \delta$ and the center frequency of the spectrum analyzer is δ .

A bichromatic homodyne method is shown in Fig. 4.1. A bichromatic local oscillator, given by (in Heisenberg picture)

$$\hat{a}_{LO}(t) = \hat{a}_{\omega+\delta}e^{i(\omega+\delta)t} + \hat{a}_{\omega-\delta}e^{i(\omega-\delta)t}, \quad (4.6)$$

is mixed with a signal light by a beam splitter. The outputs from the beam splitter is detected by commercial photodetectors, respectively. The power of the differential current is measured by a spectrum analyzer with the center frequency δ . What we need to consider here are the frequency components of the signal light of ω and $\omega \pm 2\delta$. The signal light is written as

$$\hat{a}_S(t) = \hat{a}_\omega e^{i\omega t} + \frac{1}{\sqrt{2}}\hat{a}_{\omega+2\delta}e^{i(\omega+2\delta)t} + \frac{1}{\sqrt{2}}\hat{a}_{\omega-2\delta}e^{i(\omega-2\delta)t}. \quad (4.7)$$

Substituting (4.6) and (4.7) into the input-output equations of a beam splitter (1.50) and (1.51), we obtain

$$\begin{aligned} \hat{a}_A(t) &= \frac{1}{\sqrt{2}}(\hat{a}_{\omega+\delta}e^{i(\omega+\delta)t} + \hat{a}_{\omega-\delta}e^{i(\omega-\delta)t} \\ &\quad + i\hat{a}_\omega e^{i\omega t} + i\frac{1}{\sqrt{2}}\hat{a}_{\omega+2\delta}e^{i(\omega+2\delta)t} + i\frac{1}{\sqrt{2}}\hat{a}_{\omega-2\delta}e^{i(\omega-2\delta)t}), \end{aligned} \quad (4.8)$$

$$\begin{aligned} \hat{a}_B(t) &= \frac{1}{\sqrt{2}}(i\hat{a}_{\omega+\delta}e^{i(\omega+\delta)t} + i\hat{a}_{\omega-\delta}e^{i(\omega-\delta)t} \\ &\quad + \hat{a}_\omega e^{i\omega t} + \frac{1}{\sqrt{2}}\hat{a}_{\omega+2\delta}e^{i(\omega+2\delta)t} + \frac{1}{\sqrt{2}}\hat{a}_{\omega-2\delta}e^{i(\omega-2\delta)t}). \end{aligned} \quad (4.9)$$

The differential current is described by

$$\begin{aligned} \Delta \hat{I} &= C(\hat{a}_A^\dagger(t)\hat{a}_A(t) - \hat{a}_B^\dagger(t)\hat{a}_B(t)) \\ &= C[(\hat{a}_{\omega-\delta}^\dagger\hat{a}_\omega e^{i\pi/2} + \hat{a}_{\omega+\delta}\hat{a}_\omega^\dagger e^{-i\pi/2} \\ &\quad + \frac{1}{\sqrt{2}}(\hat{a}_{\omega-\delta}^\dagger\hat{a}_{\omega-2\delta}e^{i(-2\delta t+\pi/2)} + \hat{a}_{\omega-\delta}^\dagger\hat{a}_{\omega+2\delta}e^{i(2\delta t+\pi/2)} \\ &\quad + \hat{a}_{\omega+\delta}\hat{a}_{\omega-2\delta}^\dagger e^{-i(-2\delta t+\pi/2)} + \hat{a}_{\omega+\delta}\hat{a}_{\omega+2\delta}^\dagger e^{-i(2\delta t+\pi/2)})e^{i\delta t} + \text{h.c.}]. \end{aligned} \quad (4.10)$$

We assume that the bichromatic local oscillator light consists of two coherent lights of $\omega \pm \delta$ and we replace $\hat{a}_{\omega \pm \delta}$ with $\alpha_{\omega \pm \delta}/\sqrt{2}$. For simplicity, the intensities of those lights are the same:

$$\hat{a}_{\omega+\delta} = \frac{1}{\sqrt{2}} |\alpha_{\text{bi}}| e^{i\theta_+}, \quad (4.11)$$

$$\hat{a}_{\omega-\delta} = \frac{1}{\sqrt{2}} |\alpha_{\text{bi}}| e^{i\theta_-}, \quad (4.12)$$

where θ_{\pm} represent the phases of the local oscillator of $\hat{a}_{\omega \pm \delta}$. This assumption simplify the expression of the differential current into

$$\begin{aligned} \Delta \hat{I} &= \frac{1}{\sqrt{2}} C |\alpha_{\text{bi}}| [(a_{\omega} e^{-i(\theta_- - \pi/2)} + \hat{a}_{\omega+\delta}^{\dagger} e^{i(\theta_+ - \pi/2)} \\ &\quad + \frac{1}{\sqrt{2}} (\hat{a}_{\omega-2\delta} e^{i(-2\delta t - (\theta_- - \pi/2))} + \hat{a}_{\omega+2\delta} e^{i(2\delta t - (\theta_+ - \pi/2))} \\ &\quad + \hat{a}_{\omega-2\delta}^{\dagger} e^{-i(-2\delta t - (\theta_- - \pi/2))} + \hat{a}_{\omega+2\delta}^{\dagger} e^{-i(2\delta t - (\theta_+ - \pi/2))})] e^{i\delta t} + \text{h.c.}] \\ &= \sqrt{2} C |\alpha_{\text{bi}}| e^{i\frac{\theta_+ - \theta_-}{2}} [(\hat{x}_{(\theta_+ + \theta_- - \pi)/2} + \hat{X}(2\delta, (\theta_+ + \theta_- - \pi)/2)) e^{i\delta t} + \text{h.c.}]. \end{aligned} \quad (4.13)$$

With the Wiener-Khintchine theorem, the power spectrum of the differential current is given by

$$\begin{aligned} \hat{S}_{\text{bi}}(\delta) &= 2(C |\alpha_{\text{bi}}|)^2 (\hat{x}_{(\theta_+ + \theta_- - \pi)/2} + \hat{X}(2\delta, (\theta_+ + \theta_- - \pi)/2))^2 \\ &= 2(C |\alpha_{\text{bi}}|)^2 (\hat{x}_{(\theta_+ + \theta_- - \pi)/2}^2 + \hat{X}^2(2\delta, (\theta_+ + \theta_- - \pi)/2) \\ &\quad + 2\hat{x}_{(\theta_+ + \theta_- - \pi)/2} \hat{X}(2\delta, (\theta_+ + \theta_- - \pi)/2)). \end{aligned} \quad (4.14)$$

When the signal state is in a vacuum state or squeezed vacuum state, the last term can be eliminated, and we obtain

$$\hat{S}_{\text{bi}}(\delta) = 2(C |\alpha_{\text{bi}}|)^2 \hat{x}_{(\theta_+ + \theta_- - \pi)/2}^2 + 2(C |\alpha_{\text{bi}}|)^2 \hat{X}^2(2\delta, (\theta_+ + \theta_- - \pi)/2). \quad (4.15)$$

The noise power normalized by the vacuum noise is thus written as

$$\hat{\mathcal{S}}_{\text{bi}}(\delta) = 2\hat{x}_{(\theta_+ + \theta_- - \pi)/2}^2 + 2\hat{X}^2(2\delta, (\theta_+ + \theta_- - \pi)/2). \quad (4.16)$$

The schematic image of the bichromatic homodyne method is shown in Fig. 4.2(a).

Consider the case that the quadrature noise of the two-mode squeezed vacuum is observed after the EIT window $T(\omega)$. The bandwidth of the squeezed vacuum is limited by $T(\omega)$. The observed quadrature noise is given by

$$\begin{aligned} \hat{\mathcal{S}}_{\text{bi}}(\delta) &= \frac{1}{2} [T_0 \cosh 2r - T_0 \cos \phi \sinh 2r + (1 - T_0)] \\ &\quad + \frac{1}{2} \left[\left(\frac{T_+ + T_-}{2} \right) \cosh 2r - \sqrt{T_+ T_-} \cos \phi \sinh 2r + \left(1 - \frac{T_+ + T_-}{2} \right) \right]. \end{aligned} \quad (4.17)$$

where T_0 and T_{\pm} indicate $T(\omega)$ and $T(\omega \pm \delta)$, respectively. When the medium is optically thick enough and the width of the EIT window is narrower than 2δ , the second term approaches $1/2$ (the vacuum noise), *i.e.*, the observable squeezing level is limited to -3 dB (Fig. 4.2(b)).

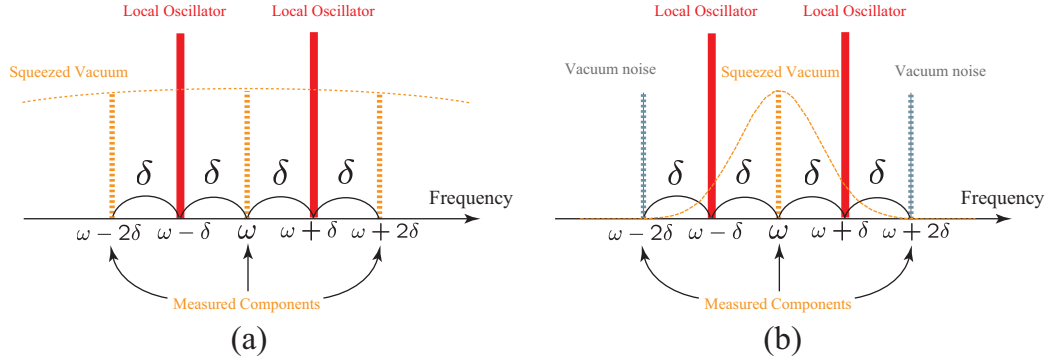


Figure 4.2: Schematic image of the bichromatic homodyne method. The local oscillator consists of $\hat{a}_{\omega \pm \delta}$. (a) The bandwidth of the squeezed vacuum is broad enough. (b) The bandwidth of the squeezed vacuum is narrower than 2δ . The bichromatic method detects the vacuum noise of $\omega \pm 2\delta$. Therefore the observed squeezing level was limited to -3 dB.

4.3 Experiment on Ultraslow Propagation of Squeezed Vacuum

4.3.1 Experiment on Observation of Narrow EIT Window with Squeezed Vacuum

The experimental setup is schematically shown in Fig. 4.3. A Ti:sapphire laser (Ti:S laser 1) was tuned to the D_1 line ($5^2S_{1/2}, F=1 \rightarrow 5^2P_{1/2}, F=2$) which corresponds to a probe transition. The beam from the other Ti:sapphire laser (Ti:S laser 2) was diffracted by an acousto-optical modulator (AOM) 1 and was used for the control field. In this experiment, the bichromatic homodyne method was employed for the measurement of the quadrature squeezing of the carrier frequency of a squeezed vacuum. The method is sensitive to the noise of the carrier frequency, therefore lights other than the squeezed vacuum should not be incident on the homodyne detector. The glan laser prism (GL) was used for splitting the control light from the probe light. The extinction ratio of the prism was, however, 10^{-5} so 0.01% of the control light was incident on the homodyne detector. Therefore two hyperfine ground states $F=1$ and $F=2$ was employed for the ground states of EIT configuration in this experiment. The frequencies of the control light and the probe light are different by the amounts of the hyperfine splitting ($\simeq 6.834$ GHz). To observe the sub-MHz EIT window, the difference of the frequencies of the control light and probe light should not be fluctuated by more than 1 MHz

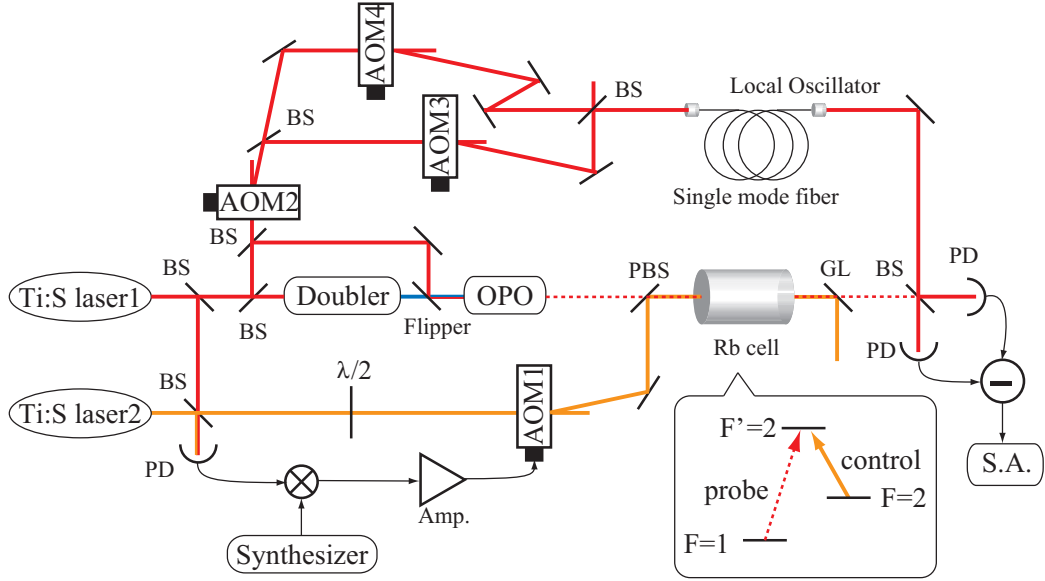


Figure 4.3: Experimental setup for observation of squeezed vacuum after passing through the sub-MHz EIT window. Amp., RF amplifier; S. A., spectrum analyzer.

during the observation. In order to stabilize the frequency of the control light, we employed a feed-forward method [80] and the frequency was able to be scanned around the $5^2S_{1/2}$, $F=2 \rightarrow 5^2P_{1/2}$, $F=1$ transition by tuning the frequency of a synthesizer. We employed a pure ^{87}Rb vapor cell filled with 5 torr of ^4He buffer gas as the EIT medium. The 75-mm-long, 25-mm-diameter cell was placed inside a three-layer magnetic shield and the residual magnetic field was less than $10 \mu\text{G}$.

First, we performed the experiment to confirm the validity of the theory described in 4.2. To avoid any absorption loss by the rubidium, the laser was detuned far from the atomic resonance. The power of the differential current from a homodyne detector was measured with the bichromatic local oscillator light ($0.8 \text{ mW} \times 2$).

The bichromatic local oscillator light $\omega \pm 1 \text{ MHz}$ was produced by driving AOM2, 3, and 4 with RF frequencies of 80 MHz, 79 MHz and 81 MHz, respectively. All driving signals were obtained by amplifying the outputs from the signal generators, whose reference clocks were synchronized with a rubidium atomic clock. The experimental result shown in Fig. 4.4(a) is obtained with varying the relative phase between local oscillator and the squeezed vacuum. The black trace was obtained when the squeezed vacuum was blocked before the homodyne detector. When the squeezed vacuum was incident on the homodyne detector, $1.53 \pm 0.20 \text{ dB}$ attenuation $3.66 \pm 0.21 \text{ dB}$ amplification were observed (red trace in Fig. 4.4(a)).

The monochromatic local oscillator (1.6 mW) could be obtained in the same experimental setup by turning off AOM4 and driving AOM2 and AOM3 with the same RF frequency, and the quadrature noise of the squeezed vacuum was measured. The experimental result is shown in Fig. 4.4(b).

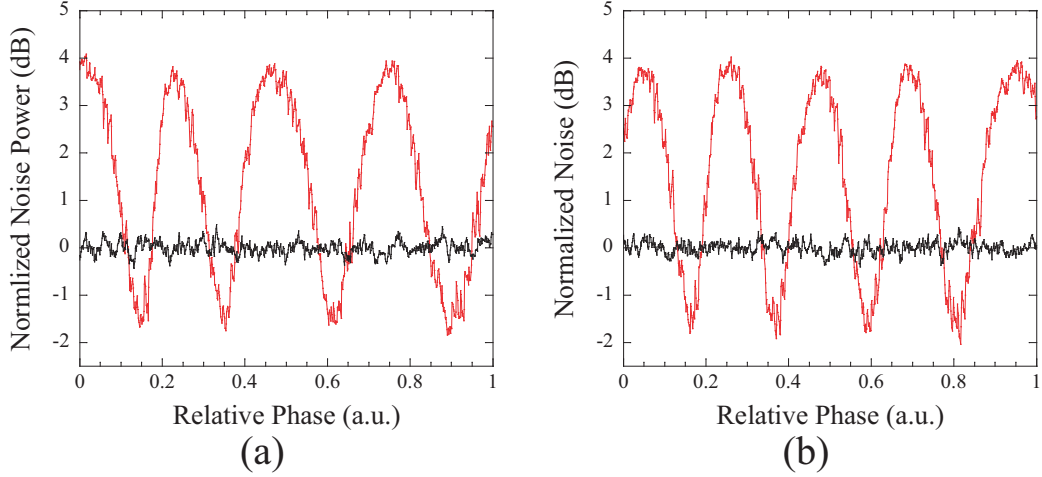


Figure 4.4: Red traces represent balanced homodyne signals of the probe light detuned far from the atomic resonance with (a) a bichromatic LO and (b) a monochromatic LO. Black traces represent the vacuum noise level. We normalized the quadrature noise levels using the vacuum noise power.

1.60 ± 0.12 dB attenuation and 3.71 ± 0.12 dB amplification were observed with the squeezed vacuum input to the homodyne detector.

The bandwidth of the OPO cavity (10 MHz) was much larger than 2 MHz, therefore the quadrature noise of the carrier frequency and the two-mode quadrature noise up to 2 MHz are the same. *i.e.*,

$$\langle \hat{x}^2 \rangle \simeq \langle \hat{X}^2(\delta = 1\text{MHz}) \rangle \simeq \langle \hat{X}^2(\delta = 2\text{MHz}) \rangle. \quad (4.18)$$

In such a case, the normalized quadrature noises measured with a bichromatic method and with a monochromatic method are the same from (1.61) and (4.16).

$$\langle \hat{\mathcal{S}}_{\text{bi}}(\delta, \theta) \rangle = \langle \hat{\mathcal{S}}_{\text{mono}}(\delta, \theta) \rangle. \quad (4.19)$$

Therefore there is no discrepancy between the prediction based on (4.16) and the experimental results. Since the frequency components outside the bandwidth OPO cavity is just in a vacuum state, if we selected a center frequency of the spectrum analyzer larger than the bandwidth OPO cavity, we could have measured the squeezing around only carrier frequency components. The bandwidth of our homodyne detector was, however, 2MHz, which was determined by the capacitance of the detector and the GB product of the operational amplifier (AD829). Therefore we could not observe the squeezing around only carrier frequency components.

The bichromatic method enables us to observe the squeezing after the squeezed vacuum passes through the sub-MHz EIT window, because the single-mode quadrature noise around the center frequency can be observed. The experiment was carried out with the cell of which temperature was actively stabilized to 28°C . A weak coherent probe light was used to determine

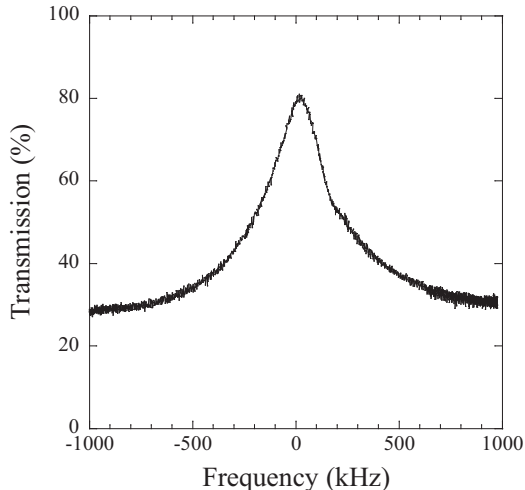


Figure 4.5: EIT window for a coherent light of 360kHz (FWHM).

the frequency width of the EIT window. We injected a light in a coherent state into the OPO cavity by using a flipper without a second-harmonic light from a Doubler, and used the output as the probe beam. The procedure described above enabled us to employ a coherent probe beam whose spatial mode was identical to that of the squeezed vacuum. The probe beam ($6.1 \mu\text{W}$) from the OPO cavity and the control light (7.5 mW) were combined using a polarizing beam splitter and then incident on the gas cell. The radii of the probe beam and the control light were 0.87 mm and 2.3 mm , respectively. After passing through the cell, the probe beam was separated from the control light by the other polarizing beam splitter and its intensity was measured using a photodetector (not shown in Fig. 4.3). Fig. 4.5 represents a typical transmission spectrum for the probe beam obtained by scanning the frequency of the control light. A transmission of 81% was obtained at two-photon resonance, whereas it decreased to 26% when the frequency of the control light was detuned from resonance. The observed width of the EIT window was 360 kHz (FWHM).

We performed the experiment on observation of squeezed vacuum passed through the sub-MHz EIT window. To improve the S/N ratio, the signal from the spectrum analyzer was averaged by 500 times. We set the spectrum analyzer in zero span mode at 1 MHz, resolution bandwidth of 300 kHz and video bandwidth of 300 Hz and averaged the data. The signal from the spectrum analyzer was divided into two, one of which was used for averaging the data and the other was used for triggering the spectrum analyzer after passing through a low pass filter of 1 Hz. The above procedure enables us to gather the noise data of which the relative phases at the origins were fixed. When the control light is on resonant, *i.e.*, the control field and the probe field satisfied the two photon resonant condition, -0.291 dB squeezing and 2.81 dB antisqueezing was observed (Fig. 4.6(a)). When we detuned the control light by 800 kHz, the squeezing and antisqueezing levels changed to -0.14 dB and 1.36 dB , respectively (Fig. 4.6(b)). This degradings of squeezing

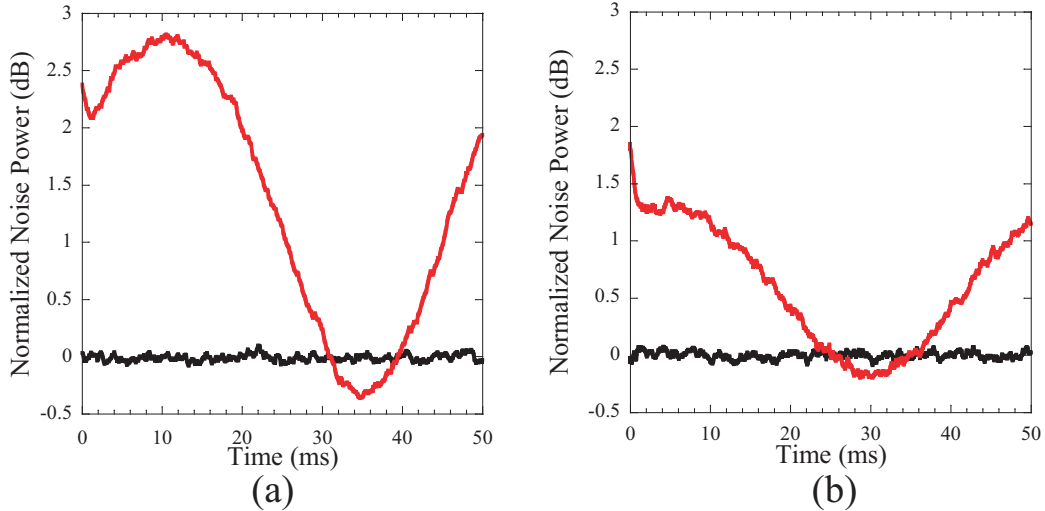


Figure 4.6: The measured quadrature noise. (a) two-photon resonance. (b) 800kHz-detuning from the two-photon resonance.

and antisqueezing levels are caused by the absorption of the center frequency components(Fig.4.7).

4.4 Experiment on Ultraslow Propagation of Squeezed Vacuum

The experiment on ultraslow propagation of a squeezed vacuum was carried out with a bichromatic homodyne method. The experimental setup is shown Fig. 4.8, which is almost same as that in the previous section. To obtain the steeper dispersion than that in the previous section, the temperature of the cell was increased to 32 °C and the intensity of the control light was decreased to 1.5 mW. The red curve in Fig. 4.9(a) shows the transmission spectrum for the probe beam obtained by scanning the frequency of the control light. A transmission of 52% was obtained at two-photon resonance, whereas it decreased to 15% when the frequency of the control light was detuned from resonance. The observed width of the EIT window was 130 kHz. When the control light was blocked, the transmission increased to 86% as is shown by a blue line in Fig. 4.9(a). It might be expected that the probe transmission would decrease when the control light is blocked since the EIT is lost. The reason that the probe transmission increased is that the hyperfine pumping from $F=2$ to $F=1$ ceased as a result of the control light being blocked; this decreased the atomic density corresponding to the probe transition.

A probe pulse having a temporal width of 12 μs was created from the continuous-wave probe beam by using AOM5 in Fig. 4.8. To achieve this we used the 0th-order (non-diffracted) light as the probe light, rather than the 1st-order diffracted light. In the later experiment, we utilized a squeezed vacuum as the probe, which is sensitive to the optical loss. The diffraction

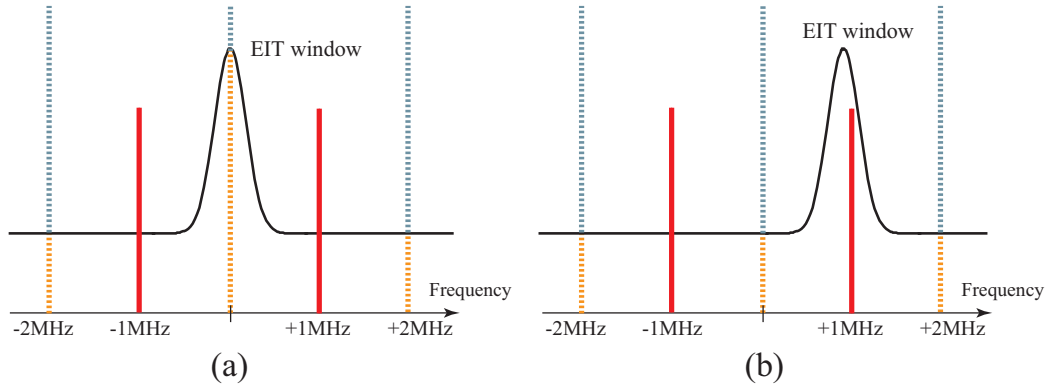


Figure 4.7: Schematic image of the observation of the squeezed vacuum after the sub-MHz EIT window. The balanced homodyne method was used to observe the frequency components of the squeezed vacuum which has passed through the EIT window, which are indicated by the orange lines. The gray lines show the vacuum noise contribution associated with the absorption. (a) The control light and the probe light satisfies the two-photon resonance condition. (b) The control light is slightly detuned from the two-photon resonance.

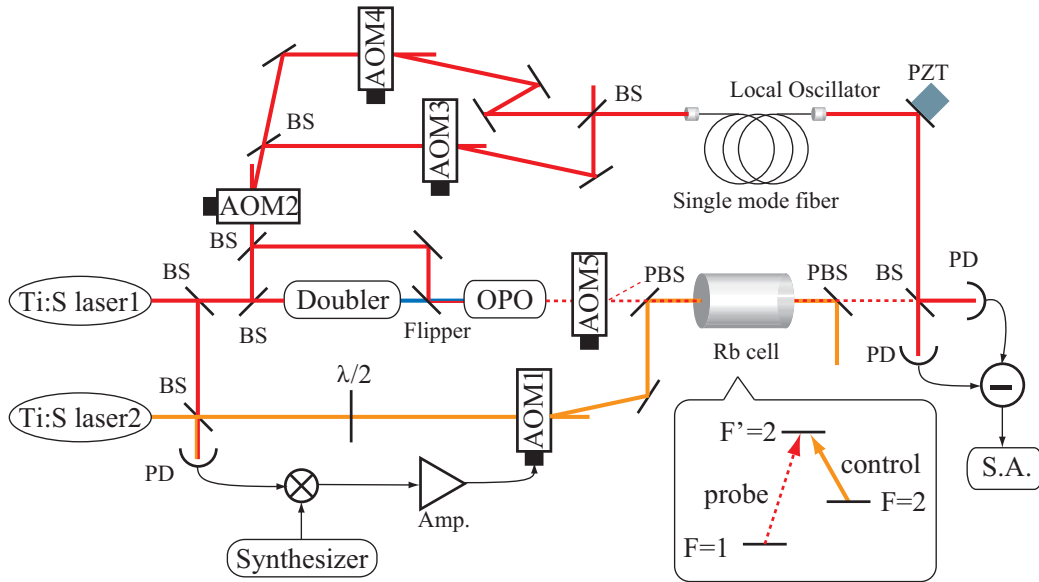


Figure 4.8: Schematic diagram of the experiment setup for ultraslow propagation of a squeezed vacuum pulse.

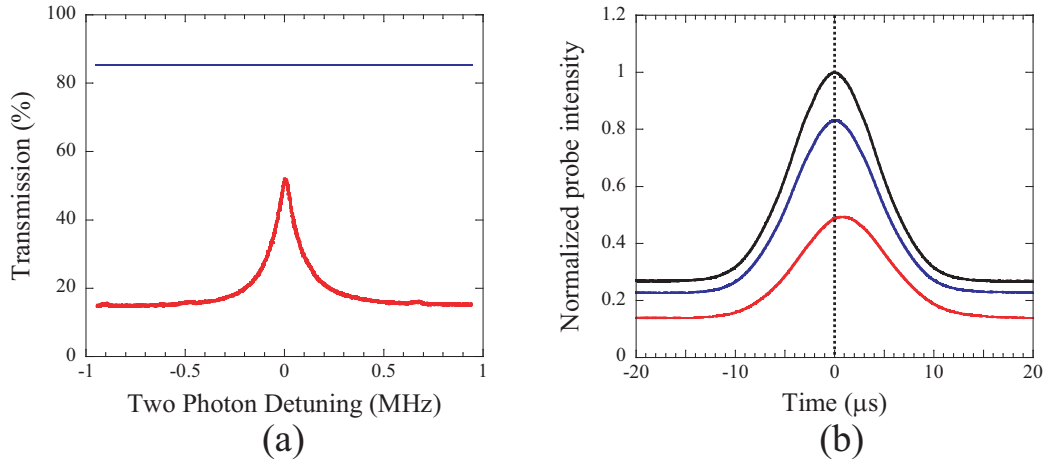


Figure 4.9: (a) Dependence of transmission of the coherent probe light on two-photon detuning without the control light (blue line), and with the control light (red curve). (b) Temporal waveform of the coherent probe pulse, detuned far from the atomic resonance without the control light (black line), resonant without the control light (blue line), and resonant with the control light (red line).

efficiency of the AOM was approximately 75%, and thus using the 1st-order beam would cause significant optical loss; therefore, we used the 0th-order beam for both the classical and the quantum experiments. The black curve in Fig. 4.9(b) is the temporal waveform of the probe pulse which is detuned far from the atomic resonance in the absence of the control light. Due to the limited diffraction efficiency of AOM5, the tail of the pulse did not approach zero. The blue curve in Fig. 4.9(b) shows the experimental result obtained when the resonant probe light was incident on the cell in the absence of the control light. As discussed above, the atomic density corresponding to the probe transition was reduced due to the absence of the control light and consequently no delay in the pulse was observed when the probe light was on resonance. These results demonstrate that the probe signal under the resonant condition in the absence of the control light can be used as a reference to measure the delay of the pulse. The red curve in Fig. 4.9(b) shows the experimental result when the probe light pulse was injected into the cell with the control light; in this case, a probe pulse delay of 820 ns was observed.

To perform ultraslow propagation of squeezed vacuum pulses, we pumped the OPO by the blue beam from the Doubler and squeezed vacuum pulses was generated with AOM5. Figure 4.12 shows the quadrature noises of the squeezed vacuum pulses and the vacuum noise level. The signal is an average of 30000 measurements and both the resolution and video bandwidths of the spectrum analyzer were set to 100 kHz. To suppress the quadrature noise below the shot noise level, the relative phase between the squeezed vacuum pulses and the LO has to be locked to $\theta=0$, where the observed noise $S(\theta)$ takes a minimum value. The phase of the 0th-order beam from an AOM

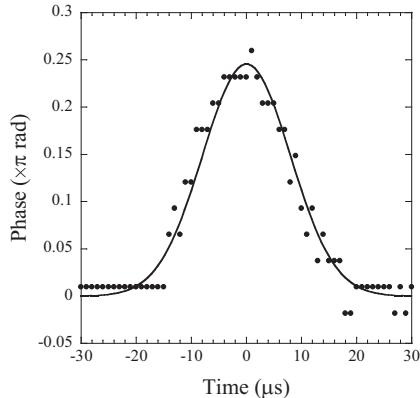


Figure 4.10: Measured temporal phase variation of the probe pulse caused by AOM5. Circles show the phase shift evaluated by the beating with the local oscillator. Black line is a fitting line by Gaussian function.

is dependent on the diffraction efficiency of the AOM¹. Phase variation of the probe pulse was measured to be Gaussian through observation of the beating between a weak probe pulse in a coherent state and the local oscillator (Fig. 4.10). The maximal phase shift (0.25π) was occurred at the maximal intensity of the pulse. Therefore we were not able to generate a squeezed vacuum pulse having a constant phase.

Instead, we controlled the phase of the local oscillator such that the relative phase θ approached zero when the pulse intensity was a maximum by the following procedure (Fig. 4.11). First, the quadrature noise of the continuous wave squeezed vacuum was measured using a spectrum analyzer and its output was used as the error signal to stabilize the relative phase θ using the PZT (Step 1). Here the offset locking technique was utilized and θ was stabilized around a value of 0.2π . Next, the squeezed vacuum was cut off using AOM5 while the voltage applied to the PZT was maintained at a constant level. During this time, an appropriate amount of the phase shift was quickly provided to the local oscillator by changing the phase of the RF signal driving the AOM2 (Step 2). Finally, the squeezed vacuum pulses were injected into the rubidium cell, where the relative phase θ approached zero when the pulse intensity was a maximum (Step 3).

The blue curve in Fig. 4.12 shows the quadrature noise of the squeezed vacuum pulse passing through the cell in the absence of the control light. While the center part of the pulse shows squeezing, its tail exhibits anti-squeezing, which is due to the limited diffraction efficiency of the AOM5 and the non-uniform phase of the squeezed vacuum pulse.

We injected the squeezed vacuum pulse with the control light into the cell (red curve in Fig. 4.12). The probe pulse experienced frequency dependent loss as is shown in the red curve in Fig. 4.9(a), *i.e.*, the carrier frequency component \hat{a}_{ω_0} experienced ultraslow propagation because of the steep dispersion

¹In this experiment, we applied the excess voltage to the voltage controlled attenuator of the AOM driver, which caused the phase variation.

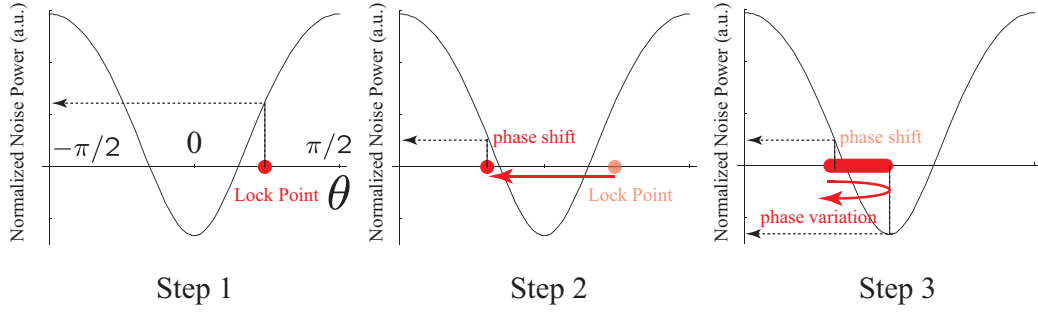


Figure 4.11: Schematic diagram for the phase shift procedure. θ is the relative phase between the squeezed vacuum and the local oscillator. Black arrows point the observed noise of the squeezed vacuum. Red circles indicate the relative phase point at every step. Transparent red circle indicates the relative phase point at the previous step.

induced by EIT. Eventually, the time when maximum degree of squeezing appeared was shifted due to the presence of the control light.

Figure 4.12(b) shows numerical simulations based on parameters obtained from the experiment. The squeezing parameter, the loss in the OPO cavity, the delay time of the carrier frequency component, and the transmission of EIT medium are evaluated from Fig. 4.4 and Fig. 4.9(b). Measured temporal phase variation of the probe pulse (Fig. 4.10) was also included in the simulation. The experimentally obtained delay time of the squeezed vacuum pulse ($1.3 \mu\text{s}$) is about twice of that obtained by the simulation (640 ns). While temporal fluctuation of the control light intensity might have caused slight difference, we do not have a clear explanation about this discrepancy. The experimentally observed squeezing level is lower than that of the simulation. We believe that this is because the locking point of the relative phase varied due to temporal fluctuations in the squeezing level.

4.5 Discussions

4.5.1 Evaluation of the delay time

We evaluated the delay time by two methods: theoretical fitting and the correlation function between the experimental data with and without the control light.

Theoretical fitting

To obtain a theoretical formula to fit the experimental data shown in Fig. 4.12, the input state is assumed to be a thermal squeezed vacuum state, which is a mixed state after a pure squeezed vacuum state is degraded due to optical loss. In the fitting process, the following parameters were experimentally obtained values from Fig.4.10 and Fig.4.9(b).

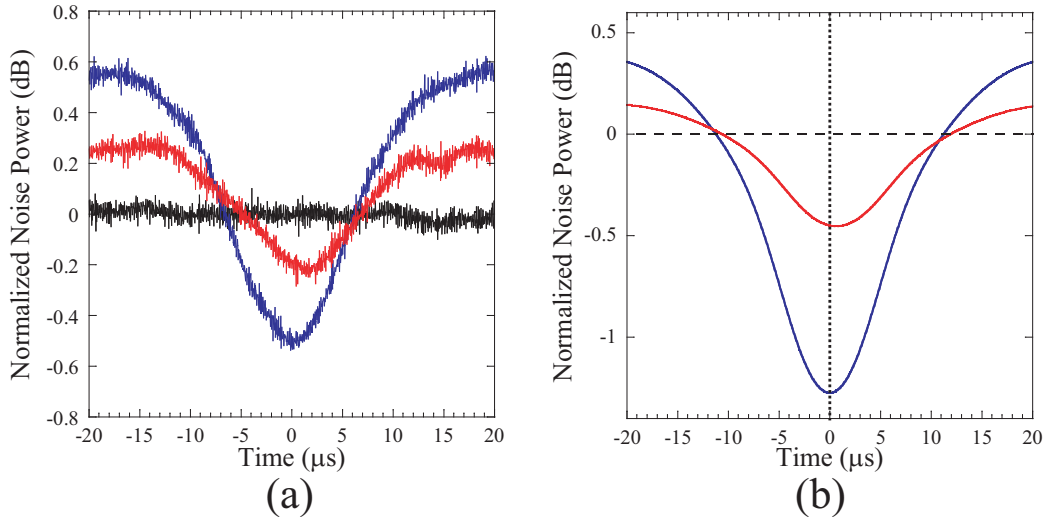


Figure 4.12: (a) Time dependence of the measured noise of the probe pulse. Each experimental data point is an average of 30000 measurements without the control light, *reference pulse* (blue tracing), with the control light (red tracing), and the shot noise (black tracing). (b) Numerical simulation based on the experimental conditions. Reference pulse (blue line) and delayed pulse (red line).

- temporal width of the phase variation of the squeezed vacuum pulse
- temporal width of the squeezed vacuum pulse

The fitting parameters are delay time, squeezing parameter, optical loss, and amount of relative phase. Figure 4.13 shows the fitting lines with experimental data. The delay time is evaluated as $1.29 \pm 0.28 \mu\text{s}$ from the fitting parameters.

Correlation function between the initial and the delayed pulse

The correlation function between the experimental data of with and without control light is given by

$$C(\tau) = \frac{1}{N} \frac{\sum_i^N f(t_i)g(t_i + \tau)}{\sum_i^N f(t_i) \sum_j^N g(t_j + \tau)}, \quad (4.20)$$

where $f(t_i)$ and $g(t_i)$ are the experimental data of with and without control light, respectively. The correlation function is shown in Fig.4.14. From the time that maximal correlation occurs, the delay time is evaluated as $1.0 \mu\text{s}$.

The above two results are strong evidence suggesting ultraslow propagation of a squeezed vacuum².

²The difference between the delay time is from that of the definition of the delay [65].

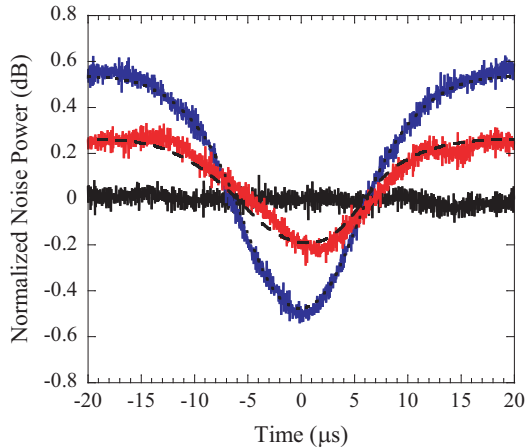


Figure 4.13: Figure 4.12 with its fitting lines. The broken line is the fittings lines of the measured noise of the probe pulse with the control light. The dotted line is that without the control light.

4.5.2 Time Dependent Absorption

Because of the imperfect condition of EIT, part of the squeezed vacuum pulse was absorbed in the experiment. If the squeezed vacuum pulse experiences time dependent absorption, artificial ultraslow propagation can be observed. There are two possibilities for such a time dependent loss.

We employed the 10 μs Gaussian pulse, therefore we gradually turn on and off the probe light. However if we suddenly turn on the probe pulse, the head of the pulse is absorbed and consumed for constructing the dark state. for constructing the dark state (nonadiabatic limit). Such an adiabatic condition is given by

$$\Omega_c \gg \frac{1}{T} \quad (4.21)$$

where Ω_c and T is Rabi frequency of the control light and the characteristic time of the probe pulse [81]. From the intensity of the employed control light, $\Omega_c \simeq 7$ MHz, which is larger than the $1/T \simeq 100$ kHz.

The other possibility of the time dependent loss is the residual magnetic field. The magnetic field rotates the atomic spins and destroys the dark state. However the measured residual magnetic field inside the shield was less than 10 μG . The Larmor frequency by this field is less than 14 Hz (See Appendix). The time scale is quite different from that of the probe pulses.

We conclude that the artificial delay does not occur, therefore the observed delay is caused by only the step dispersion of EIT medium.

4.6 Conclusion

In conclusion, we have successfully observed ultraslow propagation of a squeezed vacuum pulse using EIT. We employed a bichromatic local oscillator to observe the quadrature noise of a squeezed vacuum pulse. A delay time of 1.3

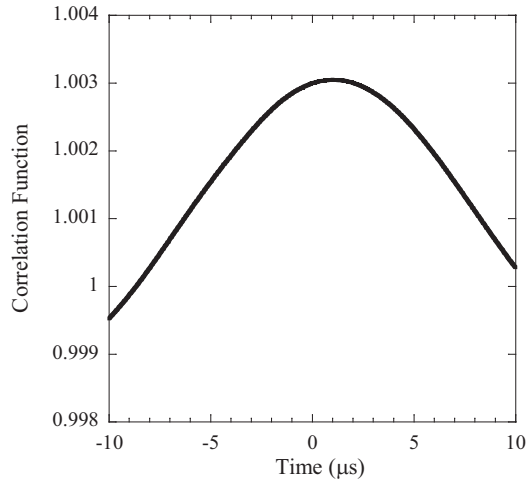


Figure 4.14: Correlation function between the time dependent noise of the probe pulse with and without the control light. The maximum correlation appears at t

μs was measured, which implies that the squeezed vacuum pulse propagated through the EIT medium with a group velocity of $c/5000$ (where c is the velocity of light in a vacuum). The obtained fractional delay was only 11% because of the relatively short atomic coherence time due to atomic diffusion. It should be possible to increase the fractional delay and also reduce the absorption loss by using a cold atomic ensemble.

Conclusion and Future Prospects

Electromagnetically induced transparency with a squeezed vacuum was investigated.

We confirmed that electromagnetically induced transparency worked for a squeezed vacuum, which is one of the nonclassical lights (Chapter 3). This was first demonstration of EIT with nonclassical lights. The experiment employed the squeezed vacuum generated by waveguides of periodically poled lithium niobate. The method with waveguides was simple, however we could not obtain higher than 1.5 dB-squeezing. The squeezing level is limited by the optical loss due to the waveguide structure, therefore it is difficult to obtain the higher squeezing level with waveguides.

For further investigation of coherent interaction between nonclassical lights and rubidium gas, a high level squeezed vacuum was generated with periodically poled KTiOPO_4 crystals in cavities (Chapter 2). The observed maximum squeezing of 2.75 dB in 795 nm was the world record at that time³. As discussed in Discussions in Chapter 2, the squeezing level was limited by the instability of the cavity. Such instability causes the relative phase fluctuation and degrades the squeezing. We expanded the beam spot size to 60 μm , reconstructed the stable cavities and obtained more than 3 dB-squeezing. Now we believe that the squeezing level is limited by the unknown loss ($\sim 5\%$) in the OPO cavity. Pursuing of the cause of this unknown loss is inevitable to increase the squeezing level. If the unknown loss can be reduced to 1.0 (0.5) %, the squeezing level will increase to 5.85 (6.75) dB.

In Chapter 4, we introduced a new homodyne method (bichromatic homodyne method) for observation of a squeezed vacuum which has passed through the sub-MHz EIT window. This technique enables us to observe such a squeezed vacuum and its ultraslow propagation. As we discussed, the narrow band squeezed vacuum is important for the experiments on ultraslow propagation or storage of squeezed vacuum. Although the bichromatic homodyne method is one of the simplest solution, the observed squeezing level is limited to 3 dB when EIT medium is optically enough dense and its EIT window is enough narrow. The other methods to observe the narrow band squeezed vacuum are known. Although the other methods seem to be experimentally difficult to implement, they are all well worth doing.

Although the storage of a squeezed vacuum has come within reach, we

³The world record is 5 dB with the same crystals as of end-January, 2007 [82].

have not demonstrated it yet with an atomic gas sample. The hot gas has a relatively large decay rate of the ground state coherence ($\sim 10\text{kHz}$) because of atomic diffusion. This diffusion can be suppressed by using a laser-cooled atomic gas. Although using the laser cooled gas will increase the amount of optics, I believe that storage of a squeezed vacuum will be demonstrated with laser-cooled atomic gas soon⁴.

I hope that the experiment in this thesis is a large step forward in the quest for demonstration of genuine quantum memory.

⁴Some experimental progress on this point is shown in Appendix. A.

Appendix A

Electromagnetically Induced Transparency with a laser-cooled atomic system

As we discussed in *Conclusions and Future Prospects*, atomic diffusion degraded the EIT condition in the experiments. Such an atomic diffusion can be suppressed by using a laser cooling technique.

The experimental setup for EIT experiments with laser cooled atoms is shown schematically in Fig. A.1. A Ti:sapphire laser (Ti:S laser 1) was tuned to the D₁ line ($5^2S_{1/2}$, $F=1 \rightarrow 5^2P_{1/2}$, $F'=2$) which corresponds to a probe transition. The beam from the other Ti:sapphire laser (Ti:S laser 2) was diffracted by an acousto-optical modulator (AOM) 1 and was used for the control field. The frequency of the control light was stabilized using a feed-forward method and it was able to be scanned around the $F=2 \rightarrow F'=2$ transition by tuning the frequency of a synthesizer. We employed a laser cooled atomic ensemble of ^{87}Rb as an EIT medium. One cycle of our experiment comprised of a cold atom preparation period and a measurement period. The preparation period and the measurement period had duration of 8.7 ms and 1.3 ms, respectively. After 5.5 ms of the magneto-optical trapping stage in the preparation period, only the magnetic field was turned off. After the eddy current ceased (~ 3 ms), both the cooling and repumping lights were turned off and a pump light, which was tuned to $F=2 \rightarrow F'=2$ transition, was incident on the gas for 100 μs to prepare the cold atoms in $F=1$ state.

A weak coherent probe light was used to observe the frequency width of the EIT window. The probe light (<1 pW) and the control light (100 μW) were incident on the gas with a crossing angle of 2.5° . The radii of the probe and the control lights were 150 μm and 550 μm , respectively. Both the probe and the control lights were circularly polarized in the same direction. During the measurement period, the probe light was incident on the atomic gas and its transmitted intensity was monitored using an avalanche photodiode (not shown in Fig. A.1). Figure A.2 represents a typical transmission spectrum for the probe light obtained by scanning the frequency of the control light, where the medium was almost transparent around two-photon resonance.

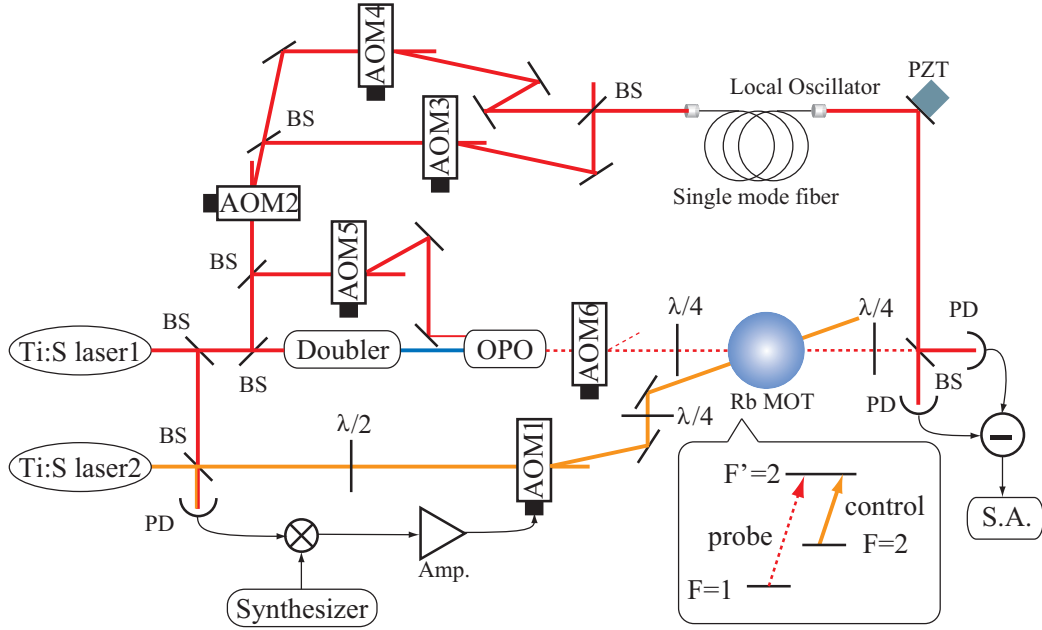


Figure A.1: Schematic diagram of the experiment setup. BS, beam splitter; PBS, polarizing beam splitter; AOM, acousto-optic modulator; PD, photodetector; SA, spectrum analyzer; Amp., RF amplifier. AOM5 consists of two AOMs to cancel the frequency shift due to the diffraction. AOM6 also consists of two AOMs, where not the 1st-order but the 0th-order beam was utilized.

In order to carry out the EIT experiment with a squeezed vacuum, the relative phase between the local oscillator light and the squeezed vacuum has to be stabilized during the measurement period. For this purpose, the relative phase was actively stabilized during the preparation period with a help of a weak coherent light incident on the OPO [76]. After the preparation period, the feedback voltage driving a PZT was held and the weak coherent light was turned off with AOM5. Eventually, the relative phase between the LO and the squeezed vacuum was kept during the measurement period [83].

The quadrature noises of the squeezed vacuum which passed through the cold atoms with the control light ($100\mu\text{W}$) were monitored by using the bichromatic homodyne method. Figure 2 (b) indicates the dependence of the quadrature noise on the two-photon detuning, where the circles (squares) were obtained when the relative phase was set to $\theta_+ + \theta_- = 0$ ($\pi/2$). Each data was averaged over $\sim 100,000$ times and both the resolution and video bandwidths of the spectrum analyzer were set to 100 kHz. When the relative phase was set to $\theta_+ + \theta_- = 0$, the squeezing level of 0.44 ± 0.09 dB was detected at the two photon resonance and the squeezing level decreased with increasing the detuning, which reflects a property of the transparency window. Around 300 kHz of detuning, the quadrature noise exceeded the shot noise level, which was because the EIT medium provided the additional phase to the probe light and changed the relative phase θ . Another peaks appeared around ± 2 MHz, which was concerned with two-mode quadrature

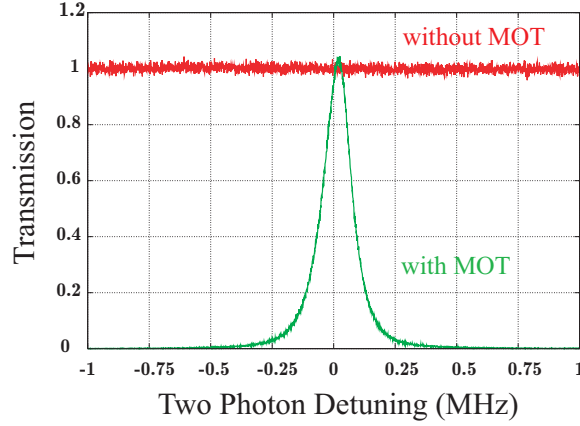


Figure A.2: Dependence of transmission of the coherent probe light on two photon detuning with the control light.

noise $\hat{X}^2(2\delta)$ ($\delta = 1$ MHz). When the control light was detuned by ± 2 MHz, the frequency component corresponding to $\nu_0 \pm 2$ MHz passed through the EIT medium, whereas that at $\nu_0 \mp 2$ MHz was absorbed, where ν_0 is the center frequency of squeezed vacuum. Therefore the quantum correlation between the two frequency modes was lost and the thermal noise corresponding to one frequency component was simply observed by the homodyne detector. Note that the noise levels were identical for both $\theta_+ + \theta_- = 0$ and $\pi/2$.

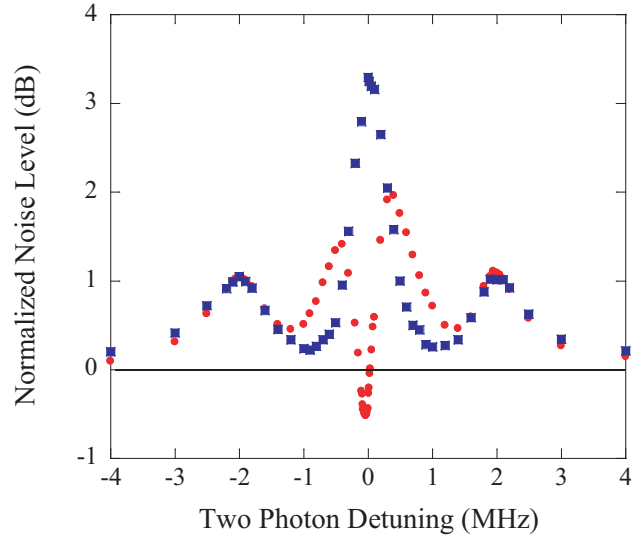


Figure A.3: Circles (Squares) indicate the quadrature noises when the relative phase between the LO and the squeezed vacuum was set to $\theta_+ + \theta_- = 0$ ($\pi/2$).

To perform ultraslow propagation of a squeezed vacuum pulse, we created a probe pulse having a temporal width of $10 \mu\text{s}$ from the continuous-wave squeezed vacuum by using two AOMs in series (AOM6 in Fig. 1). We used

the 0th-order (non-diffracted) light as the probe light, rather than the 1st-order diffracted light. The diffraction efficiency of the every AOM was 80%, and thus using the 1st-order beam would cause significant optical loss; therefore, we used the 0th-order beam for the experiments. Figure A.4(a)((b)) shows the quadrature noise of the squeezed vacuum pulses with the relative phase $\theta_+ + \theta_- = \pi/2$ (0). The signal was averaged over $\sim 100,000$ measurements. Traces (A) and (B) in Fig. A.4 show the quadrature noises of the squeezed vacuum pulses without and with the laser cooled gas in the absence of the control light, respectively. The optically dense medium absorbed the squeezed vacuum pulse and thus traces (B) are almost overlapped with the shot noises (traces (C)). When the control lights were incident on the cold atoms, the transmitted squeezed vacuum pulse were delayed. The delay time increased as the intensity of the control light decreased (see (D), (E), and (F) in Fig.4), which is a clear feature of slow propagation caused by EIT. The maximal delay of $3.1 \pm 0.11 \mu\text{s}$ was observed for the squeezed vacuum pulse with $50 \mu\text{W}$ of the control light ((F) in Fig. A.4(b)).

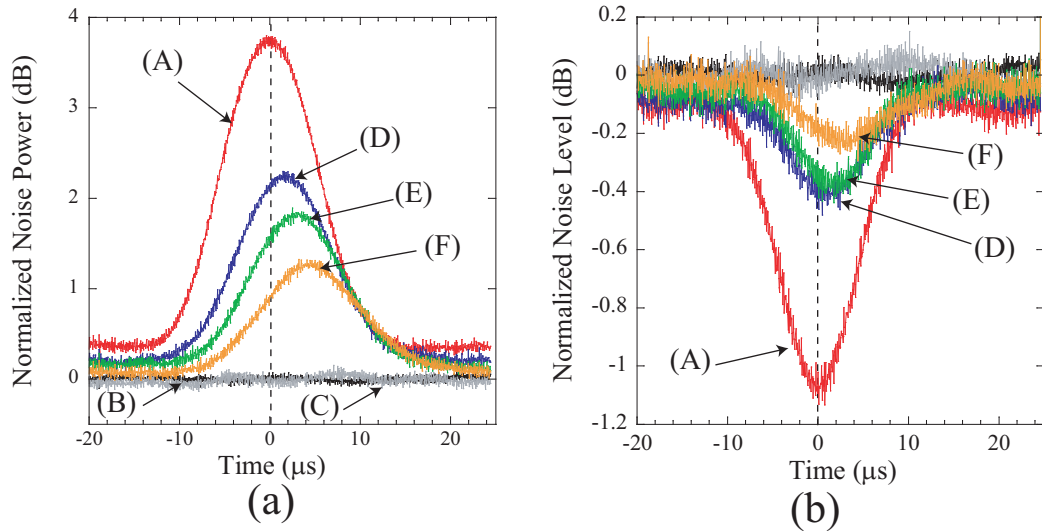


Figure A.4: Time dependence of the measured noise of the probe pulse with the relative phase (a) $\theta_+ + \theta_- = \pi/2$ and (b) $\theta_+ + \theta_- = 0$. Traces (A) show the quadrature noises of the squeezed vacuum pulses in the absence of the control lights and the cold atoms. Traces (B) show the quadrature noises of the squeezed vacuum pulses incident on the cold atoms without the control light. Traces (C) indicate the shot noises. (D), (E), and (F) show the quadrature noises of the squeezed vacuum pulses incident on the cold atoms with the control lights whose intensity were 200, 100, $50 \mu\text{W}$, respectively.

The maximum delay of $3.1 \mu\text{s}$ for $10 \mu\text{s}$ pulses is enough for performing storage of a squeezed vacuum pulse [48, 51, 52]. We are currently trying to store and retrieve the squeezed vacuum with electromagnetically induced transparency.

Appendix B

Electric Circuit

B.1 Cut-off Frequency of Fast Photodetector with OP Amp

In order to increase the bandwidth of a photodetector, OP amps are widely used. The electric circuit of a fast photodetector is shown in Fig. B.1. Here R_f and C_f are the feedback resistor and capacitor, respectively. A_v represents open-loop gain for the OP amp.

In this section, we derive the cut-off frequency of the detector. The photodiode can be modeled by a current source with a capacitor. An equivalent circuit of the Fig.B.1 is shown in Fig. B.2. The detector can be seen to be equivalent to Fig. B.2. I_p and C_p represent the output current and the capacitor of the photodiode, respectively.

The output voltage V_0 is written as

$$V_0 = -A_v V_-, \quad (\text{B.1})$$

where V_- represents the input voltage of the reverse input of the OP amp. From Kirrhioff's law, we obtain

$$I_p = sC_p V_- + (V_- - V_0) \left(\frac{1}{R_f} + sC_f \right). \quad (\text{B.2})$$

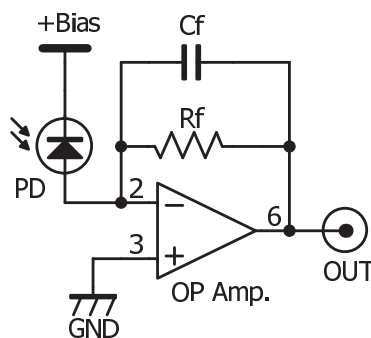


Figure B.1: Typical circuit of a fast photodetector.

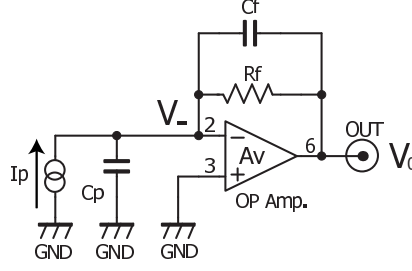


Figure B.2: Model of a fast photodetector.

V_- in (B.2) can be eliminated with (B.1).

$$I_p = -V_0 \left[\frac{sC_p}{A_v} + \left(1 + \frac{1}{A_v}\right) \left(\frac{1}{R_f} + sC_f\right) \right] \quad (\text{B.3})$$

The characteristic property of the trans-impedance amp is thus given by

$$\begin{aligned} \frac{V_0}{I_p} &= - \left[\frac{sC_p}{A_v} + \left(1 + \frac{1}{A_v}\right) \left(\frac{1}{R_f} + sC_f\right) \right]^{-1} \\ &= - \frac{A_v}{1 + A_v} R_f \frac{1}{1 + s \left(C_f + \frac{C_p}{1+A_v}\right) R_f} \end{aligned} \quad (\text{B.4})$$

The open loop gain of the OP amp is assumed to be

$$A_v = \frac{1}{1 + sT} A_0, \quad (\text{B.5})$$

where T and A_0 are the corner time constant and GB product, respectively. Substitution of (B.5) into (B.4) generates

$$\frac{V_0}{I_p} = - \frac{A_0 R_f}{1 + A_0} \frac{1}{1 + s \left(C_f R_f + \frac{T + C_p R_f}{1 + A_0}\right) + s^2 \left(\frac{T(C_f + C_p)}{1 + A_0} R_f\right)}. \quad (\text{B.6})$$

The trans-impedance is thus the second order low pass filter type and therefore there is a resonant frequency around the cut off frequency. The resonant frequency is given by

$$\omega_r = \sqrt{\frac{1 + A_0}{T(C_f + C_p)R_f}} \quad (\text{B.7})$$

With the resonant frequency, Q value is given by

$$Q = \frac{1}{\omega_r \left(C_f R_f + \frac{T + C_p R_f}{1 + A_0}\right)} \quad (\text{B.8})$$

The cutoff frequency ω_c should be less than the resonant frequency.

$$\omega_c < \sqrt{\frac{1 + A_0}{T(C_f + C_p)R_f}} \quad (\text{B.9})$$

To obtain the flat dependence on the frequency, the Q value should be around 0.7.

B.2 Homodyne Detector

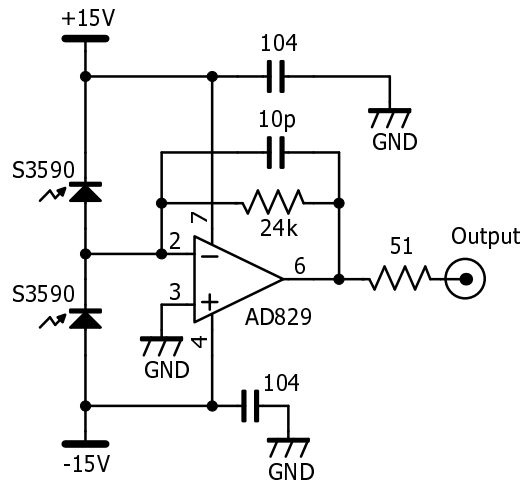


Figure B.3: Homodyne detector.

B.3 Photodetector for FM Sideband Lock

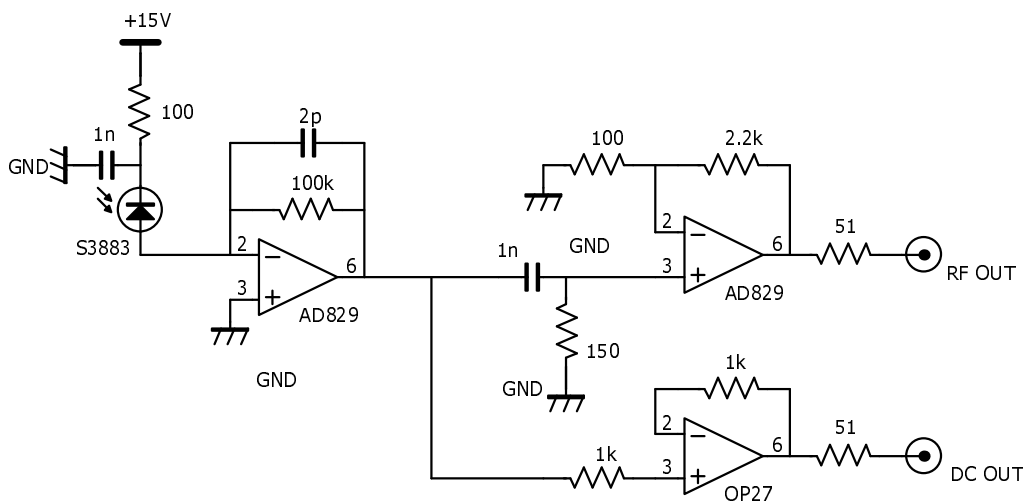


Figure B.4: Photodetector for the FM sideband lock method, by which the length of the cavities were locked on resonance. This detector was also used to lock the Ti:sapphire laser to the atomic transition.

Appendix C

Rubidium 87 data

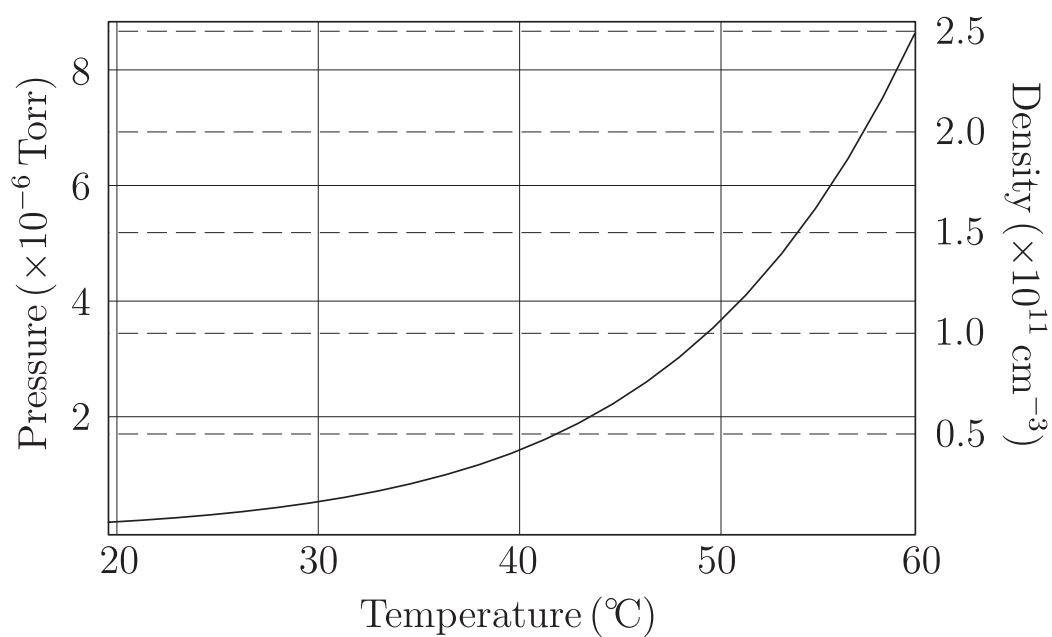


Figure C.1: Vapor pressure and atomic density of ^{87}Rb . The melting point is 39.31°C

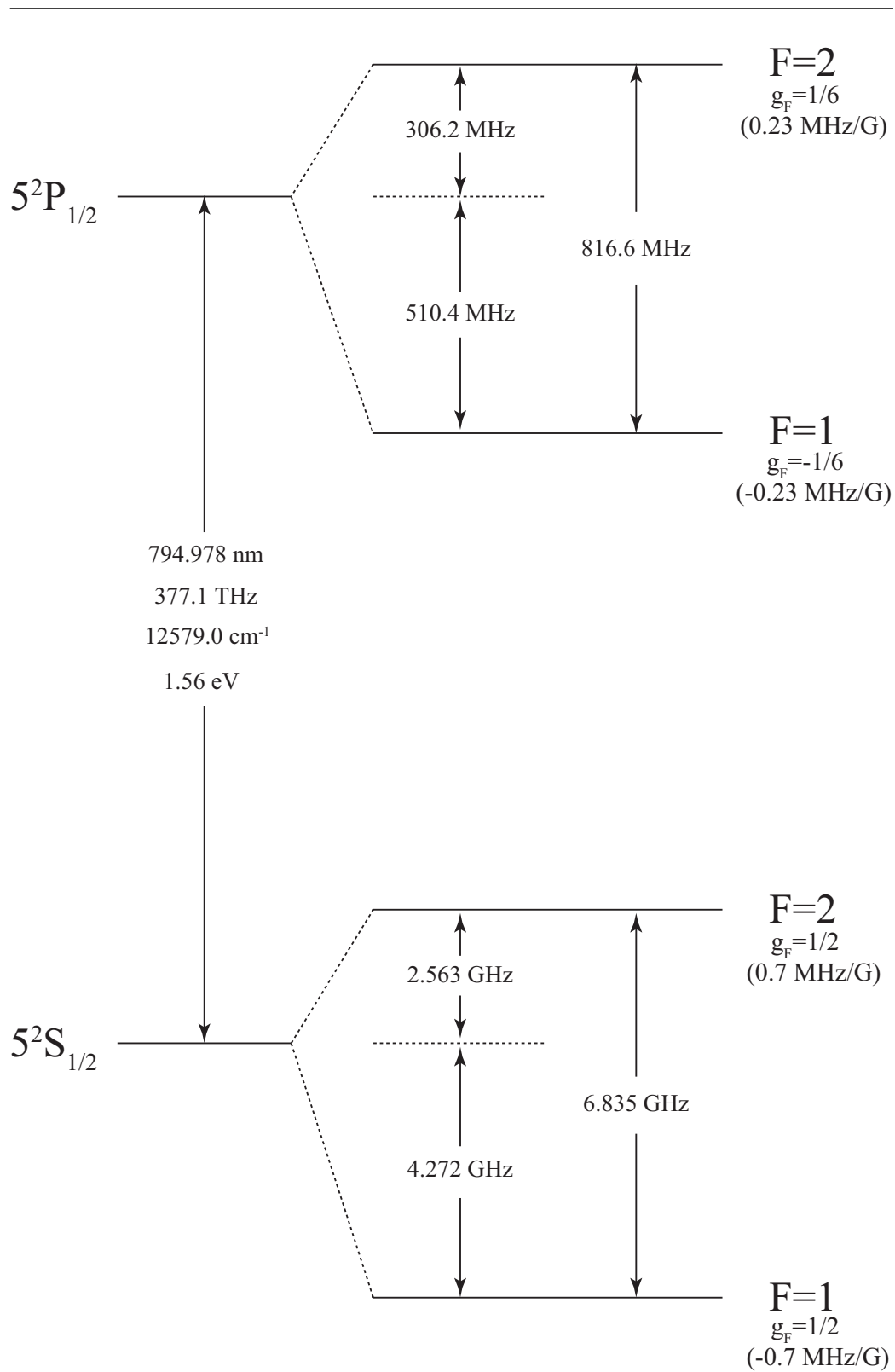


Figure C.2: ^{87}Rb D_1 transition hyperfine structure, with frequency splittings between the hyperfine energy levels. The excited-state values are taken from [84], and the ground-state values are from [85]. The approximate Landé g_F -factor for each level is also given, with the corresponding Zeeman splittings between adjacent magnetic sublevels.

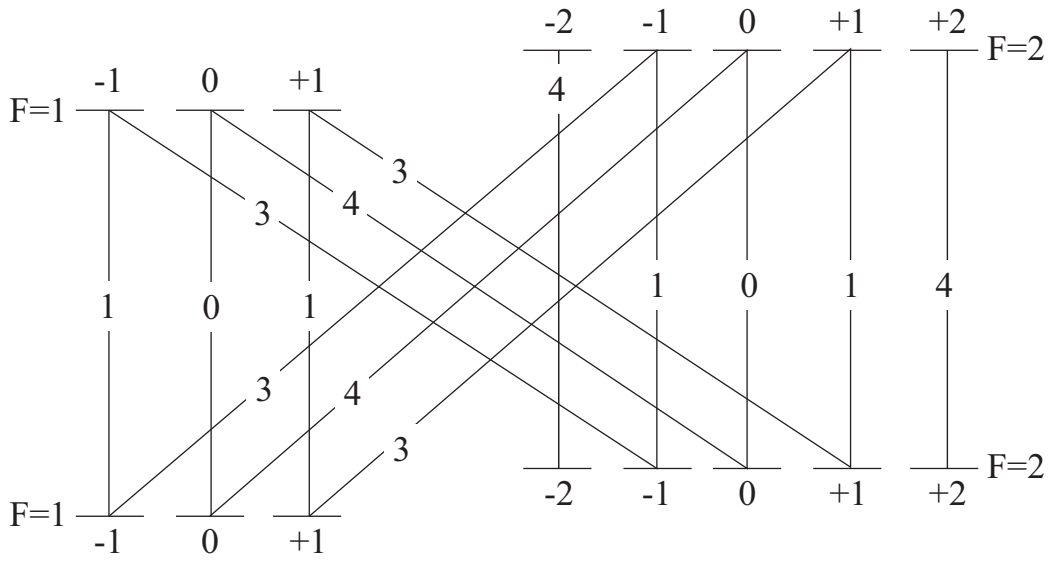


Figure C.3: Transition strengths for π transitions ($^{87}\text{Rb } D_1$).

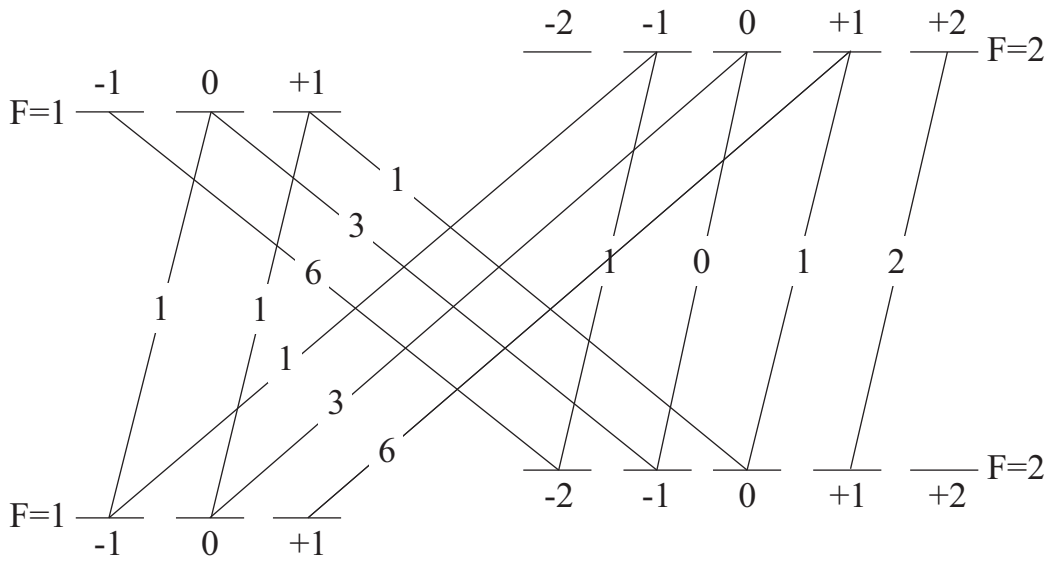


Figure C.4: Transition strengths for σ^+ transitions ($^{87}\text{Rb } D_1$).

Bibliography

- [1] T. H. Maiman, *Nature* **187**, 493 (1960).
- [2] P. A. Franken, A. E. Hill, C. W. Peters, and G. Weinreich, *Phys. Rev. Lett.* **7**, 118 (1961).
- [3] C. C. Wang and G. W. Racette, *Appl. Phys. Lett.* **6**, 169 (1965).
- [4] J. A. Giordmaine and R. C. Miller, *Phys. Rev. Lett.* **14**, 973 (1965).
- [5] C. K. N. Pate., R. E. Slusher, and P. A. Fleury, *Phys. Rev. Lett.* **17**, 1011 (1966).
- [6] R. L. Carman, R. Y. Chiao, and P. L. Kelley, *Phys. Rev. Lett.* **17**, 1281 (1966).
- [7] J. K. Ranka, R. S. Windeler, and A. J. Stentz, *Opt. Lett.* **25** 25 (2000).
- [8] S. A. Diddams, D. J. Jones, J. Ye, S. T. Cundiff, J. L. Hall, J. K. Ranka, R. S. Windeler, R. Holzwarth, T. Udem, and T. W. Hänsch, *Phys. Rev. Lett.* **84** 5102 (2000).
- [9] P. A. M. Dirac, *Proc. Roy. Soc. A* **114**, 243 (1927).
- [10] H. P. Yuen, *Phys. Rev. A* **13**, 2226 (1976).
- [11] H. P. Yuen and J. H. Shapiro, *IEEE Trans. Inf. Theory* **IT-24**, 657 (1978).
- [12] C. M. Caves, *Phys. Rev. D* **23** 1693 (1981).
- [13] R. E. Slusher, L. W. Hollberg, B. Yurke, J. C. Mertz, and J. F. Valley, *Phys. Rev. Lett.* **55**, 2409 (1985).
- [14] S. Suzuki, H. Yonezawa, F. Kannari, M. Sasaki, and A. Furusawa, *Appl. Phys. Lett.* **89**, 061116 (2006).
- [15] C. H. Bennett et al., *Phys. Rev. Lett.* **70**, 1895 (1993).
- [16] L. Vaidman, *Phys. Rev. A* **49**, 1473 (1994).
- [17] S. L. Braunstein and H. J. Kimble, *Phys. Rev. Lett.* **80**, 869 (1998).
- [18] A. Furusawa, J. L. S. rensen, S. L. Braunstein, C. A. Fuchs, H. J. Kimble, and E. S. Polzik, *Science* **282**, 706 (1998).

-
- [19] S. Lloyd and S. L. Braunstein, Phys. Rev. Lett. **82**, 1784 (1999).
- [20] S. L. Braunstein and P. van Loock, Rev. Mod. Phys. **77**, 513 (2005).
- [21] N. A. Kurnit, I. D. Abella, and S. R. Hartmann, Phys. Rev. Lett. **13**, 567 (1964).
- [22] E. L. Hahn, Phys. Rev. **80**, 580 (1950).
- [23] R. Loudon, *The Quantum Theory of Light*, (Oxford Science Publications, 2000).
- [24] K. -J. Boller, A. Imamoglu, and S. E. Harris, Phys. Rev. Lett. **66**, 2593 (1991).
- [25] S. E. Harris, Phys. Today **50**(7), 36 (1997).
- [26] S. E. Harris, Phys. Rev. Lett. **62**, 1033 (1989).
- [27] A. Imamoglu and S. E. Harris, Opt. Lett. **14**, 1344 (1989).
- [28] A. S. Zibrov, M. D. Lukin, D. E. Nikonov, L. Hollberg, M. O. Scully, V. L. Velichansky, and H. G. Robinson, Phys. Rev. Lett. **75**, 1499 (1995).
- [29] K. Hakuta, L. Marmet and B. P. Stoicheff, Phys. Rev. Lett. **66**, 596 (1991).
- [30] K. Hakuta, L. Marmet and B. P. Stoicheff, Phys. Rev. A **45**, 5152 (1992).
- [31] G. Z. Zhang, K. Hakuta, and B. P. Stoicheff, Phys. Rev. Lett. **71**, 3099 (1993).
- [32] J. C. Petch, C. H. Keitel, P. L. Knight and J. P. Marangnos, Phys. Rev. A **53**, 543 (1996).
- [33] A. Kasabi, M. Jain, G. Y. Yin, and S. E. Harris, Phys. Rev. Lett. **74**, 2447 (1995).
- [34] M. M. Kash, V. A. Sautenkov, A. S. Zibrov, L. Hollberg, G. R. Welch, M. D. Lukin, Y. Rostovtsev, E.S. Fry, and M. O. Scully, Phys. Rev. Lett. **82**, 5229 (1999).
- [35] L. V. Hau, S. E. Harris, Z. Dutton, and C. H. Behroozi, Nature **397**, 594 (1999).
- [36] E. Podivilov, B. Sturman, A. Shumelyuk and S. Odoulov, Phys. Rev. Lett. **91**, 083902 (2003).
- [37] M. Fleischhauer and M. D. Lukin, Phys. Rev. Lett. **84**, 5094 (2000).
- [38] M. Fleischhauer and M. D. Lukin, Phys. Rev. A **65**, 022314 (2002).
- [39] J. I. Cirac, P. Zoller, H. Mabuchi, and H. J. Kimble, Phys. Rev. Lett. **78**, 3221 (1997).

-
- [40] A. S. Prkins, P. Marte, P. Zoller, and H. J. Kimble, *Phys. Rev. Lett.* **71**, 3095 (1993).
- [41] T. Pelizzari, S. A. Gardiner, J. I. Cirac, and P. Zoller, *Phys. Rev. Lett.* **75**, 3788 (1995).
- [42] H. J. Kimble, *Phys. Scr.* **76**, 127 (1998).
- [43] J. Ye, D. W. Vernooy, and H. J. Kimble, *Phys. Rev. Lett.* **83**, 4987 (1999).
- [44] A. Kuhn, Markus Hennrich, and Gerhard Rempe, *Phys. Rev. Lett.* **89**, 067901 (2002).
- [45] J. McKeever, A. Boca, A. D. Boozer, R. Miller, J. R. Buck, A. Kuzmich, and H. J. Kimble, *Science* **303**, 1992 (2004).
- [46] B. Darquié, M. P. A. Jones, J. Dingjan, J. Beugnon, S. Bergamini, Y. Sortais, G. Messin, A. Browaeys, and P. Grangier, *Science*. **309**, 454 (2005).
- [47] R. H. Dicke, *Phys. Rev.* **93**, 99 (1954).
- [48] D. F. Phillips, A. Fleischhauer, A. Mair, R. L. Walsworth, and M. D. Lukin, *Phys. Rev. Lett.* **86**, 783 (2001).
- [49] C. Liu, Z. Dutton, C. H. Behroozi, and L. V. Hau, *Nature* **409**, 490 (2001).
- [50] A. Mair, J. Hager, D. F. Phillips, R. L. Walsworth, and M. D. Lukin, *Phys. Rev. A* **65**, 031802 (2002).
- [51] T. Chanelière, D. N. Matsukevich, S. D. Jenkins, S.-Y. Lan, T.A.B. Kennedy, A. Kuzmich *Nature (London)* **438**, 833 (2005).
- [52] M. D. Eisaman, A. André, F. Massou, M. Fleischhauer, A. S. Zibrov, and M. D. Lukin, *Nature (London)* **438**, 837 (2005).
- [53] A. Kuzmich, L. Mandel, and N. P. Bigelow, *Phys. Rev. Lett.* **85**, 1594 (2000).
- [54] B. Julsgaard, A. Kozhekin, Eugene S. Polzik, *Nature* **413**, 400 (2001).
- [55] B. Julsgaard, J. Sherson, J. I. Cirac, J. Fiurášek, and E. S. Polzik, *Nature (London)* **432**, 482 (2004).
- [56] J. Sherson, A. S. Sørensen, J. Fiurášek, K. Mølmer, and E. S. Polzik, *Phys. Rev. A* **74**, 011802(R) (2006).
- [57] M. Kitagawa and M. Ueda, *Phys. Rev. A* **47**, 5138 (1993).
- [58] J. Hald, J. L. Sørensen, C. Schori, and E. S. Polzik, *Phys. Rev. Lett.* **83**, 1319 (1999).

-
- [59] J. M. Geremia, J. K. Stockton, and H. Mabuchi, *Science* **304**, 270 (2004).
- [60] D. Leibfried, M. D. Barrett, T. Schaetz, J. Britton, J. Chiaverini, W. M. Itano, J. D. Jost, C. Langer, and D. J. Wineland, *Science* **304**, 1476 (2004).
- [61] A. Ourjoumtsev, R. Tualle-Brouri, J. Laurat, P. Grangier, *Science* **312**, 83 (2006).
- [62] J. S. Neergaard-Nielsen, B. M. Nielsen, C. Hettich, K. Molmer, and E. S. Polzik, *Phys. Rev. Lett.* **97**, 083604 (2006).
- [63] T. Tanimura, D. Akamatsu, Y. Yokoi, A. Furusawa and M. Kozuma, *Opt. Lett.* **31** 2344 (2006).
- [64] D. Akamatsu, K. Akiba, and M. Kozuma, *Phys. Rev. Lett.* **92**, 203602 (2004).
- [65] A.M. Steinberg, P.G. Kwiat and R.Y. Chiao, *Phys. Rev. Lett.* **68**, 2421 (1992).
- [66] K. Akiba, D. Akamatsu, and M. Kozuma, *Optics Commun.* **259**, 789 (2006).
- [67] D. K. Serkland, M. M. Fejer, R. L. Byer, and Y. Yamamoto, *Opt. Lett.* **20**, 1649 (1995).
- [68] A. Yariv, *Optical Electronics in Modern Communications*, (Oxford University Press, 1997).
- [69] S. Somekh and A. Yariv, *Opt. Commun.* **6**, 301 (1972).
- [70] G. D. Boyd and D. A. Keinman, *J. Appl. Phys.* **39**, 3597 (1968).
- [71] R. W. P. Drever, J. L. Hall, F. V. Kowalski, J. Hough, G. M. Ford, A. J. Munley, and H. Ward, *Appl. Phys. B* **31**, 97 (1983).
- [72] J. C. Jacco, D. R. Rockafellow, and E. A. Teppo, *Opt. Lett.* **16**, 1307 (1991).
- [73] J. K. Tyminski, *J. Appl. Phys.* **70**, 5570 (1991).
- [74] J. P. Fève, B. Boulanger, G. Marnier, and H. Albrecht, *Appl. Phys. Lett.* **70**, 277 (1997).
- [75] B. Boulanger, J. Rousseau, J. P. Fève, M. Maglione, B. Ménaert, and G. Marnier, *IEEE J. Quant. Electron.* **35**, 281 (1999).
- [76] E. S. Polzik, J. Carri, and H. J. Kimble *Appl. Phys. B* **55**, 279 (1992).
- [77] H. Mabuchi, E. S. Polzik, and H. J. Kimble, *J. Opt. Soc. Am.* **B11**, 2023 (1994).

-
- [78] R. L. Targat, J. -J. Zondy, and P. Lemonde, *Opt. Commun.* **247**, 471 (2005)
- [79] H. Hansen, T. Aichele, C. Hettich, P. Lodahl, A. I. Lvovsky, J. Mlynek, and S. Schiller, *Opt. Lett.* **26**, 1714 (2001).
- [80] M.Kouroggi, B. Widiyatmoko, K. Imai, and T. Shimizu, and M. Ohtsu, *Opt. Lett.* **24**, 16 (1999).
- [81] M. O. Scully and M. S. Zubairy, *Quantum Optics* (Cambridge University Press, 1997)
- [82] G. Hétet, O. Glöckl, K. A. Pilypas, C.C. Harb, B. C. Buchler, H. -A. Bachor, and P. K. Lam, *J. Phys. B* **40**, 221 (2007).
- [83] N. Takei, N. Lee, D. Moriyama, J. S. Neergaard-Nielsen, and A. Furusawa, *Phys. Rev. A* **74**, 060101(R) (2006).
- [84] G. P. Barwood, P. Gill, and W. R. C. Rowley, *Appl. Phys. B* **53**, 142 (1991).
- [85] S. Bize, Y. Sortais, M. S. Santos, C. Mandache, A. Clairon, and C. Salomon, *Europhys. Lett.* **45**, 558 (1999).

Publication List

1. “Steep optical-wave group-velocity reduction and “storage” of light without on-resonance electromagnetically induced transparency”, M. Kozuma, D. Akamatsu, L. Deng, E. W. Hagley, and M. G. Payne, Physical Review A **66**, 031801 (2002).
2. “Coherent transfer of orbital angular momentum from an atomic system to a light field”, Daisuke Akamatsu and Mikio Kozuma, Physical Review A **67**, 023803 (2003).
3. “Electromagnetically Induced Transparency with Squeezed Vacuum”, Daisuke Akamatsu, Keiichirou Akiba, and Mikio Kozuma, Physical Review Letters **92**, 203602 (2004)¹.
4. “Frequency-filtered parametric fluorescence interacting with an atomic ensemble”, K. Akiba, D. Akamatsu, and M. Kozuma, Optics Communications **259**, 789 (2006).
5. “Generation of a squeezed vacuum resonant on a rubidium D₁ line with periodically poled KTiOPO₄”, Takahito Tanimura, Daisuke Akamatsu, Yoshihiko Yokoi, Akira Furusawa, and Mikio Kozuma, Optics Letters **31**, 2344 (2006)².
6. “Ultraslow Propagation of a Squeezed Vacuum with Electromagnetically Induced Transparency”, Daisuke Akamatsu, Yoshihiko Yokoi, Akira Furusawa, and Mikio Kozuma, quant-ph/0611097 (submitted to Physical Review Letters)³.

¹Chapter 3

²Chapter 2

³Chapter 4